Electrolyte Design for Fluoride-ion Batteries



Omar Alshangiti

Lincoln College

University of Oxford

A thesis submitted for the degree of

Doctor of Philosophy

Trinity 2025

Acknowledgements

First and foremost, I'm grateful to God who eased every hurdle and permitted every step along this journey, and without whom not a cell in me would have had the strength to think or do.

I am immensely thankful for Professor Mauro Pasta, who has been supportive and always reachable and open to new ideas, and whose attention to detail and unrelenting inquisition will always be a source of inspiration. For taking me to his lab and for the many interesting discussions I'm forever grateful.

I am also thankful to the great crew at the Pasta Lab, to the senior lab legends who showed me around when I first started—Giulia Galatolo, Lorenz Olbrich, Liwei Dai, Max Schart and Po-Yuan Huang, to the F-ion subgroup— Jacob Christianson and Simone Merottoto, and to the wisdom and expertise of the postdocs—Camilla Di Mino, Taewon Kim, Hua Guo, Stephen Turell, and Krishnakanth Sada, from whom I learned so much. I'm also very grateful to Ben, Emily, Matt, Souhardh, Yi, Yiming, Xinyao, Yvonne, Jack, and Junyi for the great company around the lab and the countless lunch trips to Linacre and University Park.

I'm indebted to the many collaborations forged during my time at Oxford—Greg Reese from the Bruce Group, Thomas Hohmann at the Governeur Group, Victor Gonzalez from Williams Group, James Quirk and James Dawson from Newcastle University, and Yoan Delavoux and Gosia Swadzba-Kwansy from Queen's University in Belfast.

A special thank you goes to my amazing housemates, both past and present-Ahmed, Ahmed S, Hatim, Trey, and Adrian-and to my Oxford friends-Mohammed, Nawaf, Abdullah, another Mohammed, Saad, Waleed, yet another Mohammed (all different Mohammeds, I promise), and Rashid-for letting me test my cooking skills on them, for the many heated board game nights, and for the laughs that lasted into the morning. Thanks also to many others who I crossed paths with during my time in Oxford, and whom I can't name all here but who are all worthy of mention.

I am also thankful to the friends back in Riyadh: Omar, Ahmed, Saud, Faisal, and others for the thousands of miles of of epic road trips all over Saudi and

the Gulf. I'm honestly not sure how I could finish this degree with that much Karak in my bloodstream.

Lastly, and more importantly, thank you to my parents. My father, who taught me how to hold a pen and instilled in me the value of discipline and hard work, and my mother, for the good IQ genes and for being the first PhD holder in the family. I'm also indebted to my grandparents, for their unbounded love and for feeding me so well whenever I was back at Riyadh and Madinah. Thanks also to my three younger siblings, Abdullah, Jehan, and Joman, and to my Aunt Naeemah and toddler cousin Alyaa, who were wonderful London buddies.

"I am the combined effort of everyone I've ever known", and for them all I'm very grateful: my elementary school teachers, the Chemistry Olympiad professors, my undergrad research mentors at UIUC, and every person, alive or departed, who inspired me to appreciate the wonders of science and good craftsmanship.

It's been a fun and enriching journey, and I wish this PhD is not my best work and that that is yet to come.

Abstract

Exploring beyond-lithium charge carriers for energy storage applications remains a compelling and pressing challenge. Compared to the more researched cationic batteries such as sodium, potassium, and calcium-ion, the fluoride-ion battery remains an underdeveloped and nascent field despite its promising potential; the high electronegativity of the fluoride-ion gives rise to a high electrochemical stability, enabling high operating voltages and theoretical energy densities of up to 1393 Wh L^{-1} (588 Wh kg^{-1}), while the small ionic radius and single charge allow for ion transport with minimal polarization compared to ions with higher charge densities (e.g., Ca^{2+}, Mg^{2+}, Al^{3+}). Furthermore, the high natural abundance of fluorine and eliminating the reliance on critical minerals (i.e., Li, Co, Ni) contribute additional environmental and economic benefits.

Still, achieving a fluoride-ion battery with sufficiently long cycle life and high operating voltages has been hindered by many obstacles, most notably of which is the development of room-temperature and stable electrolytes that can overcome the chemical reactivity and low solubility of the fluoride-ion in the electrochemically stable aprotic solvents typically used in battery electrolyte solvents. This necessitates the design of novel electrolytes for the fluoride-ion, paired with detailed understanding of the fluoride-ion solvation and chemical behavior. Besides electrolytes, electrodes for fluoride-ion batteries also still require a more mechanistic understanding for the root causes of the prevalent capacity fading in the cathode, in addition to the need for leak-less and stable reference electrodes. This work makes an attempt at the development and understanding of each of these fluoride-ion components.

First, solvent-in-salt electrolytes were investigated to utilize the high fluoride solubility in protic solvents. Starting from an array of protic solvents that included alcohols and amides, aqueous cesium fluoride was explored as a model electrolyte due to its improved solubility and inflammability, achieving an electrochemical stability window of 3.1 V, high ionic conductivity, and a suppression of active material dissolution which enabled improved cycling stability. A detailed solvation study using spectroscopic techniques such as ^{17}O NMR and MD simulations revealed the elimination of free solvent molecules, whereas diffusivity

measurements showed an improved preferential fluoride migration compared to the Cs^+ ions.

Despite this improved performance, protic solvents still fall short compared to the conventional aprotic electrolytes which can achieve electrochemical stability windows of > 4 V. Aprotic solvents, both based on molecular and ionic liquid solvents, were explored due to their higher electrochemical stability windows. An imidazolium-based ionic liquid was investigated due to its high fluoride solubility of 0.67 m and its electrochemical stability window of 4.65 V and an ionic conductivity of 9.53 mS cm^{-1}. The origin of this high solubility and the solvation structure were investigated using neutron total scattering and NMR spectroscopy, revealing that the fluoride solvation was driven by electrostatic interactions and weak hydrogen bonding without covalent H—F character, suggesting chemical stability of 1,3-dimethylimidazolium towards the fluoride-ion and its potential as an electrolyte for high-voltage FIBs.

Finally, an explorative study of FIB positive and reference electrodes was performed. To understand the fluorination mechanism of the high capacity CuF_2/Cu cathode, mono-disperse copper nanocubes were synthesized with shape and size control using a colloidal synthesis and following a nucleation and growth mechanism, achieving nanoparticles with a size of 44.2 nm and a size distribution of 3.8%. In-situ TEM fluorination of the copper nanocubes was performed using a biased PbF_2 tip, showing spatial inhomogeneity as a result of the large polarity in CuF_2. Furthermore, given the lack of stable FIB reference electrodes that are chemically compatible with the fluoride-ion and the urgent need for such electrodes to investigate fluoride electrodes, a reference electrode was developed using a LaF_3 frit, a stable polymer container, and a Ag/Ag^+ reference electrolyte, and was shown to exhibit a stable OCV over a 2-day period.

Publication List

1. Alshangiti, Omar, Giulia Galatolo, Camilla Di Mino, Thomas F. Headen, Jacob Christianson, Simone Merotto, Gregory J. Rees, Yoan Delavoux, Małgorzata Swadźba-Kwaśny, and Mauro Pasta. ”Imidazolium-based ionic liquid electrolytes for fluoride ion batteries.” ACS Energy Letters 9, no. 12 (2024): 6104-6108.

2. Alshangiti, Omar, Giulia Galatolo, Gregory J. Rees, Hua Guo, James A. Quirk, James A. Dawson, and Mauro Pasta. ”Solvent-in-salt electrolytes for fluoride ion batteries.” ACS Energy Letters 8, no. 6 (2023): 2668-2673.

3. Galatolo, Giulia, Omar Alshangiti, Camilla Di Mino, Guillaume Matthews, Albert W. Xiao, Gregory J. Rees, Maximilian Schart, Yvonne A. Chart, Lorenz F. Olbrich, and Mauro Pasta. ”Advancing fluoride-ion batteries with a Pb-PbF_2 counter electrode and a diluted liquid electrolyte.” ACS Energy Letters 9, no. 1 (2023): 85-92.

4. Simone Merotto, James Quirk, Omar Alshangiti, Camilla di Mino, James Dawson, and Mauro Pasta. ”HF_2^- as an alternative charge carrier for fluoride-ion batteries” (manuscript in preparation)

Contents

List of Figures **xi**

Abbreviations **xv**

1 Introduction **1**
1.1 The Fluoride-Ion as a Charge Carrier 2
1.1.1 The Fundamentals of Fluoride-Ion Batteries 2
1.1.2 Materials for Fluoride-Ion Conversion 4
1.1.3 Materials for Fluoride-Ion Intercalation 7
1.1.4 Liquid electrolytes for FIBs 10
1.2 The Fluoride Ion chemical and solvation properties 21
1.2.1 The 'naked' fluoride dilemma 22
1.2.2 The Fluoride Salts 24
1.2.3 Fluoride Ion Solubilizing Systems 30
1.3 Thesis Objectives 34

2 Methods Fundamentals **37**
2.1 Electrochemical Methods 38
2.1.1 Electrochemical impedance spectroscopy 38
2.1.2 Cyclic Voltammetry 42
2.1.3 Galvanostatic Cycling 44
2.1.4 Electrodes and Coin Cell Fabrication 45
2.2 Solvation Structure 46
2.2.1 Total Neutron Scattering 46
2.2.2 Molecular Dynamics (MD) simulations 48
2.2.3 Density Functional Theory (DFT) 48
2.3 Chemical Analysis 49
2.3.1 Nuclear Magnetic Resonance (NMR) 49
2.3.2 Pulse-field Gradient (PFG) NMR 52
2.3.3 ICP-MS 54
2.3.4 Differential Scanning Calorimetry (DSC) 55

2.4 Solid-state Structure Characterization 56
2.4.1 (In-situ) Transmission Electron Microscopy (TEM) 56
2.4.2 X-ray Photoelectron Spectroscopy (XPS) 57

3 Solvent-in-salt Protic Electrolytes 59
3.1 The Case for Concentrated Electrolytes 60
3.2 Fluoride Solubilities in Protic Solvents 61
3.3 Electrochemical Stability Window and Thermal Stability 64
3.4 Diffusivity and Ionic Conductivity 67
3.5 Chemical Stability Towards HF Formation 70
3.6 Galvanostatic and Potentiometric Cycling 74
3.7 Dilution and Potential Co-solvents 76

4 Aprotic Electrolytes 81
4.1 Exploring the Aprotic Fluoride Solvents 82
4.2 Imidazolium-based Ionic Liquids as Fluoride Solvents 84
4.2.1 Synthesis of TMAF and [MMIm][TFSI] 85
4.2.2 Chemical Stability of the Imidazolium Towards the Fluoride Ion 87
4.2.3 Fluoride-Imidazolium Solvation Structure 92
4.2.4 Thermal Properties 95
4.2.5 ESW, Ionic Conductivity, and Diffusivity 96
4.3 Molecular Solvents 97

5 Electrodes for Fluoride-Ion Batteries 103
5.1 Hunting Down the Perfect FIB Cathode 104
5.2 Positive Electrodes Based on Cu/CuF_2 106
5.2.1 Synthesis of Monodisperse Cu Nanocubes 108
5.2.2 In-situ Fluorination of the Cu Nanocubes 114
5.3 Reference Electrodes for FIBs 115
5.4 The Future of FIB electrodes 118

References 121

List of Figures

1.1 Crystal structure of the fluoride-conductive tysonites and fluorites. 5
1.2 Crystal structure of fluoride-ion intercalation cathodes 9
1.3 Crystal structure of the fluoride-ion intercalation anodes 9
1.4 Ionic liquids used in FIBs electrolytes schematic 12
1.5 State of the art aprotic electrolyte based on BTFE solvent 14
1.6 Lewis acid anion acceptors used in FIBs. 17
1.7 Fluoride-ion reactivity schematic 21
1.8 The fluoride-ion sources schematic 28
1.9 Fluoride-ion solubilizing systems schematic 31
1.10 Fluoride-ion anion acceptor based on hydrogen bonding 32

2.1 Equivalent circuit schematic for blocking electrodes cell. 40
2.2 Nyquist plot for blocking electrodes cell. 41
2.3 Cyclic voltammetry breakdown schematic 43
2.4 Coin-cell assembly schematic 46
2.5 Pulse field gradient (PFG) NMR pulse sequences. 54

3.1 Influence of solvation on molecular orbitals energy levels schematic 61
3.2 solvent-in-salt and salt-in-solvent electrolyte comparison schematic 62
3.3 CsF solubility in various protic solvents 63
3.4 Salt-to-solvent weight and volume ratios and the 'solvent-in-salt' region. 64
3.5 Solvent-to-salt molar ratios at various concentrations 65
3.6 Electrochemical stability window (ESW) of WiSE 66
3.7 DSC and TGA thermal profiles for WiSE 66
3.8 Ionic conductivity at various concentrations. 68
3.9 Self-diffusion coefficients for the F and Cs ions 69
3.10 ^{17}O NMR spectroscopy showing the water solvent interaction . . . 69
3.11 MD simulation showing ionic species evolution and fraction of free water. 71
3.12 The fluoride ion chemical species and electronic environment obtained from pH values and ^{19}F NMR. 73

3.13 Cyclic voltammetry of CuF_2 in WISE 74
3.14 Suppressed active material dissolution of CuF_2. 75
3.15 Cyclic voltammetry of AgF_2 and ZnF_2 76
3.16 Galvanostatic cycling of symmetric Pb|PbF2 coin-cells 77
3.17 Phase separation of WiSE and DME diluent 78
3.18 Ternary phase diagram of water, CsF, and a diluent 79

4.1 Deprotonation of acetonitrile by the fluoride ion to form HF_2^- and the corresponding alkene. 82
4.2 Reaction scheme of E2 elimination reaction catalyzed by the fluoride ion. 82
4.3 Structure of potential ionic liquid cations 85
4.4 The [MMIm][TFSI] ionic liquid synthetic route. 86
4.5 ^{19}F NMR for saturated TMAF in [MMIm][TFSI] showing a solubility of 0.67 m. 87
4.6 Reaction scheme of the potential deprotonation of imidazolium to form the N-heterocyclic carbene (NHC). 87
4.7 ^{13}C NMR for [MMIm][TFSI] showing the absence of an NHC species. 89
4.8 Electronic geometry schematic for singlet and triplet carbenes . . . 90
4.9 EPR for [MMIm][TFSI] confirming the absence of NHC species . . 90
4.10 Ground-state energy levels of (de)protonated [MMIm][TFSI] obtained from DFT calculation. 91
4.11 ^{19}F NMR spectra showing traces of hydrogen bifluoride. 91
4.12 Preferential solvation revealed by ^{1}H NMR change in proton chemical shift at variable TMAF concentrations. 92
4.13 The partial radial distribution function, coordination number, and distance angle map for the CH-F interaction. 94
4.14 The spatial density function (SDF) for the fluoride ion around $[MMIm]^+$. 94
4.15 The MMIm-F and TMA-F radial distribution functions and coordination numbers. 95
4.16 TGA and DSC profiles showing thermal stability of [MMIm][TFSI] . 96
4.17 Diffusivity and ionic conductivity of TMAF in [MMIm][TFSI] 97
4.18 Electrochemical stability window and cyclic voltammograms for MnF_2 and AgF_2 in [MMIm][TFSI] 98
4.19 ^{19}F NMR for TMAF in an array of fluorinated aprotic molecular solvents. 100

5.1 Irregular, dendritic morphology upon the attempted synthesis of copper nanocubes. 111

5.2 Thick organic layers covering copper nanoparticles due to residual surfactants from the colloidal synthesis. 111
5.3 TEM micrograph and SAED pattern of the successful synthesis of monodisperse copper nanocubes. 113
5.4 XPS of the pristine Cu particle showing the formation of a copper oxide layer. 114
5.5 Schematic of the experimental setup for the in-situ TEM fluorination of the copper nanocubes. 115
5.6 Fluorinated Cu nanocubes TEM micrograph and SAED pattern. . . 116
5.7 Preliminary reference electrode assemblies. 118
5.8 Final reference electrode design, using Ag^{+}/Ag, PEEK case, and LaF_3 pellet as a frit. 119
5.9 OCV for the reference electrode showing a stable potential over 50 hours. 119
5.10 Black AgF_2 residue formed at the reference electrode tip 120

Abbreviations

FIB . . . . . Fluoride-ion batteries

LIB . . . . . Lithium-ion batteries

IL . . . . . Ionic liquid

SIS . . . . . Solvent-in-salt

WISE . . . . . Water-in-salt electrolyte

TMAF . . . . . Tetramethylammonium fluoride

MMIm 1,3-dimethylimidazolium

TFSI . . . . . Bis(trifluoromethanesulfonyl)imide

BTFE . . . . . Bis(2,2,2-trifluoroethyl) ether

AN . . . . . Acetonitrile

THF . . . . . tetrahydrofuran

G4 . . . . . tetraglyme

EIS . . . . . Electrochemical Impedance Spectroscopy

ICP-MS . . . . Inductively Coupled Plasma Mass Spectrometry

PFG NMR . . . Pulse-field gradient NMR

MD . . . . . Molecular Dynamics

DFT . . . . . Density Functional Theory

RDF . . . . . Radial Distribution Function

SDF . . . . . Spatial Density Function

ESW . . . . . Electrochemical Stability Window

SEI . . . . . Solid Electrolyte Interphase

After 25 years working with this remarkable anion,
F- continues to surprise and to delight; most of all,
though, it continues to challenge.

— James H. Clark

1 Introduction

Contents

1.1 The Fluoride-Ion as a Charge Carrier 2

1.1.1 The Fundamentals of Fluoride-Ion Batteries 2

1.1.2 Materials for Fluoride-Ion Conversion 4

1.1.3 Materials for Fluoride-Ion Intercalation 7

1.1.4 Liquid electrolytes for FIBs 10

1.2 The Fluoride Ion chemical and solvation properties 21

1.2.1 The 'naked' fluoride dilemma 22

1.2.2 The Fluoride Salts 24

1.2.3 Fluoride Ion Solubilizing Systems 30

1.3 Thesis Objectives 34

1.1 The Fluoride-Ion as a Charge Carrier

1.1.1 The Fundamentals of Fluoride-Ion Batteries

Alternatives to lithium-ion batteries are sought with an increasing urgency, primarily in pursuit of improved energy densities and to eliminate the reliance on the critical minerals (e.g. Ni, Co, Li) used in conventional lithium-ion cathodes. The fluoride ion, sitting across lithium in the periodic table, is also a single charged ion with a high redox potential of 2.87 V (vs. SHE) and a small ionic radius of 116 pm. The high redox potential renders the fluoride-ion more electrochemically stable at higher operating voltages, which enables higher energy densities compared to the less energy dense alkali metal electrochemistries (K^+, Na^+).[1] The small radius and single charge on the other hand can enable fast transport while minimizing polarization due to the small charge density, compared to multivalent charge carriers (e.g., Zn^{2+}, Mg^{2+}, Ca^{2+}) which suffer from high polarization and thus unstable cylcing. Concurrently, fluorine has an established and unstrained supply chain, as fluorine production, mined as fluorspar(CaF_2), is two orders of magnitude larger than that of lithium and is the 13th most abundant element in earth's crust.[2, 3]

Furthermore, if multivalent metal fluorides, MF_m (e.g., BiF_3, CuF_2), were used as active materials to host the fluoride ions at the cathode and were paired to a metal anode, M' (e.g., Zn, Ca, Pb), this would allow the shuttling of multiple fluoride ions per reaction step:

At the cathode:

$$MF_m + ne^- = M + nF^- \tag{1.1}$$

And at the anode:

$$M^{'} + F^{-} = M^{'}F_m + me^{-} \tag{1.2}$$

Given the energy density is directly proportional to the number of shuttled electrons, and therefore the metal valency (n):

$$E_{density} = \frac{nF(E^{o}_{cathode} - E^{o}_{anode})}{\Sigma M_i} \tag{1.3}$$

Energy densities up to 588 Wh kg^{-1} (1393 Wh L^{-1}) for selected metal electrode pairs can be obtained, corresponding to 2-3x the energy density of conventional Li-ion batteries.[4]

These promising attributes, however, have and will continue to face practical hurdles impeding the full realization of FIBs. While lithium-ion batteries benefited from continuous and intensive research and commercialization efforts since the 1970s, the fluoride-ion has only picked up momentum in 2011.[5] Some earlier sporadic effort with the concept of a fluoride shuttle was first proposed in 1974 for an all-solid state galvanic cell operating at high temperature (400 °C).[6] It was demonstrated practically two years later for a full cell by Kennedy and Schoonman, but with no reversible capacity.[7, 8] This was followed by a few studies in the 1980s to improve the ionic conductivity of solid electrolytes by doping.[9] But three decades of stagnation followed, until 2011 when Anji and Fichtner revived the field by introducing a reversible cell comprised of metal/metal fluoride electrodes (BiF_3 vs. Ce) and a solid electrolyte made of Ba-doped LaF_3, increasing the ionic conductivity by two orders of magnitudes and demonstrating reversible discharging.[5] Despite the limited cycle life and capacity retention and the high operating temperature of 150 °C needed to achieve acceptable fluoride-ion conductivity in the solid electrolyte, this work initiated an ever-growing interest in FIBs.

1.1.2 Materials for Fluoride-Ion Conversion

An ideal electrode pair for FIBs should have a large potential difference to allow a high operating voltage, low molecular weights and high capacity to enhance the energy density, reasonable ionic conductivity to allow reversible (de)fluorination, electron conductivity, and stability towards the electrolyte.

Among the metal fluorides, fluorite-type (CaF_2, BaF_2, and SrF_2) and tysonite-type (LaF_3 and CeF_3) exhibit the highest fluoride ion conductivity (10^{-5} S cm^{-1} at 150 °C). The former has a cubic ($Fm\bar{3}m$) structure that conducts fluoride ions through the central octahedral unit,[10] while the latter has a rhombohedral structure ($P3\bar{c}1$) that utilizes the Schottky vacancies for fluoride diffusion (Figure 1.1).[11] Furthermore, the fluoride ion conductivity in both fluorites and tysonites can further be increased by aliovalent doping, where a divalent fluorite-type is added to a trivalent tysonite-type matrix, or vice versa, to introduce vacancies and interstitials, respectively, that improve the fluoride ion diffusion. Forming $La_{1-x}Ba_xF_{3-x}$ (LBF) with $0 \leq x \leq 0.15$ was found to increase the vacancies concentration and hence the ionic conductivity by more than two orders of magnitudes up to 1.6×10^{-4} S cm^{-1} at 160 °C,[5] and can be further improved upon sintering LBF at higher temperatures.[12] Further studies have been performed to optimize the LBF synthesis and sintering conditions.[13, 14]

Given the low work function, and hence the low reduction potential, of these metals, in addition to their good fluoride ion conductivity, tysonites and doped-fluorites have been used as both anode and solid electrolyte materials for FIBs.[15] Among the potential anodes, CaF_2 is the most promising due to its high specific capacity of 686.6 mAh g^{-1} and low reduction potential (Table 1.1). MgF_2 has a comparable energy density to CaF_2 but is undermined by the larger volume change (43%) compared to the negligible volume change in calcium fluoride.[4] Both CaF_2 and MgF_2 have been preliminarily demonstrated as anode materials for FIBs.[16, 17] Still, comparing the metal anodes might not be as straightforward, depending on whether the gravimetric or volumetric capacity is of relevance. For instance, looking at the energy densities of Ce and Ca anodes,

the higher molar mass of Ce is offset by its larger density and trivalency, resulting in a higher volumetric capacity for Ce than Ca despite its lower specific capacity. Other material classes besides tysonites and fluorites with excellent fluoride conductivities include the main group, Sn and Pb, metal fluorides, which can enable room temperature solid electrolytes despite their narrower electrochemical stability; $Pb_xSn_{2-x}F_4$, prepared by doping α-PbF_2 with β-SnF_2, shows an excellent fluoride conductivity of 1 × 10^{-3} S cm^{-1} at room temperature.[18, 19] Anode materials based on Zn, Mn, and Pb have also been reported with variable levels of success.[20, 21] Ultimately, the choice of the anode material is likely to be limited by the corresponding cathode and electrolyte, which sets the electrochemical stability window, in addition to parameters such as chemical compatibility and reversible cycling.

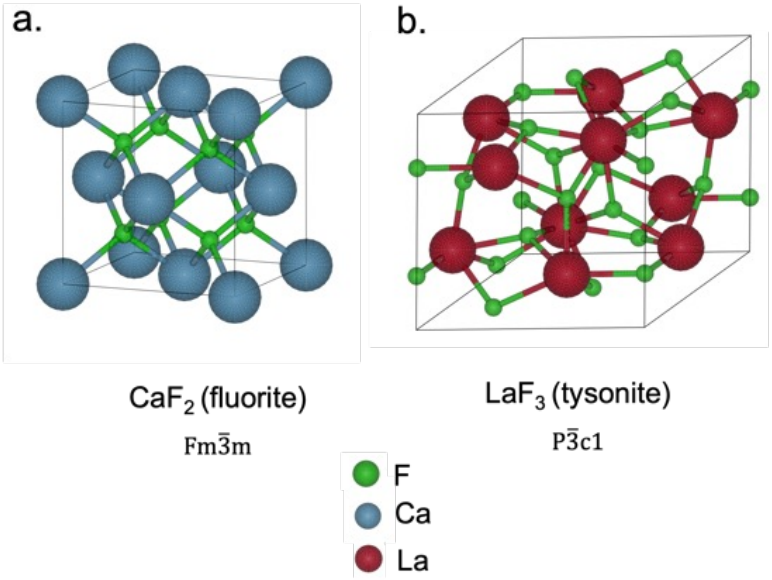


Figure 1.1: Crystal structure of the fluoride-conductive fluorite (a) and tysonite (b) used as solid electrolytes and anode materials.

Metals and metal fluorides with high reduction potentials, on the other hand, are desired as potential cathode materials. Divalent transition metal fluorides tend to have a tetragonal rutile structure (*$P4_2/mnm$*). The Trivalent transition metals (CoF_3, FeF_3), however, have a rhombohedral structure ($R\bar{3}c$), unlike the

Table 1.1: Redox potentials and specific capacities for conversion metal fluoride electrodes.

	Active material	Redox potential (V vs. Li^+/Li)	Specific Capacity ($mAh\ g^{-1}$)[a]
Cathodes	$Cu \leftrightarrow CuF_2$	3.54	527.9
	$Co \leftrightarrow CoF_3$	3.61	693.6
	$Bi \leftrightarrow BiF_3$	3.18	302.3
	$Co \leftrightarrow CoF_2$	2.74	553.1
	$Ni \leftrightarrow NiF_2$	2.96	554.5
	$Fe \leftrightarrow FeF_3$	2.74	712.5
	$Sn \leftrightarrow SnF_2$	2.97	342.0
	$Pb \leftrightarrow PbF_2$	2.89	218.6
	$Sn \leftrightarrow SnF_4$	2.86	550.6
	$Fe \leftrightarrow FeF_2$	2.63	571.2
Anodes	$Ca \leftrightarrow CaF_2$	0.20	686.6
	$Mg \leftrightarrow MgF_2$	0.54	864.5
	$Y \leftrightarrow YF_3$	0.41	551.1
	$La \leftrightarrow LaF_3$	0.66	410.4
	$Ce \leftrightarrow CeF_3$	0.70	407.9
	$Al \leftrightarrow AlF_3$	1.15	957.4
	$Ti \leftrightarrow TiF_4$	1.39	766.5
	$Zr \leftrightarrow ZrF_4$	1.40	641.1
	$V \leftrightarrow VF_3$	1.85	744.9
	$Mn \leftrightarrow MnF_2$	1.91	576.8
	$Zn \leftrightarrow ZnF_2$	2.39	518.4

[a]Calculated based on the mass of the metal fluoride.

trivalent BiF_3 orthorhombic structure (Pnma), and the tetravalent SnF_4 which has a tetragonal (I4/mmm) structure.

The cycling of FIBs has been attempted using different combinations of cathode, anode, and electrolyte materials, with CuF_2 and BiF_3 cathodes being the most used. The highest performance reported for copper cathodes have been for a maximum of 10 cycles, with a reversible capacity half that of the theoretical.[22] Bismuth cathodes, on the other hand have been used more widely, with a reversible capacity of around 50 $mAhg^{-1}$ at the 40th cycle,[16] although it was also found that a much longer cycling lifespan could be achieved using a bismuth oxyfluoride buffering phase.[23] Other transition metal fluorides were hardly ever used as cathodes for FIBs. FeF_3, for instance, has a lower reduction potential than CuF_2 but a higher specific capacity and a slightly lower energy density, but

its reversible (de)fluorination in a FIB has never been reported to the best of our knowledge.

1.1.3 Materials for Fluoride-Ion Intercalation

Conversion-type electrodes have been by far the most widely used in FIBs due to their higher specific capacities, which stems from their relatively lower molecular weight and ability to shuttle multiple fluoride ions per reaction step. However, conversion electrodes also suffer from poor cycling due to the diffusion requirement and volume change during (de)fluoridation.[4, 15] Compared to conversion-type active materials, intercalation often has an improved cycle life and rate capability due to the migration of a single ionic species in a stable fluoride ion host.

Intercalation cathodes are based on three classes of materials: perovskites (AMO_{3-y}), layered Ruddlesden-Popper oxides ($AO(AMO_3)_n$), and the tunnelled Schafarzikite oxides (MSb_2O_4). Perovskites, based on $BaFeO_{2.5}$, were the first reported cathode intercalation materials for FIBs, despite showing low fluoride uptake and performance.[24] Intercalation cathodes based on $SrFeO_2$ were also reported, but it was found that it is chemically unstable at the operating temperature of 170 °C.[25] The second class of intercalation cathodes, the Ruddlesden-Popper oxides (e.g., La_2MO_4 and $LaSrMO_4$) are potentially more promising candidates. With a K_2NiF_4-type structure ($AO(AMO_3)_n$), they contain n perovskite layers contained between rock-salt (AO) layers along the z-axis, with 2 fluoride ions per formula occupying the vacancies in the rock-salt layers (Figure 1.2a). These intercalation cathodes exhibit theoretical capacities between 130-160 $mAhg^{-1}$, similar to intercalation cathodes in conventional lithium ion batteries.[15] Some reversible intercalation has been shown for $LaSrMnO_4$ against a Pb/PbF_2 conversion anode, showing a two-step fluoride intercalation to form $LaSrMnO_4F_{2-x}$ with a discharging capacity of 20-25 $mAhg^{-1}$, which is still higher than the capacity achieved in $BaFeO_2$.[26] Other Ruddlesden-Popper based intercalation cathodes such as La_2NiO_4 and La_2CoO_4 have also been reported for La_2NiO_4,

a 2-electron Ni redox transition confirmed by XANES and corresponded to 1.59 - 1.79 fluoride ions per formula,[27] whereas La_2CoO_4 showed a lower fluoride insertion of 1.2.[28] For both intercalation cathodes, low-capacity cutoffs (<50 $mAhg^{-1}$) where required to maintain reversible cycling (20-200 cycles), as higher cutoffs resulted in the oxidation of conductive carbon. Furthermore, it was found that Ruddlesden-Popper oxyfluorides, prepared by topochemical fluorination of the corresponding oxides, were also suitable intercalation cathodes for FIBs. In this case, each oxygen atom is substituted by two fluoride ions during the fluorination.[15] The fluoride ion uptake for oxyfluorides such as $LaNi_2O_3F_2$ was found to be one fluoride per formula unit.[29] The third class of intercalation cathode materials, the Schafarzikite-type, exhibits a tetragonal symmetry consisting of linked MO_6 octahedra and can intercalate fluoride ions along the channels,[30] similar to the 1D intercalation in olivine cathodes for lithium batteries (Figure 1.2b).[31] Successful fluoride (de)intercalation of $FeSb_2O_4$ has been recently reported at room temperature.[32] However it was only possible topochemically (not electrochemically) in solid FIBs. Electrochemical intercalation of $(Co/Mn)_{0.5}Fe_{0.5}Sb_2O_4$ was, however, demonstrated electrochemically by Nowroozi et. al. at temperatures above 170 °C.[33]

Beside the challenged intercalation cathodes, intercalation anodes are also an incipient class of fluoride-intercalating materials. Electrides (e.g. Ca_2N and Y_2C) are layered materials with electrons residing freely in the lattice points. Interestingly, electrides were shown to intercalate fluoride ions to form Ca_2NF and Y_2CF_2, respectively, with redox potentials close to that of the comprising metal (e.g. Ca) (Figure 1.3).[34, 35] Due to their low molecular weights and potentially high reversibility, electrides can be formidable anode materials if electrolytes that are stable towards strong reducing agents can be designed.

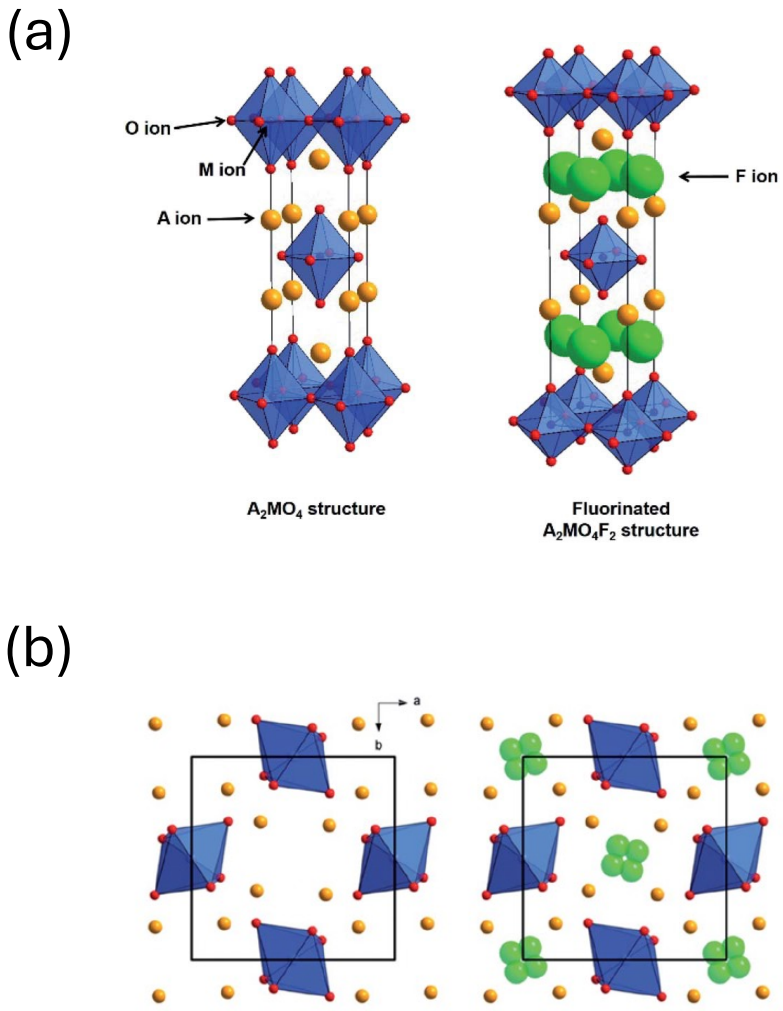


Figure 1.2: Fluoride ion intercalation cathodes based on (a) Ruddlesden-Popper oxides. (b) Schafarzikite-type oxides. Adapted from [15].

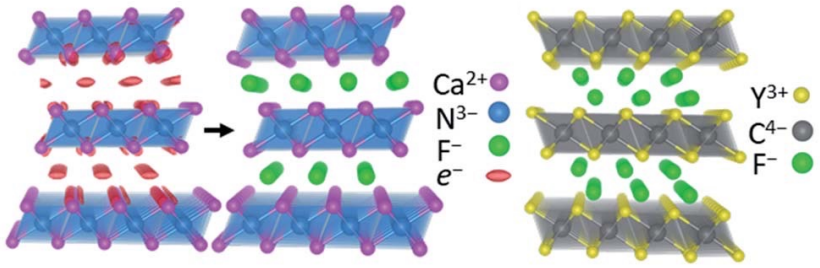


Figure 1.3: Fluoride ion intercalation in (a) Calcium nitride, Ca_2N and (b) Yttrium carbide, Y_2C. Adapted from [34].

1.1.4 Liquid electrolytes for FIBs

The vast majority of literature reporting FIBs uses solid electrolytes. Despite their improved stability and wider electrochemical stability window, solid electrolytes have restricted the operation temperatures of FIBs to above 90 °C due to their poor ionic conductivity at room temperature, in addition to other problems such as poor interfacial contact with the electrolyte, harder cell assembly, and larger bulk density that reduces the cell energy density compared to liquid electrolytes. Liquid electrolytes have the chance to tackle these challenges. So far, liquid electrolytes for fluoride ion batteries have been based on four major systems: polymers, binary organic electrolytes, anion acceptors, and electrolytes based on protic solvents.

Polymers

Electrolytes based on a polyethylene glycol (PEG) matrix were first demonstrated using ammonium bifluoride salt mobilized in the solid polymer using small amounts of acetonitrile (AN) and dimethyl chloride (DMC), with BiF_3 as a cathode and Li or Mg as anodes.[36, 37] The PEG-matrix was used to coordinate to the ammonium cation through hydrogen bonding, thus enhancing the solubility and migration of the free fluoride ion. The formation of the PEG-O ... H-N bond was confirmed using FT-IR, with the original NH peak at 3400 shifting to 3200 cm^{-1} upon coordination. The salt was fully embedded in the polymer matrix that it contributed an enhanced thermal stability, with the salt-polymer matrix degrading at 340 °C compared to a degradation temperature of 130 °C for the pure ammonium bifluoride. Furthermore, comparing different polyethylene chain lengths, the shorter chain lengths (higlyme and tetraglyme) gave higher initial capacities compared to the longer PEG6000 and PEO.[37] Another system reported the use of NaF and LiF salts in a PEG-matrix using a trimethoxy boroxine anion acceptor.[38] For all these reports, the ionic conductivity ranged between 0.8 - 2 mS/cm, and

only the first discharge capacity was reported (ca 60% of the theoretical), which raises concerns about the cycling stability of polymeric electrolytes.

Aprotic Organic Electrolytes

Aprotic organic electrolytes consist of a single fluoride salt and a single organic solvent, either based on molecular solvent or ionic liquids.

Ionic liquids (ILs) are promising candidates for FIB electrolytes due to their high chemical and thermal stability. Only a handful of ILs have been reported for FIBs. N,N,N-trimethyl-N-propylammonium bis(trifluoromethanesulfonyl)amide (TMPA/TFSA) has been used as a liquid electrolyte solvent for 1-methyl-1-propyl-piperidinium fluoride (MPPF) salt (Figure 1.4a), cycled against a BiF_3 cathode and a Pb/PbF_2 anode. The electrochemical stability window was found to be surprisingly low, extending from 0 to 0.70 V (vs. Pb/PbF_2). An ionic conductivity of 2.5 mS/cm was achieved, for a maximum soluble concentration of 0.35 mol/dm^3. Furthermore, poor cycling was observed, with a coulombic efficiency of 56% for the first discharge and complete capacity loss by the fifth cycle. A somewhat better electrolyte based on 1-ethyl-3-methylimidazolium Fluorohydrogenate $[C_2C_1Im][(FH)_{2.3}F]$ ionic liquid (FHIL) as both the ionic liquid and fluoride source was also proposed (Figure 1.4b), exhibiting high ionic conductivities in the vicinity of 100 mS/cm.[22] Cyclic voltammetry using CuF_2 as both working and counter electrodes showed overlapping plots over multiple cycles, suggesting some reversible redox reaction, which they suggested was:

$$CuF_2 + 4[(FH)_3F] - +2e^- = 6[(FH)_2F]^- + Cu \tag{1.4}$$

Ten cycles were demonstrated, with the discharged capacity going down from 517 to 264 $mAhg^{-1}$ by the tenth cycle (51.1%), despite the first discharge capacity being 98% the theoretical capacity (528 $mAhg^{-1}$). The columbic efficiency based on the first charge/discharge was found to be 92%. This electrolyte, however, was cycled using symmetric Cu/Cu electrodes, which is likely due to a narrow

electrochemical stability window due to the presence of the hydrogen bifluoride. Furthermore, examining the XRD of the Cu/CuF_2 electrodes after discharging/charging showed the intensity of the CuF_2 barely growing back, casting doubt over the reversible fluorination. They suggested this might have been due to the formation of a CuF_2 amorphous phase or the dissolution of CuF_2 in the ionic liquid.

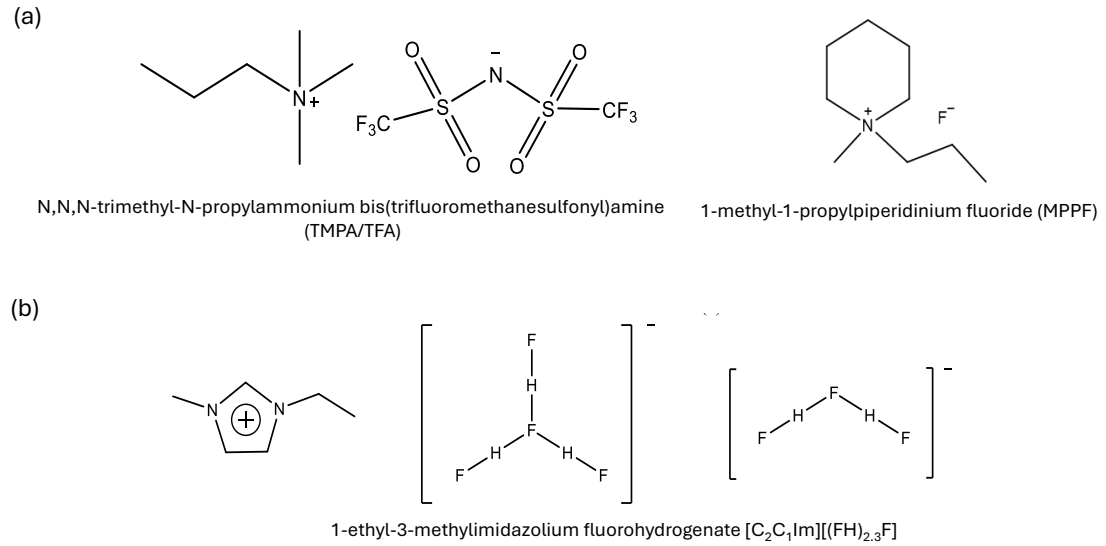
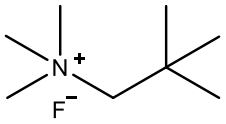


Figure 1.4: Ionic liquids used in FIBs electrolytes. (a) N,N,N-trimethyl-N-propylammonium bis(trifluoromethanesulfonyl)amide (TMPA/TFSA) as an ionic liquid and 1-methyl-1-propylpiperidinium fluoride (MPPF) as a fluoride source. (b) 1-ethyl-3-methylimidazolium Fluorohydrogenate [C2C1im][$(FH)_{2.3}$F] ionic liquid (FHIL).

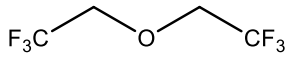
These early IL reports still allow for a much-needed room for improvement, particularly by using more chemically stable fluoride ion sources and ionic liquids with hydrogen donor moieties that can solvate the fluoride ion, enabling solubilities larger than the achieved 0.35 mol/L. Adapting electrolyte systems from the well-developed ionic liquids used in lithium ion battery electrolytes,[39, 40] while maintaining the reactivity and solvation constraints of the fluoride ion, are key to uncovering high performing ionic liquid electrolyte designs.

Unlike ionic liquids which is comprised of two ions, molecular solvents are neutral organic molecules that act as solvents. A single yet notable report of using a fluorinated ether, bis(2,2,2-trifluoroethyl) ether (BTFE), was reported by Davis et al.[41] They tested, separately, two quaternary ammonium fluoride salts, N,N,N-trimethyl-N-neopentylammonium fluoride (Np_1F) and N,N,N-dimethyl-N,N-dineo-

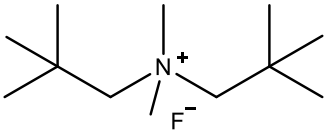
pentylammonium fluoride (Np_2F), both of which prepared through a multi-step synthesis that involved the use of HF. The Np branch was used due to the absence of β-hydrogens and the high branching expected to enhance solubility (Figure 1.5). Based on an initial screening of the chemical and solubility properties of various nonaqueous electrolytes,[42] it was found that BTFE offered the best fluoride solubility (>2.2 M) and chemical stability and was therefore used as the solvent. The 0.75 M Np_1F/BTFE exhibited the highest ionic conductivity of 2.351 mS/cm, and an ESW of 4.1 V (0.7 V to 4.8 V vs. Li^+/Li). They also showed that the cathodic limit could further be extended to 0.4 V by blending linear glycol ethers such as DME with BTFE. This window covered all the high-voltage cathode metals: Cu, Pb and Bi and was at the boundary of the Cerium anode (0.7 V vs. Li+/Li). Ce anode, however, didn't exhibit any reversible fluorination until a CF_n-containing SEI layer was pre-formed by cyclic voltammetry of the cerium anode in 1H,1H,2H,2H-perfluorooctyltriethoxysilane (FOTS). Cu could also not cycle reversibly until it was chemically coated with LaF_3@Cu to form LaF_3@Cu core-shell structure. This was found to be essential in stopping the copper dissolution and enhance the fluoride ion conductivity into the Cu core. Reversible cycling for this LaF_3@Cu versus Ce was, however, reported for only seven cycles, after which the capacity completely faded. Furthermore, a closer look at the ^{19}F NMR showed that BTFE still formed some HF_2^-, but it was not clear whether this was due to a chemical reaction of the fluoride with BTFE or with residual water.[41] Recently, Np_1F and Np_2F were synthesized through a more facile HF-free synthetic route.[43] Still, despite the remarkable solubility and electrochemical stability of BTFE, more work is still needed to understand and expand the fluorinated ether solvents, especially given the low boiling point of 62 °C for BTFE, which limits its use as a practical solvents.



N,N,N-trimethyl-N-neopentylammonium fluoride (Np_1F)



Bis(2,2,2-trifluoroethyl) ether (BTFE)



N,N,N-dimethyl-N,N-dineopentylammonium fluoride (Np_2F)

Figure 1.5: Binary aprotic electrolyte for FIBs based on molecular solvent bis(2,2,2-trifluoroethyl) ether (BTFE) with large-cation tetraalkylammonium fluoride salts N,N,N-trimethyl-N-neopentylammonium fluoride (Np_1F) and N,N,N-dimethyl-N,N-dineopentylammonium fluoride (Np_2F).

Anion acceptors

The most widely investigated and reported liquid electrolytes for FIBs have utilized anion acceptors to dissolve inorganic fluoride salts in organic solvents, particularly boron-based anion acceptors added to CsF in tetraglyme. In this case, the Lewis acid borane, boroxine, or borate (Figure 1.6) binds to the fluoride ion, forming a tetrahedral complex that is more soluble in organic solvents:

$$BR_3 + CsF = [BR_3F]^- + Cs^+ \tag{1.5}$$

The first report of FIB electrolyte based on anion acceptors was of fluorobis (2,4,6-trimethylphenyl)borane (FBTMPhB), with the CsF solubility in tetraglyme increasing from $1.7{\cdot}10^{-4}$ M to 0.47 M upon introducing 0.5 M of FBTMPhB.[44] Other anion acceptors, such as triphenyl boroxine (TPhBX), and triphenylborane (TPhB) were subsequently investigated and resulted in similar increase in solubility.[45] However, this strong fluoride affinity of these anion acceptors also resulted in the dissolution of the BiF_3 active material:

$$BiF_3 + AA = Bi^{3+} + 3AA^- + F^- \tag{1.6}$$

Monitoring the Bi^{3+} concentration profile using Atomic Absorption Spectroscopy (AAS) showed that up to 38 % of active material is dissolved by the end of charging, resulting both in an aggravating capacity loss and an alternative dissolution-deposition cycling mechanism. Furthermore, this dissolution was observed for other metal fluorides such as PbF_2, with the dissolution of the active material at the end of the first charging at 46% for TPhB and 13% for FBTMPhB.[46, 47] However, this dissolution was found to be partially suppressed and the capacity retention improved if saturated CsF electrolytes were used instead of the 0.45 M concentration, resulting in suppressing the BiF_3 dissolution to below 0.04%.[48] In this case, the increase of the CsF/FBTMPhB ratio shifted the complexation of the active material, improving the capacity retention. The same effect of saturating the CsF concentration was also observed with other anion acceptors such as TPhBX.[48]

Furthermore, methods to optimize the electrode performance through controlling the particle size or carbon additives could improve the rate capability and allow the charge transfer to occur before the dissolution of active material. Several reports on optimizing BiF_3 by pre-milling with carbon were shown to retain >100 mAh/g of capacity at the 10th cycle.[49, 50] Similar optimization for the TPhBX electrolyte was also performed for the PbF_2 cathode with acetylene black.[51]

Another approach used to minimize the active material dissolution is the use of alternative anion acceptors known to be stable towards the active material, likely due to their lower binding energies. Lithium bis(oxalato)borate (LiBOB) has been attracting interest in lithium batteries particularly for its ability to suppress active material dissolution, which has been attributed to BOB^- forming a stable SEI layer.[52] The BOB anion can also coordinate strongly to alkali metals through the oxygen bridge, with three possible complexation sites (Figure 1.6).[53] Drawing from this, Abe and co-workers postulated that a similar system can coordinate the Cs cation in CsF while maintaining high cycling performance.[54] It was found that for a 0.5 M (sat) CsF in G4, introducing a LiBOB concentration of 0.5 M dissolved $4.8 \cdot 10^{-2}$ M of CsF, up from $3.5 \cdot 10^{-4}$ M CsF for 0.06 M of LiBOB. To

determine the solvation mechanism, Raman spectroscopy was performed and a peak at 860 cm^{-1} was assigned to the Cs-BOB bond, in agreement with the reported Raman frequency of the metal-glymes (867 cm^{-1} for Cs^+, 865 cm^{-1} for Li^+). The slightly lower frequency observed was attributed to the presence of excess free G4. In using LiBOB with CsF, a competition between Li^+ and Cs^+ is expected, with the ion exchange facilitating the CsF solubility:

$$LiBOB + CsF = CsBOB + LiF \tag{1.7}$$

Here, CsF and LiF are both partially solvated by G4, but the total energy calculated using DFT shows a thermodynamically favorable solvation of the Cs^+ by -0.41 eV energy difference.[54]

Ionic conductivity of the LiBOB(0.5M)/CsF/G4 electrolyte was found to be 2.27 mS/cm and 2.24 mS/cm in the presence and absence of CsF, respectively, suggesting a low fluoride transference number.[54] Linear Sweep Voltammetry (LSV) showed that the peak corresponding to the BOB^- reduction (at -1.7 V vs. ref) persisted after multiple cycles, suggesting that the protective layer on the electrode was not formed, in disagreement with previous results for LIBs. The electrolyte reductive and oxidative degradation started at -2.5 and 0.6 V, respectively, indicating an ESW of 3.1 V. This value is larger than that reported for previous AA/CsF/G4, suggesting some stabilizing effect of LiBOB. However, this could also be a result of using a considerably slower sweep rate (1 mV/s versus 100 mV in previous works[44]).

Other anion acceptors based on borolan-2-yl were also investigated. 4-(4,4,5,5-tetramethyl-1,3,2-dioxaborolan-2-yl)pyridine (DiOB-Py) and the more electron rich and less acidic DiOB-aniline were first investigated with CsF.[55] The ionic conductivity, however, was found to be significantly low, at $3.18 \cdot 10^{-3}$ mS/cm for DiOB-Py/CsF/G4 and $2.71 \cdot 10^{-3}$ for DiOB-An/CsF/G4 using saturated CsF and concentrations of 3900 and 2200 µg/L for the Pyridine and Aniline, respectively. This agrees with the weaker Lewis acidity of these two nitrogen anion acceptors compared to the boron lewis acids, which could have resulted in weaker ion

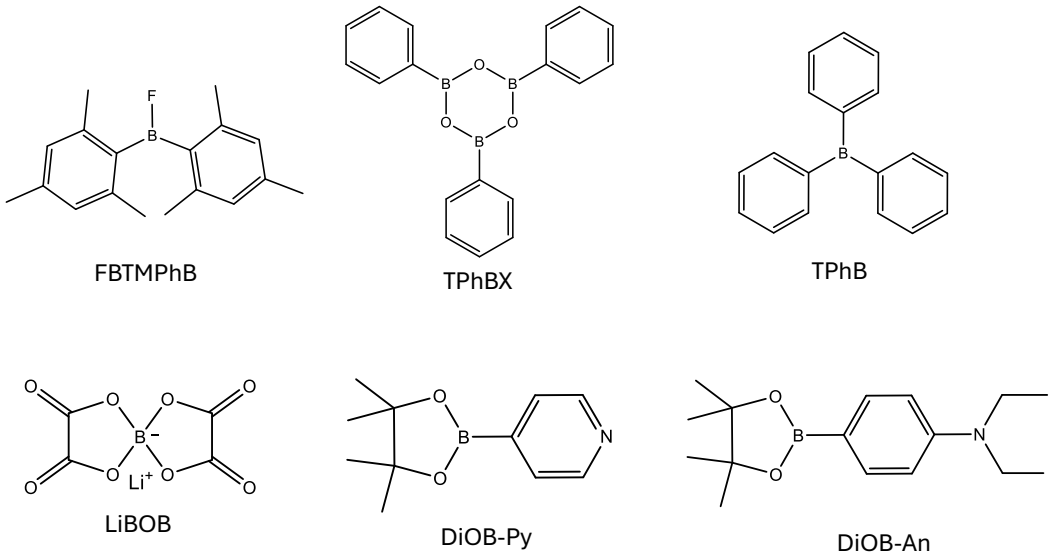


Figure 1.6: Fluorobis (2,4,6 trimethylphenyl) borane (FBTMPhB) Triphenylboroxine (TPhBX) Triphenylborane (TPhB) 4-(4,4,5,5-tetramethyl-1,3,2-dioxaborolan-2-yl)pyridine (DiOB-Py) Lithium bis(oxalato)borate (LiBOB) 4-(4,4,5,5-Tetramethyl-1,3,2-dioxaborolan-2-yl) aniline (DiOB-An).

dissociation and lower ionic conductivity. The ESW was found to be 3.0 and 3.4 V, respectively, for the pyridine and aniline AAs. Running CV for the anion acceptor alone in G4 showed no redox peaks, indicating exceptional electrochemical stability. DiOB-An/CsF/G4 did not, however, show any capacity during cycling, which could be attributed to the low CsF concentration and ionic conductivity, unlike DiOB-Py which showed near full capacity for the first three cycles. Finally, DiOB-Py/CsF/G4 also showed minimal BiF_3 dissolution (<0.1 µg/L) after full discharge/charge, suggesting minimal capacity loss due to the dissolution of active material and a conversion mechanism instead of the dissolution-deposition mechanism previously observed in AA/CsF/G4 electrolytes.[56] In a subsequent study, DiOB-Py with saturated solution of lower molecular weight fluoride sources NaF and KF was investigated.[57] NaF showed insufficient solubility and a low ionic conductivity that prevented cycling, while KF showed more promising cycling capability of up to 30 cycles, an ESW of 3.2 V, and an ionic conductivity of $1.02 \cdot 10^{-2}$ mS/cm.

In summary, comparing these different anionic acceptors, FBTMPhB, TPhB

and TPhBX showed very similar performance, except for the large and unexplained difference in PbF_2 dissolution between FBTMPhB and TPhB in two reports by Konishi et. al.[46, 47] In a different report, TPhB was shown to have superior performance and less PbF_2 dissolution than TPhBX, and was concluded to be the best among the three aforementioned anionic acceptors.[58] This trend might be partially explained by the difference in binding energy as calculated by DFT: 312.3 kJ/mol for FBTMPhB, 324.3 kJ/mol TPhB, and 335 kJ/mol for TPhBX.[58] The performance of TPhBX and Py-DiOB was compared at the same AA concentration and BiF_3 milling condition, and both the charge and discharge capacities were found to be higher in Py-DiOB despite its lower saturation CsF concentration.[55]

Although they have been examined more extensively, anion acceptor electrolytes based on CsF in tetraglyme suffer from some serious limitations that hinder their deployment in high voltage and reversible FIBs. The active material dissolution, the low concentration of <0.5 M, and the need for large (equimolar) amounts of anion acceptor all limit their practical use in FIBs. But more importantly, the limited ESW of 2 to 3 V hinders the use of high operating voltage electrode pairs, which are crucial for utilizing the high energy density of fluoride ion batteries. Still, a lot can be done to explore the effects of the electronics and binding energies along with the steric effects of the Lewis acid in order to find the optimal acceptor that can bind to the fluoride in solution but not in the cathode, particularly given the wide array of Lewis acids used for fluoride sensing and recognition, many of which are still unexplored in the FIB context.[59]

More recently, anion acceptors with milder fluoride affinity were attempted, namely based on imino and sulfone fluoride acceptors.

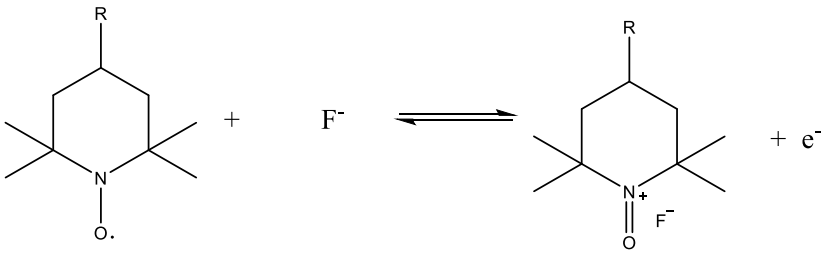
Aqueous and Protic Electrolytes

The first reported FIB based on aqueous electrolyte used a NaF dual-ion electrochemistry that utilized both fluoride and sodium shuttles. During charging, fluoride and sodium ions are released from the anode and cathode, respectively, with

BiF_3 used as an anode and sodium manganese oxide, $Na_{0.44}MnO_2$ (NMO), as a cathode.[60] A NaF concentration of 0.8 M, slightly short of the saturation concentration of 0.96 M, was used to suppress the dissolution of the metal fluoride anode. Cycling exhibited a poor coulombic efficiency of 51.95% for the first cycle most likely due to the formation of the SEI, with the efficiency for the subsequent cycles reaching 99% with a reversible capacity of 47.28 $mAhg^{-1}$ maintained over 40 cycles. This rate capability and stable cycling is an improvement over the organic based systems, which could only cycle for 10-30 cycles. The cyclability was further improved to 109.5 $mAhg^{-1}$ for 80 cycles when an anode configuration of BiF_3 on carbon nanotubes (nano-Bi@CNTs) was employed.[61] In another report of an NaF aqueous electrolyte, a flow battery based on BiF_3 anode and a 4-hydroxy-TEMPO catholyte was used[62]:

Negative Electrode: $BiF_3 + 3e^- \rightleftharpoons Bi + 3F^-$

Positive Electrode:



Performing CV for separate solutions of NaF with both 4-hydroxy-TEMPO and BiF_3 at the two working electrodes shows the former has a one-electron redox couple while the latter has two, corresponding to both the $0 \rightarrow 2$ and $2 \rightarrow 3$ transitions of Bismuth. Furthermore, the BiF_3 showed an additional reduction peak at the first cycle which was attributed to the formation of an SEI. XRD imaging of the discharged and charged states showed some BiF_3 peaks persisting after charging indicative of an incomplete reaction, unlike previous aqueous NaF electrolytes.[62] Analyzing the HRTEM diffraction fringes of the BiF_3 at the charged and discharges state showed the formation of bismuth oxyfluoride (BiOF and $Bi_7F_{11}O_5$) as seen in the XRD pattern, possibly due to the presence of water

in the electrolyte. The FTIR spectra of 4-hydroxy-TEMPO catholyte showed the disappearance of the 1167 cm^{-1} N–O peaks and the appearance of the 1542 cm^{-1} N = O confirming the reduction. In a recent paper, the cycling performance of aqueous FIBs was taken to a new level, where the cycling of 1 M aqueous KF was performed reversibly for 1000 cycles while retaining 76.3 mAh/g of the capacity.[23] This performance was enabled by the introduction of a 'buffering' phase for $Bi_7F_{11}O_5$ during the cathode preparation. This bismuth oxyfluoride was shown by DFT to have smaller volume change and smaller electronic band gaps compared to BiF_3, resulting in a more stable configuration and facile charge transfer and higher electronic conductivity during cycling.[23]

More recently, electrolytes based on protic solvents have also emerged. For instance, a highly concentrated TMAF in methanol solution with propionitirile (PN) as a diluent was developed as a ternary FIB electrolyte.[63] This inspired further work into alcohol-mediated fluoride solvation, such as the use of benzyl alcohol to promote the solubility of CsF in N, N-dimethylacetamide (DMA), achieving an ionic conductivity of 2.05 mS cm^{-1}.[64] Another report used ethylene glycol (EG) as a fluoride solvent with choline chloride (ChCl) as a solvation regulator for CsF to form a eutectic with EG, giving rise to an ionic conductivity of 2.17 mS cm^{-1}.[65] A similar design, based on choline fluoride and EG, claiming a wider stability window compared to ChCl.[66] Deep eutectic solvents based on amides were also investigated, where the N-H bond in 1,3-dimethylurea (DMU) and TMAF were mixed to depress the melting point and form a high concentration electrolyte of 2.6 mol/L, obtaining an ionic conductivity of 0.41 mS cm^{-1}.[67] However, all these electrolytes had ESW of 2-3 V, limited by the electrochemical stability of the protic solvent.

1.2 The Fluoride Ion chemical and solvation properties

Despite the previous work on designing liquid electrolytes for FIBs, the state of the art systems are still far from practical, particularly in terms of their solubility and (electro)chemical stability, let alone other features such as SEI formation which has been rarely if at all investigated. The design of new fluoride electrolytes necessitates a thorough understanding of the physicochemical properties of the fluoride ion, starting from the fluoride-ion salts, the fluoride reactivity, and the fluoride solvation.

The fluoride ion is the smallest single charged anion with a radius of 119 pm (compared to 90 pm for Li^+). Due to the fluorine atom exhibiting the highest electronegativity in the periodic table, the fluoride ion forms strong hydrogen bonds to electron deficient hydrogen atoms (O-H, N-H, and even C-H in the presence of electron withdrawing groups). Furthermore, the fluoride ion can, based on the reacting species, be a formidable nucleophile and base, capable of undergoing substitution, condensation and elimination reactions:

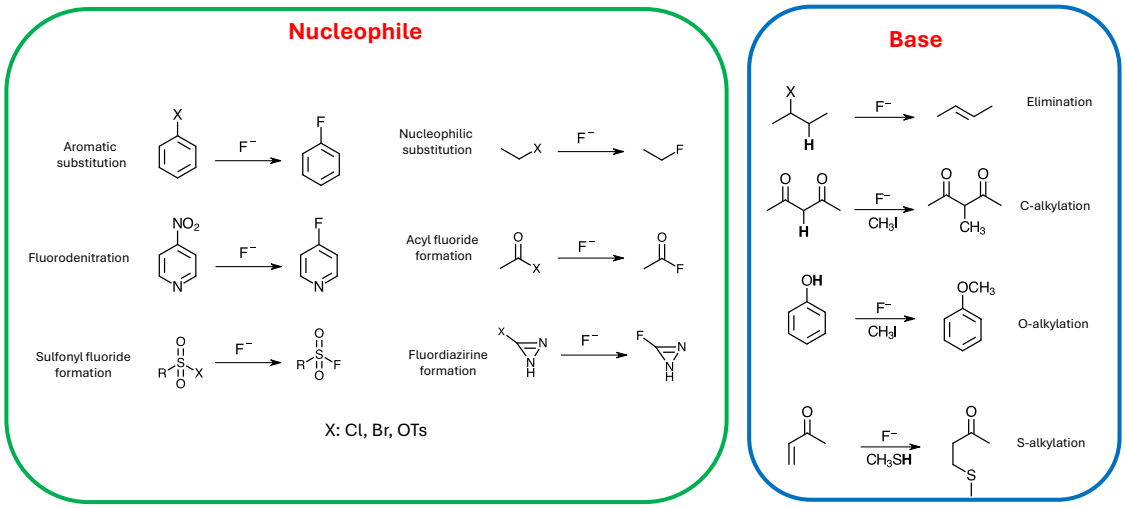


Figure 1.7: Fluoride ion reactivity schematic.

The fluoride ion can also etch glass but only due to the formation of small amounts of HF, hence many reports still using glassware with the fluoride ion

with impunity.[68]

Fluoride ion can also form hydrogen difluoride, HF_2^-, in slightly acidic mediums. HF_2^- (i.e., FHF^-) is a linear ion with a D_h point group symmetry, where the bivalency of the proton is enabled by the strong hydrogen bond donation. The molecular orbitals (MOs) of HF_2^- can be constructed from the sum of the HF and F-orbitals. However, hydrogen bifluoride is not a direct fluoride-hydrogen fluoride adduct, as indicated by the two equivalent H-F bonds. The atomic orbitals of fluorine involved in the bonding and anti-bonding of F_2 are the same as those in HF_2^- (2s and 2p) with the same symmetry (B_{3u}, B_{2u} and A_g, for the bonding $2p_x$, $2p_y$ and $2p_z$/2s orbitals, respectively), only separated by the central proton, which allows its 1s A_g to bond with the $2p_z$ and 2s A_g orbitals of fluorine. Given the closer energy match of the hydrogen 1s orbital (-13.6 eV) to the $2p_z$ fluorine orbital (-18.7 eV) compared to the 2s orbital (-40.2 eV), stronger interaction occurs with the former. The H-F bond energy of HF_2^- is 212 kJ/mol and the bond distance 114.5 pm, compared to a bond energy and distance of 574 kJ/mol and 91.7 pm in HF.[69] The lower bond energy in HF_2^- is due to the bonding MOs extending over three atoms. The HF bond in difluoride is therefore claimed to be the strongest.[70]

1.2.1 The 'naked' fluoride dilemma

The term naked fluoride have typically been used to describe fluoride ions that are stripped off any hydrate or protic (e.g., alcohol) solvates. Due to the strong hydrogen bonding of fluoride and its tendency to exist in solvates, obtaining such ions has been a tremendous challenge. The term first referred to fluoride ions in aprotic polar solvents where ion pairing was minimized by complexing the counter cation, for instance using a crown ether to coordinates to Cs^+ in CsF.[71] Strictly speaking, however, fluoride ions cannot exist in solution without some level of interaction with the solvent and some level of ion pairing, and truly naked fluorides can only exist in the gas phase.

Still, an estimate of the cation-anion distance, and hence the size of the cation, can be indicative of ion pairing and the level of the fluoride 'nakedness'. CsF has traditionally been used to approximate a naked fluoride source due to its larger cation-anion distance and smaller ion pairing relative to NaF and KF, but this suggests that even more naked fluorides can be obtained if dry fluoride salts with larger counter cations are prepared. For instance, it was claimed that phosphazenium fluorides are more naked than tetramethylammonium fluoride (TMAF) due to the larger size and cation-anion distance (630 and 420 pm, respectively).[71] However, it was also found that the activity of the fluoride ion described as naked, such as CsF solubilized by crown ethers, was still much lower than expected due to ion pairing.[72] Therefore, the term 'non-hydrated' fluoride was proposed instead,[73] despite some reports still referring to synthesizing 'naked' fluoride salts.

Even in their hydrogen-bonded solvates, varying the solvating molecule can provide a method for controlling the fluoride activity. For instance, the fluoride reactivity in fluorination reactions correlated directly with the bulkiness of the solvating molecule (t-BuOH > i-PrOH > n-BuOH n-PrOH > H2O).[74] Furthermore, bulkier solvates provide a more selective fluoride ion in substitution reactions, overcoming the side elimination reaction, and investigating the coordination environment in these crystal solvates showed the fluoride to be predominately surrounded by four alcohol molecules.[75] In another study by Engle et. al, fourteen alcohol-fluoride complexes were studied and it was found that tri- and dicoordinate fluoride-alcohol complexes existed for even bulkier alcohols. It was postulated that this variation in the coordination number, and in the bond angles and lengths, would influence the activity of fluoride upon dissociation in solution.[76] In summary, these results indicate that the coordination number of fluoride-solvate complexes range from two to four, decreasing with the degree of branching and size of the solvating molecule.

The ability of fluoride ions to form hydrogen bonds should also be cross examined with its reactivity towards acidic hydrogens. Given that hydrogen bonding

is stronger for acidic hydrogens, it is possible that hydrogens below a certain pK_a threshold are abstracted by the fluoride ion to form hydrogen (bi)fluoride. A rough screening by Davis et. al. suggested that deprotonation in nonaqueous mediums occurred at pKa < 33.[42] This is evident, for instance, in the slow but growing formation of hydrogen fluoride in solutions of fluoride in acetonitrile (pKa 25).[42] Despite this instability, acetonitrile has been widely reported as a solvent for fluoride ions in syntheses of fluoroorganics.

1.2.2 The Fluoride Salts

The various fluoride salts are often classified based on the nature of the counter cation, which can significantly influence the solubility, hygroscopicity, and (electro)chemical stability of the given salt.

alkali metal fluorides

Alkali metal fluorides are the most abundant, stable, and cost effective of the fluoride salts. The relatively small size of the counter cation, however, results in lower solubility due to the larger ion pairing, but it also results in less hygroscopicity, with both the solubility and hygroscopicity increasing with molecular weight (RbF > CsF > KF > NaF).[68] Solubility measurements for alkali metal fluorides in nonaqueous solvents are, however, scarce and inconsistent, with values differing in some cases by 2-3 order of magnitudes.[77] This could be a result of variations in the methods used in the solubility measurement and in the water content of the nonaqueous solvents. Using methods such as conductance, for instance, can be affected by ion pairing where solubility is underestimated due to the absence of freely moving ions. Differences in water content from 100 to 400 ppm was shown to double the saturation concentration.[78] A more systematic and reproducible report of solubility measurements obtained by flame spectroscopy of saturated solutions of alkali-metal fluorides showed that the solubility did not exceed 1 mM even for the most soluble of salt/solvent systems.[78]

Solubility of LiF and NaF measured by potentiometric titration using fluoride ion-selective electrodes revealed that both salts had slightly lower solubility in alcohols than in water, with a Gibbs free energy of 18 kJ/mol for the water-to-methanol phase transfer. Much smaller solubilities (and more positive $\Delta_t G$ values) were observed when acetonitrile (AN) was used instead of the alcohol, despite acetonitrile's higher dielectric constant which is expected to have minimized ion pairing, highlighting the importance of hydrogen bonding in solvating the fluoride ion.[79] Still, some solubility trends still need explanation, such as unexpectedly higher solubility of CsF compared to RbF (e.g., in AN), and the exceptionally high solubility of LiF despite the significant ion pairing expected.

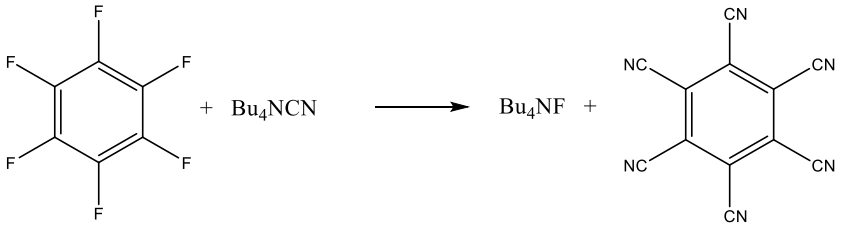
Quaternary ammonium fluorides

Tetraalkylammonium fluorides can be a promising source of fluoride due to their higher solubility compared to alkali metal fluorides. In fact, further increase of the cation size even among quaternary ammonium fluorides was shown to significantly increase the solubility. In a report by Davis et. al.,[41] the solubility was increased by 3 folds going from Tetramethyl ammonium fluoride (TMAF) to a slightly more branched cation with neopentyl (Np) side chains.

TMAF is the simplest of the quaternary ammonium fluoride salts and is known to be stable towards oxidative attacks due to the distribution of the positive charge over 12 hydrogen atoms.[71] In a study of tetramethyl ammonium salts with various counter anions, the reduction potential limit was found to be in the vicinity of -2.90 to -2.70 V vs. SCE (0.38 to 0.58 V vs. Li^+/Li).[80] Furthermore, TMAF is a more potent source of fluoride ions compared to CsF, due to its higher solubility. In a study by Schimler and co-workers, it was found that anhydrous TMAF in dimethylformamide (DMF) was a more effective S_NAr fluorinating agent at RT compared to CsF even at elevated temperatures, as evident by the higher reaction yield, with the reaction solution was prepared by stirring 0.2 M of TMAF in DMF for 24 h.[81] In another study, TMAF dissolved in either DMSO or DMF was also found to be an effective base for alkyl halides elimination, even at mild

conditions.[82] This mild fluorination agent, TMAF in DMSO, was also shown to be capable of performing aromatic substitutions for even the nonactivated halo arenes if catalyzed by a Pd complex.[83]

Larger quaternary ammonium fluorides can have larger solubility and a more naked fluoride source, and are thus more effective bases and nucleophiles, despite their potential instability if they possess β-hydrogens. Tetrabutyl ammonium fluoride (TBAF), for instance, is known to be less thermally stable than TMAF due to the presence of β-hydrogen, which upon heating to 77 °C undergoes Hoffmann elimination to give tributyl amine, 1-butene, and tetra butyl ammonium bifluoride.[84] This decomposition was shown to still occur, although more slowly, at room temperature for both solid and in-solution TBAF.[85] Partially anhydrous (0.1 - 0.3 molar equiv H_2O) TBAF, however, could be obtained if the hydrate is heated under high vacuum at 40 °C, and was found to be an effective fluoride source allowing S_N2 reactions at mild conditions, where the substrate was directly added to the oil-like ”anhydrous” TBAF.[86] Another neat method for the preparation of more rigorously anhydrous TBAF was developed by Sun and DiMagno, where anhydrous and highly soluble TBAF was prepared in-situ from hexafluoro benzene and tetrabutylammonium cyanide dissolved in THF, DMSO or acetonitrile, and was used as a fluoride source in room-temperature S_NAr reactions:



The anhydrous TBAF salt was precipitated and obtained free from the aromatic side products by cooling down the reaction mixture to -65 °C, and was found to be soluble in nonpolar aprotic solvents up to 2 M, with minimal (<4%) hydrogen difluoride formation.[85] TBAF solutions were, however, found to decompose slowly (within hours to days) at temperatures above 0 °C. Given the

facile nature of the S_NAr performed here (a few minutes to 6 h), this was not an issue. However, for liquid electrolytes, this method would have to be used with more stable quaternary ammonium cations. Despite the instability of TBAF, these drying and in-situ preparation methods can potentially be extended to other more stable counter cations.

Other larger quaternary ammonium salts based on bi- and tricyclic tetraalkylammonium fluoride salts have also been synthesized and investigated; 1-methylhexamethylenetetramonium fluoride (MHMTAF) (Figure 1.8) was first synthesized by quaternizing the amine using methyl iodide followed by a fluoride metathesis using silver fluoride.[87] Another report of a single-step, one-pot synthesis of MHMTAF was reported by Gnann et. al., starting from methylamine, formaldehyde, HF and ammonia solutions, where subsequent azeotroping of the water-isopropanol mixture gave anhydrous MHMTAF.[88] In another report, anhydrous N, N, N-trimethyl-1-adamantylammonium fluoride (TMAAF) (Figure 1.8) was synthesized by the metathesis of the corresponding chloride and KF in alcohol, where the TMAACl salt was synthesized from N,N-dimethyl-l-adamantamine and methyl chloride in ether solvent.[89] N-methylquinuclidinium fluoride (NMQF) (Figure 1.8) was also synthesized in the hemihydrate form.[90] The synthesis was carried out by treating quinuclidine with methyl bromide in ethanol while cooling to 0 °C, yielding MQBr. Treating MQBr with silver oxide (Ag_2O) resulted in the corresponding hydroxide (MQOH), which was converted to the fluoride salt upon treatment with 5% HF. In all these fused cycles, the bridgehead methylene group did not undergo Hoffmann elimination due to Bredt's rule, where double bonds do not form on bridgeheads given the resulting ring strain.

Two more quaternary ammonium fluoride salts, 1,1,3.3,5,5-Hexamethylpiperidinium fluoride (HMPAF) and 1,2-dimethylpropyltrimethylammonium fluoride (DMPTMAF) (Figure 1.8), with larger cation sizes were synthesized by Mahjoub et. al. to enhance the solubility.[91] Both salts lacked β-hydrogens and were found to be soluble in fluorohydrocarbons even at low temperatures, and their fluoride activity was demonstrated by forming highly coordinated Se and Br com-

plexes. Finally, anhydrous quaternary ammonium fluoride salts based on azabicyclo[2.2.2]octane skeleton, similar to the NMQF but with X = N, NCH_3^+, or CPh, could also be achieved, in this case prepared using fluoride ion exchange resin.[92]

More complex, chiral tetraalkylammonium fluorides could also be prepared and were originally used for enantioselective fluorination, and are expected to be even more soluble due to the larger ion mismatch, although possibly at the expense of thermal and electrochemical stability. In an early report, binaphthyl-derived quaternary ammonium fluorides (BINAF) (Figure 1.8) was obtained in-situ by mixing the corresponding hydrogen sulfate salt with excess KF in toluene, generating inhomogeneous fluoride source that was used in Michael addition.[93]

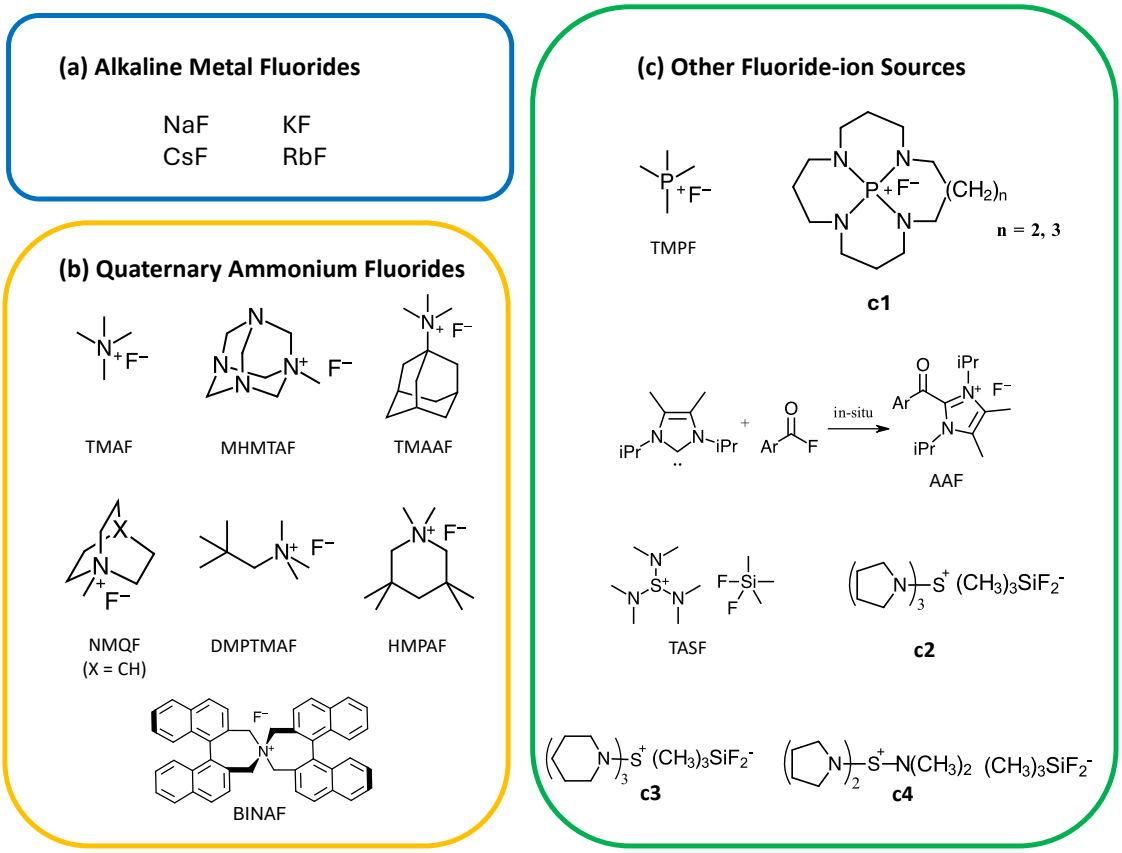


Figure 1.8: The fluoride ion sources characterized by the counter-cation into (a) alkali metal fluorides, (b) quaternary ammonium salt, and (c) other fluoride-ion sources including phosphonium, acyl azolium, and sulfonium-based fluorides.

Other Fluoride Sources

Other fluoride salts, such as those based on quaternary phosphoniums, have also been synthesized due to the more naked fluoride source they provide owing to their larger cation-anion distance. Quaternary phosphonium fluorides (R_4PF) can exist in both molecular or ionic forms. As the molecular form is non-hygroscopic, it can be prepared with minimal water content then converted to the ionic form, as adjusting the polarity of the medium induces the ionic nature.[94] This method has been shown to be partially successful for tetraphenyl phosphonium hydrogen difluoride, which was prepared and dried easily and was found to be highly soluble in aprotic solvents.[95] Interestingly, the hydrogen difluoride in these phosphonium salts was found to be geometrically distorted due to the larger size of the countercation, which resulted in a more active fluoride source.[96] Tetramethyl phosphonium fluoride (TMPF) (Figure 1.8c) was also prepared in an anhydrous form, although in a four-step synthesis, and was found to be stable up to 120 °C with some solubility in non-protic solvents such as THF, benzene and ethers.[97] Cyclic phosphonium fluoride salts (Figure 1.8, **c1**) were also shown to be an effective fluoride source and could neatly perform S_NAr.[98]

Furthermore, anhydrous acyl azolium fluorides (AAFs) were prepared by Ryan et. al. with the objective of obtaining anhydrous, soluble fluoride sources for room temperature S_NAr reactions in polar aprotic solvents, and were synthesized rapidly in-situ from the N-heterocyclic carbene (NHC) and acid fluoride (Figure 1.8c).[99] Furthermore, the choice of the carbene was found to enable tuning the nucleophilicity of the fluoride ion, where replacing the hydrogen with methyl groups in the imidazolium ring suppresses the fluoride nucleophilicity due to the elimination of hydrogen bonding, whereas using more electron rich acid fluorides (methoxy substituted arenes) enhanced the fluoride nucleophilicity and improved the S_NAr reaction yield compared to the trifluoromethyl substituted arenes. In this reaction, a concentration of ca. 0.6 mol/L of the acyl fluoride and the NHC in DMF at room temperature were used.

Another unconventional fluoride ion source is tris(dimethylamino)sulfonium trimethyldifluorosilicate (TASF), which was found to dissociate readily in the presence of a hydrogen bond acceptor, providing a fluoride ion.[100] It was also found to exhibit reasonable solubility in aprotic polar solvents such as THF and ethers. Other trimethyldifluorosilicate salts with different sulfonium counter cations (Figure 1.8, **c2 - c4**) were also demonstrated in the original work describing this fluorinating agent.[101]

1.2.3 Fluoride Ion Solubilizing Systems

To increase the solubility of the fluoride ion in nonaqueous media, fluoride ion receptors can be used to coordinate to the fluoride ion or to the counter cation in order to increase ion separation. This guest-host interaction can be based on a macrocyclic structure with strong interaction with either the fluoride ion or the countercation, a Lewis acid with high fluoride affinity, or a solid media that can support the fluoride salt.

Macrocyclic Fluoride Receptors

Relatively little understanding exists for anion-complexing compared to cation-complexing using macrocyles such as crown ethers, cryptands, cavitands and spherands.[102, 103] 18-crown-6, for instance, was shown to solubilize KF even in nonpolar solvents (benzene), and the activity of the fluoride ion was demonstrated by S_N2 and S_NAr reactions, showing reaction yields between 60-90%.[104] Plotting the KF solubility versus the crown ether concentration showed a straight line passing through the origin, indicating that solubilization is independent of the solvent's dipole moment and is limited only by the solubility of the crown ether (1.5 M in benzene and 0.2 M in acetonitrile).[104]

Besides cation-complexing macrocycles, another less explored field is the use of macrocycles with strong hydrogen bond acceptor methylene groups to coordinate the fluoride ion (Figure 1.9a), with the CF_2 acting as a strong electron

withdrawing group to increase the hydrogen bond accepting ability of the adjacent methylene hydrogens, and thus the fluoride ion affinity.[100] The fluorinated macrocycle was prepared using a multi-step synthesis starting from the commercially available 2,2,3,3,4,4-hexafluoro-1,5-pentanediol and perfluorocyclobutene. The fluorinated macrocycle exhibited exceptional fluoride binding ability, where treating the macrocycle with an equimolar amount of fluoride-ion produced the fluoride-nesting complex quantitatively. Analyzing the X-ray structure of the fluoride adduct showed a nesting complex with a cup-shaped cavity, with the fluoride binding to the four hydrogen atoms. The synthesized fluorinated macrocycle was inspired by a pioneering series of papers by Larson and McMahon on the C-H hydrogen bond interaction with the fluoride ion in the gas phase, in which they proposed macrocycles as a possible method for solubilizing fluoride salts in organic solvents.[105–107]

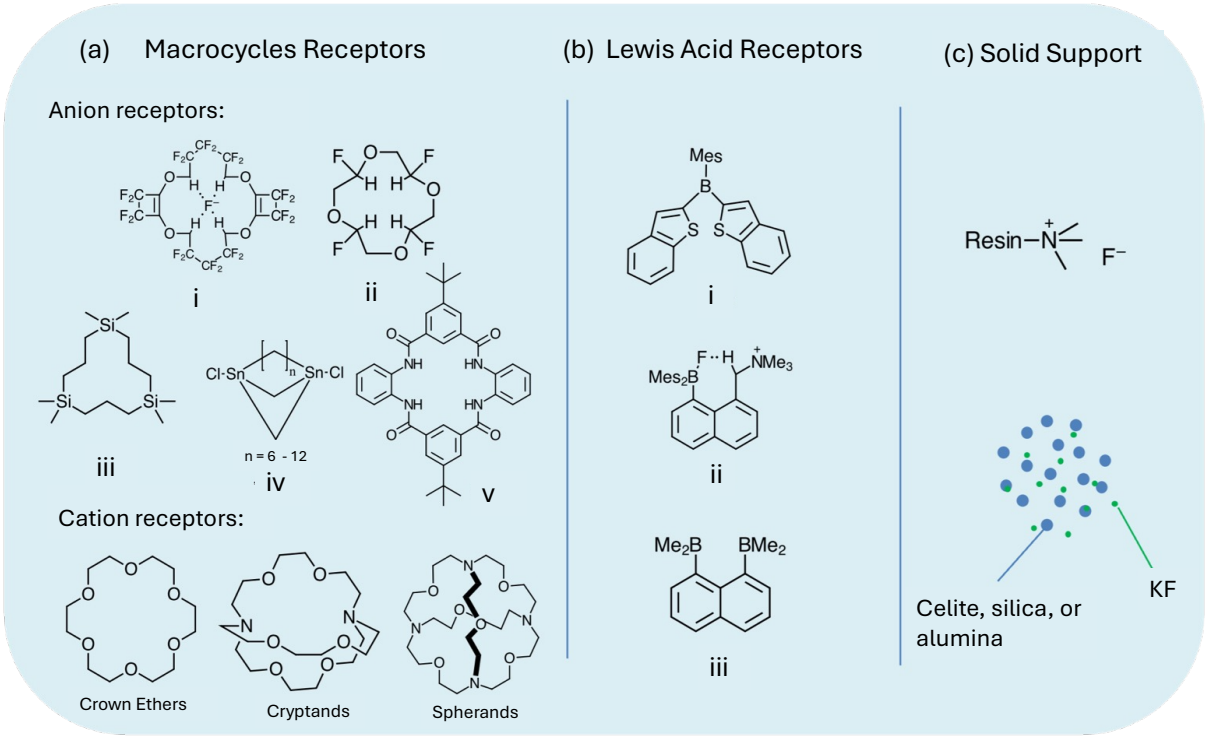


Figure 1.9: Fluoride ion solubilizing systems, (a) Macrocyclic receptors, (b) Lewis Acid Fluoride Receptors, and (c) Solid-state supports.

Macrocycles with Lewis acidic tin bridgeheads (Figure 1.9, **iv**) were also shown to selectively bind to the fluoride ion while maintaining structural integrity. Here

the fluoride selectivity was controlled by the cavity size as determined by the number of methylene groups (n), where it was found that n = 6 corresponded to fluoride-ion selectivity whereas n = 8 and n = 10 showed stronger interaction with the chloride ions. [108] Macrocycles based on silicon, 12-silacrown-3 (Figure 1.9, iii) were also prepared in a multi-step, yet facile, synthesis, but no fluoride transport was observed compared to other halides, suggesting poor interaction or unoptimized cavity size match.[109]

Finally, a potentially promising macrocyclic fluoride recognition system is tetralactam, which was recently prepared in a one-pot synthesis and shown to have high fluoride ion affinity, attributed partly to the formation of a double-saddled complex (Figure 1.10).[110] This work builds on and uses the most soluble tetralactam from a broader study on tetralactam reagents (Jurczak's receptors).[111–114]

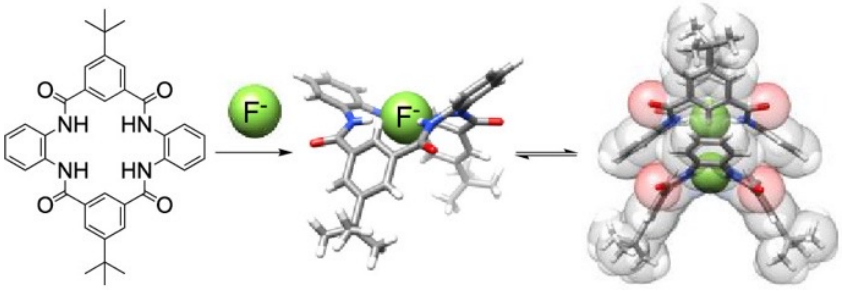
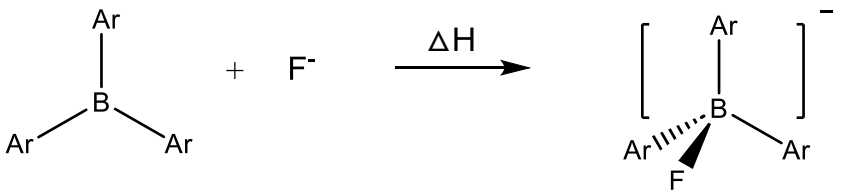


Figure 1.10: Tetralactam fluoride-ion receptors use a double-saddled complex and hydrogen bonding to coordinate the fluoride ion. Adapted from [110].

Lewis acid receptors

Lewis acids, especially those based on boron, have been widely employed as fluoride-ion receptors, with applications mainly for fluoride sensing but also as FIB electrolytes. Thermodynamically, triaryl boranes have large fluoride ion affinity as evident by the exothermic binding reaction:



This fluoride ion affinity (described by $-\Delta H$) was found to decrease as the borane substituents become bulkier, due to the induced repulsion during the formation of the tetrahedral complex.[115] Furthermore, the fluoride affinity can be enhanced by employing more electron withdrawing substituents, as evident by the very short B-F bond (1.43 Å) and the large binding constant of $[(C_6F_6)_3B]F^-$.[116] Extending the π-conjugation also proved to enhance the fluoride affinity, mainly by lowering the LUMO of the boron atom and thus increasing its Lewis acidity, as shown in the large binding constants of benzothienyl derivatives (Figure 1.9b, **i**).[117] Other methods to enhance the fluoride affinity also include using cationic pendant functionalities (Figure 1.9b, **ii**).[118] This cationic borane was found to exhibit exceptional fluoride binding ability due to the formation of intramolecular hydrogen bonding. Bidentate boranes (Figure 1.9b, **iii**) were also shown to enhance the fluoride ion binding.[119]

Only a fraction of these Lewis acids studied for fluoride ion recognition has been used in fluoride ion electrolytes, leaving room for investigating and balancing the electronic and structural factors to maximize the fluoride ion transport in electrolyte solvents, while also keeping an eye for active material dissolution that might result from the large fluoride affinity.

Solid Supported fluorides

Fluoride salts can also be hosted in solid supporting materials with potentially less hygroscopicity and more thermal stability.[68] Fluoride supported on anion-exchange resins, where a quaternary ammonium group is bonded to a polymeric material, can be used as a medium and source for fluoride ion. It was shown, for instance, that an Amberlyst-A 26 resin with tetraalkylammonium (Figure 1.9c) could effectively fluorinate primary and secondary alkyl halides or sulfonates under mild conditions and in the presence of a solvent such as acetonitrile.[120] In another report, a wider array of fluorinated resins (A-26, A-27, MSA-1 and IRA-900) were used with aprotic solvents such as THF, DMF and benzene.[121] In these reports, the support is based on a polystyrene resin, and the reaction is

run by adding the reactive substrate to a mixture of the polymer powder and the solvent (typically in 1:1 v/v) after which the suspension is stirred for 24h at RT, followed by filtering the product and regenerating the resin. Celite, the naturally occurring sedimentary rock also known as diatomaceous earth, can also act as a supporting material for fluoride ion (Figure 1.9c). KF-celite was formed by mixing the two powders in water, followed by drying at 60 °C under vacuo, achieving a fluoride activity that was demonstrated by C-, N-, O- and S- alkylation. This method was also demonstrated for other supporting materials such as silica and alumina, and provided a more thermally stable and less hygroscopic fluoride source.[122] While these systems were typically used for fluorination reactions, it might be possible to extend into electrolytes for FIB electrolytes.

1.3 Thesis Objectives

Unlike other more mature electrochemistries such as Li and Na, the fluoride-ion battery still needs fundamental understanding and development at every level and component of the battery (electrolyte, cathodes, anodes, interphases). Between all of these uncharted territories, the development of room-temperature electrolytes is, we believe, the greatest obstacle in the development of high-energy density FIBs. The objective of this work is to tackle this from two angles:

Part 1 (Chapter 1): explore the limits of protic solvents as FIB electrolytes, namely to exploit their higher fluoride solubility to obtain more electrochemically stable electrolytes, and to investigate the solvation, transport, and proton transfer of such electrolytes.

Part 2 (Chapter 2): Ultimately, aprotic solvents will be needed to achieve satisfactory electrochemical stability windows (> 4 V). This chapter explores the fluoride solvation and chemical stability in aprotic solvents, then presents an expanded and detailed study of 1,3-dimethylimidazolium TFSI as a potential solvent due to its unprecedented solubility.

Besides electrolytes, the FIB critically lacks a stable reference electrode and a cathode with sufficiently high capacity and cycling stability.

Part 3 (Chapter 3) presents a Ag/Ag^{+} reference electrode fabrication and electrochemical testing, along with the synthesis of mono-disperse copper nanocubes to mechanistically study the (de)fluorination of CuF_2 cathodes, long considered the holy-grail of FIB conversion cathodes.

2

Methods Fundamentals

Contents

2.1 Electrochemical Methods 38

2.1.1 Electrochemical impedance spectroscopy 38

2.1.2 Cyclic Voltammetry 42

2.1.3 Galvanostatic Cycling 44

2.1.4 Electrodes and Coin Cell Fabrication 45

2.2 Solvation Structure 46

2.2.1 Total Neutron Scattering 46

2.2.2 Molecular Dynamics (MD) simulations 48

2.2.3 Density Functional Theory (DFT) 48

2.3 Chemical Analysis 49

2.3.1 Nuclear Magnetic Resonance (NMR) 49

2.3.2 Pulse-field Gradient (PFG) NMR 52

2.3.3 ICP-MS 54
2.3.4 Differential Scanning Calorimetry (DSC) 55
2.4 Solid-state Structure Characterization 56
2.4.1 (In-situ) Transmission Electron Microscopy (TEM) . . . 56
2.4.2 X-ray Photoelectron Spectroscopy (XPS) 57

2.1 Electrochemical Methods

2.1.1 Electrochemical impedance spectroscopy

Electrochemical impedance spectroscopy (EIS) is a powerful technique used to measure a wide range of electrochemical parameters, such as ionic conductivity and charge-transfer resistance. In EIS, electrical equivalent circuits (EECs) are constructed as theoretical analogs to the electrochemical system under study. Resistors and capacitors, for instance, are used to approximate the solution resistance and the double layer capacitance at the electrolyte/electrode interface. The voltage response for these EECs can be expressed as:

$$V_{inductor}(t) = L\frac{dI}{dt} \tag{2.1}$$

$$V_{resistor}(t) = RI \tag{2.2}$$

$$V_{capacitor}(t) = \frac{1}{C}Idt \tag{2.3}$$

The time response, however, is not practical given the variable timescales of the various processes occurring simultaneously in an electrochemical system. Fourier transform is thus performed to obtain the voltage in the frequency domain:

$$V(t) \Rightarrow \tilde{V}(\omega) \tag{2.4}$$

The impedance can then be defined as the frequency-equivalent of resistance, R. From Ohm's law, this can be obtained by dividing the voltage by the current, both in the frequency domain:

$$Z(\omega) = \frac{\tilde{V}(\omega)}{\tilde{I}(\omega)} \tag{2.5}$$

From equations 2.1 - 2.3, the impedance for each of the three basic circuit elements can be expressed as:

$$Z_{resistor}(\omega) = R \tag{2.6}$$

$$Z_{capacitor}(\omega) = \frac{1}{i\omega C} \tag{2.7}$$

$$Z_{inductor}(\omega) = i\omega L \tag{2.8}$$

Since Fourier transform is a linear operation, the impedances for different EECs can be combined in series or in parallel the same way resistors are combined. In potentiostatic EIS, voltage is applied sinusoidally at varying frequencies and the current response is measured. The impedance is then calculated, and the imaginary (Z'') and real (Z') components of the impedance are plotted in what is known as Nyquist plot ($-Z''$ versus Z). The shape and position of the resulting plot for a given electrochemical system can be used to construct the EECs that gave rise to that Nyquist plot, which is often a combination of well-known EECs. For instance, combining a resistor and a capacitor in series gives:

$$Z = R - i/\omega C \tag{2.9}$$

The real and imaginary components of the impedance are R and $-1/\omega C$, respectively. Plotting the Nyquist plot therefore gives a vertical line with an x-intercept of R, corresponding to a constant real value and an imaginary value that

varies inversely with frequency. Combining a resistor and capacitor in parallel, however, gives the following impedance:

$$Z_{RC} = \frac{R}{1 + i\omega CR} = \frac{R(1 - i\omega CR)}{1 + (\omega CR)^2} \tag{2.10}$$

This equation, despite appearing complicated, is the equation of a circle with radius R/2 and a center shifted from the origin by R/2:

$$(\frac{R}{2})^2 = (Z' - \frac{R}{2})^2 + (Z'')^2 \tag{2.11}$$

Since the value of frequency can only be positive, RC combined in parallel gives a semi-circle in the Nyquist plot.

For an electrolyte sandwiched between two blocking electrodes where no charge transfer occurs, maintaining some voltage across the two electrodes results in the ions accumulating at the two electrodes and creating two double layers in series, which can be expressed as the combined double-layer capacitor (C_{dl}). The electrolyte also experiences a geometric double layer capacitance between the two opposing electrodes (C_g) along with the bulk solution resistance (R_b). Thus, an electrolyte between two blocking electrodes would have the following EECs:

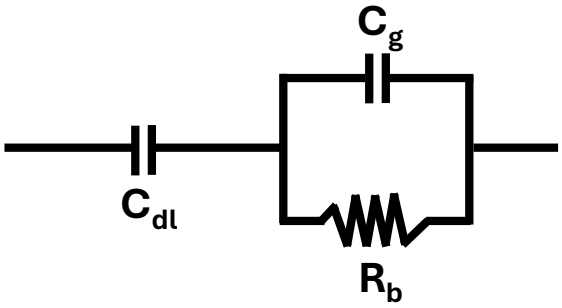


Figure 2.1: The electrical equivalent circuit for an electrolyte between two blocking electrodes.

Combining the previous parallel RC element with a capacitor and solving for

the impedance:

$$Z = -\frac{i}{\omega C_{dl}} + \frac{R(1 - i\omega C_g R)}{1 + (\omega C_g R)^2} \tag{2.12}$$

Where

$$Z' = \frac{R}{1 + (\omega C_g R)^2}$$

$$Z'' = \frac{\left[1 + (\omega C_g R)^2 \left(1 + \frac{C_{dl}}{C_g}\right)\right]}{\omega C_{dl} \left[1 + (\omega C_g R)^2\right]}$$

The obtained Nyquist plot is the typical tailed semi-circle, combining the RC semi-circle and the capacitor spike, with the ratio between C_{dl} and C_g determining how 'damped' the curve is:

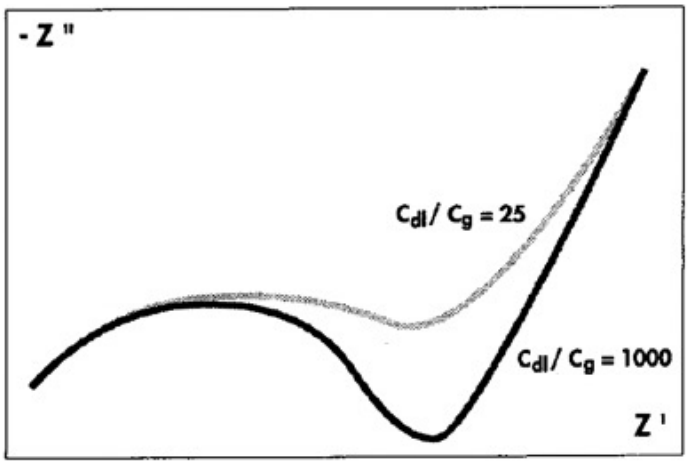


Figure 2.2: The Nyquist plot for an electrolyte between two blocking electrodes. Adapted from [123].

Where the second x-intercept in the real axis, Z', of the semi-circle ($\omega \rightarrow 0$) describes the bulk resistance, R_b, which is critical in determining the ionic conductivity of the electrolyte.

In case of non-blocking electrodes, such as real electrochemical cells, the double layer capacitance is coupled to a charge transfer resistance in parallel,

producing two semi-circles, where the higher frequency semi-circle corresponds to the bulk solution RC whereas the low-frequency corresponds to the interphase. The semi-circles and spikes observed in real electrochemical cells are often damped and tilted, suggesting a deviation from the idealized semi-circular and vertical EEC. This non-ideal behavior is accounted for using constant phase elements (CPE), which can be thought of as an RC element with an imperfect, leaky capacitor:

$$Z_{\text{CPE}} = k(j\omega)^{-p} = \frac{k}{\omega^p}\left[\cos\left(\frac{p\pi}{2}\right) - j\sin\left(\frac{p\pi}{2}\right)\right] \tag{2.13}$$

Where k is a constant and $0 \leq p \leq 1$. When $p = 0$ a CPE acts like a resistor with $R = k$. When $p = 1$ it acts like a capacitor with C = 1/k, and when $p = 1/2$ it acts like a Warburg element which approximates diffusion.

2.1.2 Cyclic Voltammetry

Cyclic Voltammetry (CV), along with Linear Sweep Voltammetry (LSV), is indispensable in understanding redox reactions of both molecular and ionic species in an electrolyte, where the voltage is varied linearly from a starting potential, E_1, to a switching potential, E_2, at a scan rate, ν [mV/s], while measuring the current response, i, typically across a 3-electrode cell. Consequently, the species in the electrolyte undergo oxidation/reduction depending on the applied voltage, E, meanwhile changing in concentrations according to the Nernst equation:

$$E = E^0 + \frac{RT}{nF}\ln\left(\frac{[Ox]}{[Red]}\right) = E^0 + 2.3026\frac{RT}{nF}\log_{10}\left(\frac{[Ox]}{[Red]}\right)$$

Where E^0 is the potential for the Ox/Red pair at standard conditions, (Ox) and (Red) are the activities of the two species, F is Faraday's constant, n is the number of electrons. Due to diffusion of the species from and to the electrode, a differential concentration between the interface and bulk solution occurs, resulting in a 'delay' or mismatch between cathodic and anodic current peaks,

i_{pc} and i_{pa}, even when the process is electrochemically reversible, which gives rise to the typical duck-shape $i - E$ plot (Figure 2.3). This distance between the electrode surface and the bulk solution is often called the diffusion layer. Furthermore, in less reversible processes (non-Nernstian) the electron transfer is sluggish, this results in polarization at the interface and is reflected in wider peak separation, ΔE_p.

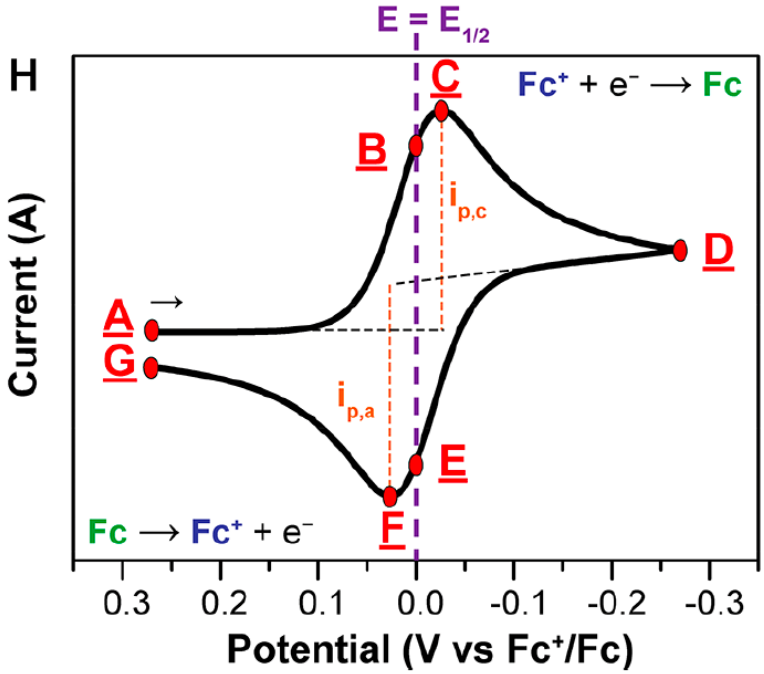


Figure 2.3: The typical duck-shape curve in a cyclic voltammetry, showing the anodic, i_{pc}, and cathodic, i_{pa}, peak currents. Note that this follows the US convention of a negative oxidation current and a reversed potential axis. Adapted from [124].

In a CV experiment, the scan rate can influence both the position and intensity of the current peak, based on the Randles-Sevcik equation:

$$i_p = 0.446nFAC^0 \left(\frac{nFvD_o}{RT}\right)^{1/2}$$

Where C^0 is the concentration of the oxidized/reduced species, A is the electrode surface area, and D_o is the diffusion coefficient of the analyte. As the scan rate is increased, the diffusion layer gets smaller, resulting in larger currents. A deviation of the observed current from that calculated by the Randles-Sevcik

equation can be used to determine whether a reactant is diffusing freely in solution as opposed to being deposited or absorbed on the electrode.

A CV measurement is often performed using a 3-electrode cell, composed of a working electrode (WE), a counter electrode (CE), and a reference electrode (RE). While the current runs between the first two, the latter is used to report the voltage against a stable, well known electrochemical reaction. Common materials used as working electrodes include platinum, carbon, and mercury. Furthermore, when performing a CV, a supporting electrolyte is often used to lower the solution resistance and to provide ions whose migration can compensate for the electron charge transfer between the analyte and the electrode. Common salts, with wide ESW that enable the study of the analyte without degradation, include an ammonium cation, often $^{+}NBu_4$, with an anion such as BF_4^-, ClO_4^-, PF_6^-, or $B(C_6H_5)_4^-$.[124]

2.1.3 Galvanostatic Cycling

Galvanostatic, or chronopotentiometric, cycling involves applying a constant current and measuring the potential across the working and counter/reference electrodes up to a preset voltage cutoff. Alternating the current between a positive and a negative value for multiple cycles resembles the charging/discharging, which allows the study of the cycle life and capacity fading of the cell, often denoted as the coulombic efficiency (CE) to describe the efficiency in retaining the charge capacity, Q, between charge and discharge:

$$CE = \frac{Q_{discharging}}{Q_{charging}} \tag{2.14}$$

Where the observed $Q_{discharging}$ and $Q_{charging}$, in mAh/g, is obtained from the applied current needed to reach the cutoff voltage, normalized by the mass of the working electrode. This current/voltage profile can be used to obtain a plethora of information about the cell performance, such as differentiating the capacity over the potential dQ/dV to see at what voltages an electrochemical reaction

occurs. Furthermore, the value of the applied current can be varied to study the rate capability during (dis)charging. This is often expressed in units of time as C-rate, where C/10 indicates a current that would discharge the theoretical capacity in 10 hours.

2.1.4 Electrodes and Coin Cell Fabrication

Due to the electrically insulating nature of most active materials, electrodes often are made into composites to contain a conductive carbon additive (10-30%) and a polymeric binder (1-10%). In this work, two ways for electrode fabrication were used: dry mixing, where the active material (e.g., PbF_2) was pre-mixed with carbon fiber, followed by adding PTFE binder and mixing using pestle and mortar to form a dough which was then rolled into 50-100 μm electrodes, and wet-casting, where the active material, carbon super-p, and polyisobutylene (PIB) dissolved in O-dichlorobenzene were mixed and casted on carbon-coated aluminum foil using doctor blade, followed by drying under vacuum to remove residual solvent. In all these assemblies, the active material was first ball milled for 12 h to obtain 0.1 μm size particles. The electrodes then would be assembled into a coin-cell (Figure 2.4, where the electrolyte is added dropwise to a total volume of 150 μL before the coin-cell is sealed using a crimping machine.

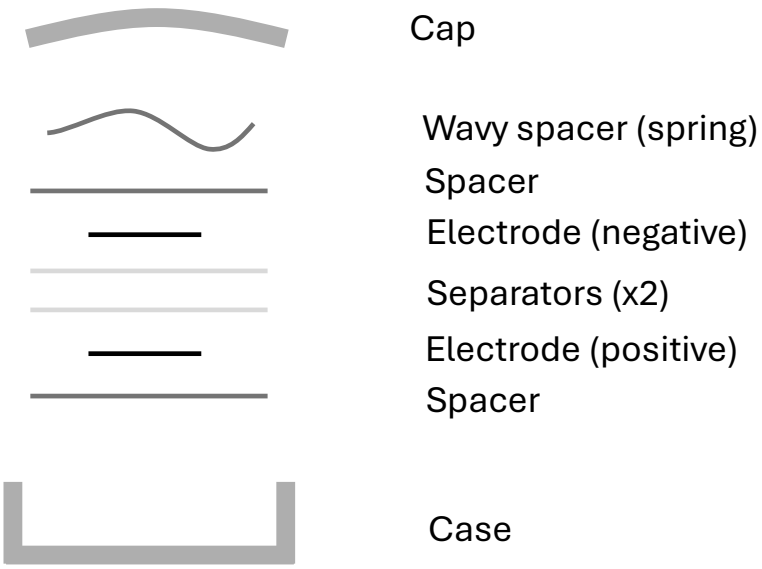


Figure 2.4: The sequence of components used in coin-cell assembly.

2.2 Solvation Structure

2.2.1 Total Neutron Scattering

Every moving particle, including neutrons, has wave-like properties with a de Broglie wavelength:

$$\lambda = \frac{h}{m\nu}$$

In XRD, waves scatter off of valence electrons, while in neutrons they scatter off of atomic nuclei, which results in the high sensitivity of neutron scattering towards low atomic weight atoms such as hydrogen and deuterium which are typically invisible in XRD. The momentum transfer between incident and scattered neutrons can be described in terms of Q, the scattering vector:

$$Q = \frac{4\pi sin(\theta)}{\lambda}$$

Where θ is the scattering angle and λ is the wavelength, indicating that larger Q values correspond to smaller wavelengths and thus smaller probed distances.

Therefore, due to the wide range of Q accessible by neutrons, fine spatial resolution can be achieved. The scattering intensity can be described in terms of the structure factor, $F(Q)$:

$$F(Q) = \sum_{\alpha,\beta \geq \alpha} (2 - \delta_{\alpha\beta}) c_\alpha c_\beta b_\alpha b_\beta (S_{\alpha\beta}(Q) - 1)$$

Where δ is Kronecker delta, c and b are the concentration and scattering length weighting factors, respectively, and $S(Q)$ is the static structure factor summed over all α, β atom pairs to capture the fingerprint of the entire arrangement of atoms. From this, the total radial distribution function, $G(r)$, describing the probability density of finding atom α a distance r from atom β, can be calculated:

$$G(r) = \frac{1}{(2\pi)^3 \rho_0} \int_0^\infty 4\pi Q^2 F(Q) \frac{sin(Qr)}{Qr} dQ.$$

Structural information can then be extracted from the total neutron scattering using the Empirical Potential Structure Refinement (EPSR) method, where a Monte-Carlo simulation consisting of a Lennard-Jones potential plus a coulombic term is used to fit the neutron scattering:

$$U_{inter} = U_{\alpha\beta}(r_{ij}) = 4\epsilon_{\alpha\beta} \left[\left(\frac{\sigma_{\alpha\beta}}{r_{ij}} \right)^{12} - \left(\frac{\sigma_{\alpha\beta}}{r_{ij}} \right)^{6} \right] + \frac{q_\alpha q_\beta}{4\pi\epsilon_0 r_{ij}}$$

Where the well depth parameter, $\epsilon_{\alpha\beta}$, and the range parameter $\sigma_{\alpha\beta}$ are equal to, respectively, $\sqrt{\epsilon_\alpha \epsilon_\beta}$ and $\frac{1}{2}(\sigma_\alpha + \sigma_\beta)$. After the simulation reaches equilibrium, the Empirical Potential is started, and the Monte Carlo process iteratively adjusts the structure to match the experimental neutron scattering data. This is achieved by adding a small empirical potential term into the reference potential, refining the model until optimal agreement is obtained. As a result, the structural information remains consistent with the neutron total scattering profiles of the samples.

In this work, Neutron total scattering data were acquired on the Near and Inter-Mediate Order Diffractometer (NIMROD) at ISIS, the UK Neutron and Muon

Source, in a Q range $0.02 < Q < 50$ Å^{-1}.

2.2.2 Molecular Dynamics (MD) simulations

In molecular dynamics (MD), each particle describing a molecule or ion in the electrolyte is subjected to a force derived from an interatomic potential. This gives an equation of motion that describes the energy as function of position, which if integrated over discrete time steps gives a time-resolved trajectory that captures the equilibrium positions and solvation interactions.

In this work, on-the-fly machine-learned forcefields (MLFF) as used in VASP6 were used.[125] For ab-initio calculations, a semilocal RPBE exchange-correlation functional with D3 dispersion corrections was used.[126, 127] Initial geometries were generated with PACKMOL.[128]

2.2.3 Density Functional Theory (DFT)

Density functional theory (DFT) is a quantum mechanical computational method used to investigate the electronics and energetics of materials and is based on a reduced, one-dimensional form of the Schrodinger equation that uses the electronic density, $\rho(r)$, instead of the many-body wavefunction to describe the energy of the particles, where it was found that a model for non-interacting electrons based on the Kohn-Sham (KS) equation can reproduce the ground-state energy for real interacting systems:

$$\left[-\frac{\hbar^2}{2m}\nabla^2 + V_{\text{ext}}(\mathbf{r}) + V_{\text{H}}(\mathbf{r}) + V_{\text{XC}}(\mathbf{r})\right]\psi_i(\mathbf{r}) = \epsilon_i\psi_i(\mathbf{r})$$

Where V_{ext}, V_{H}, and V_{XC} are, respectively, the external potential (e.g., from nucleus), the Hartee potential for electron-electron repulsion, and the exchange-correlation potential accounting for many-body interactions and is the potential modified during a DFT calculation. By solving the KS equation, one can obtain the electron density needed for the DFT computation:

$$\rho(\mathbf{r}) = \sum_i |\psi_i(\mathbf{r})|^2.$$

In this work, DFT calculations were carried out with Gaussian16 using B3LYP functional with basis set 6-311G++-(p,d) in vacuum. The diffuse basis set (++) was used to take into account the effect of polarization induced by the presence of the positive charge on imidazolium. Charges were added or removed from the atoms to create the corresponding fragments to simulate MMIm and the deprotonated MMIm (the carbene), respectively. A first geometric optimization calculation was run with a tight energy convergence criteria of 10^{-12} Ry followed by ground-state calculation to compute the two corresponding ground-state energies.

2.3 Chemical Analysis

2.3.1 Nuclear Magnetic Resonance (NMR)

Nuclei generate magnetic fields because they are charged and are continuously spinning. As spinning magnets, they possess a magnetic moment, μ, described in units of magneton (1 magneton = $5.05078 \cdot 10^{-27}$J T^{-1}). They also have a characteristic spin, I, that can have values of zero, integers, or fractions. 1H, 13C, 19F all have spins of 1/2 due to their odd number of nucleons (protons and neutrons). As an external magnetic field is applied, some nuclei align with (α state, lower energy) and others align against (β state, higher energy) the external magnetic field. The difference in energy between these two states can be expressed as:

$$\Delta E = \frac{\mu B_x}{I}$$

Where B_x is the external magnetic field, I is the spin, and μ is the magnetic moment. The energy difference, and hence the detection limit of the signal, is

proportional to the strength of the external magnetic field but also to the magnetic moment of the nucleus. Given that energy is proportional to frequency through Plank's constant, this energy difference is often more conveniently expressed as frequency, ν, with frequencies usually ranging from 20 to 900 MHz, which is around the frequency of radio waves, hence the mild and nondestructive nature of NMR. In the NMR spectrometer, the sample is subjected to both a strong magnetic field to initiate the nuclei alignment and to an electromagnetic wave in the radio frequency range (e.g. 100 MHz). The radio frequency EM is absorbed by the sample as it undergoes the $\alpha \rightarrow \beta$ transition, and a detector then records the change in the frequency absorbed by the sample due to the magnetic transition.

NMR is powerful because nuclei in different environments behave differently as the surrounding electrons produce magnetic fields that either oppose or enhance that of the applied field (shielding), thus resonating at different frequencies. This can be used to probe and compare the different electronic environments and infer the chemical structure and molecular interactions. When the surrounding electrons oppose the applied field (more shielded), as in the case of electron donating groups, the nucleus resonates at lower frequencies, also known as up or high field.

The NMR spectrometer works by sweeping a range of magnetic fields and detecting the change (i.e. absorption) in radio frequency waves. The swept range of the magnetic field (i.e., the frequency of its energy) is expressed as ppm, that is a fraction of the total magnetic field applied. For instance, if a 2.34 T magnetic field with a sweep from 2.3487 to 2.3488 T was applied, then this would correspond to 0.0001/2.34 = 42.7 ppm. The response of the observed nucleus is then reported within this ppm range. For protons, this usually occurs within 12 ppm. This method is used to standardize the frequency reading for any given sample across various magnetic field strengths, as the absolute value of the transition energy (or frequency) is dependent on the strength of the external

magnetic field and the frequency of the applied radio wave. Reporting the transitions in ppm relative to an internal standard ppm eliminates this inconsistency. This ppm value is known as the chemical shift, δ:

$$\delta = \frac{\nu_{\text{sample}} - \nu_{\text{ref}}}{\nu_{\text{ref}}}$$

The proton chemical shift is the most widely used due to the abundance of the 1H isotope and their prevalence in organic molecules. Protons in alkyl groups, CH, often have sharp NMR signals corresponding to a set chemical shifts. The range for OH and NH is often wider due variations in the hydrogen bonding at different solvent conditions and concentrations, where stronger hydrogen bonding shifts the signal downfield (hydrogen bonding deshields the proton, resulting in larger frequency). Dilute solutions have weaker hydrogen bonding and are therefore more upfield. The hydroxy protons in carboxylic acids are very downfield (e.g., 11 ppm) because of the intramolecular cyclohexane dimeric structure that enhances the hydrogen bonding. Also, OH protons exchange with deuterium very rapidly. This can be used to remove or determine the OH proton signal. This also results in OH protons in the same different molecules in one sample exchanging very rapidly and thus showing a single average signal. If a single molecule contains both an alcohol proton (~2 ppm) and a carboxylic acid proton (~14 ppm) for instance, it will show one broad peak at around 6 ppm.

Besides the chemical shift, more information can also be obtained from the peak splitting, which is a result of spin-coupling of nearby nuclei. A pair of spin-coupled nuclei have the same value of coupling constant, J, with values of J ranging from 1 to around 20 Hz and is magnetic field independent. If the coupled nuclei have significantly different chemical shifts ($\nu >> J$), then first order splitting is obtained with the usual doublet, triplet, or quartet splittings, depending on how many nuclei are causing the splitting. If the chemical shift is too close, the splitting pattern will be distorted (2nd order splitting) where the signal close to the to the chemical shift of the coupled nucleus has slightly higher intensity. Spin-coupling occurs for both geminal ^{2}J (two nuclei bonded to the

same center) or vicinal ^{3}J (bonded to neighboring centers) nuclei, where the superscript denotes the number of bonds between the two nuclei. Longer range coupling is also observed for rigid frameworks. If a nucleus is coupled to multiple (e.g., two) different nuclei, then its signal is split twice with a distinctive coupling constant for each splitting. Spin coupling occurs with both identical and different elements (e.g. F and H), and can be used to infer the neighboring atoms in an NMR spectra.

2.3.2 Pulse-field Gradient (PFG) NMR

The magnetic moment of a nucleus precess, that is it rotates with an angle to form a cone shape in the presence of an external field. This precession is most visible when the magnetic dipole moment is perpendicular to that of the external field, similar to how a spinning object with an angular momentum precesses in the presence of a gravitation field. The angular frequency of this precession is called the Larmor frequency, ω_0:

$$\omega_0 = \gamma B_0$$

Where γ is the gyromagnetic ratio characteristic for every nucleus and is an indicator of how sensitive the nucleus is towards NMR, where 1H is the highest. The way the nucleus is tipped, favorably to 90-degrees to give the stronger precession and thus the strongest signal, is using a coil that transmits an oscillating magnetic field with a frequency equal to the Larmor frequency, just like when you tip a gyroscope your finger need to be rotating with the same frequency as the wheel. This same coil is used to detect the EM signal (as voltage) coming from the nucleus as it decays back during the free induction decay (FID). The FID is in the time domain and is Fourier transformed to the frequency domain to show a peak, where the faster the decay the broader and shorter the peak is and the lower the signal-to-noise ratio. The external field has to be homogeneous. If it's not, different nuclei will have different alignments, and thus different Larmor

frequencies, and they will cancel each other and decay faster, resulting in a more noisy signal. Still, some residual inhomogeneity, along with thermal relaxation causing the magnetic field to align with the external field, is what eventually causes the decay. If a 180-degree pulse is applied, the faster nuclei go back and the slower goes to the front so they all come back in step with each other some time later resulting in a higher signal as the nuclei come in phase, before they finally decay (dephase) in a duration called the second relaxation time (T2). T1, on the other hand, describes the longer relaxation time (T1>T2) needed to realign with the external field B_0.

Applying a specific sequence of pulses turned out to be extremely valuable in studying the diffusion of nuclei using pulse field gradient (PFG) NMR. There are two major PFG pulse techniques: spin-echo (SE) and stimulated echo (STE). In both methods, and designating the spin as a vector aligned in the z-axis, the nuclei are first hit with a 90-degree ($\pi/2$) radio frequency (RF) pulse to excite the spin to the xy plane where they then relax in a time that is the second relaxation time (T2). Next, a gradient pulse with an intensity of g and a duration of δ is applied (forming a helical magnetic moment, where the spacial position is encoded in the phase shift that formed the helix). The molecules then diffuse for a time of Δ, followed by another gradient pulse and finally FID acquisition (Figure 2.5). The SE and STE differ in that in SE the magnetization is transversal during diffusion while it is longitudinal in STE. Also, STE relaxes through T1 while SE through T2.

By tuning g, δ, and Δ and measuring the intensity, the diffusion coefficient can be determined from the linear fit of the Stejskal-Tanner equation:

$$\ln\left(\frac{A(2\tau)}{A(0)}\right) = -D\gamma^2 g^2 \delta^2 \left(\Delta - \frac{\delta}{3}\right) \tag{2.15}$$

In this work, diffusion coefficients were measured at 30 °C using pulsed field gradient (PFG) NMR, with measurements completed at 9.45 T (ν_0(1H) = 400.19 MHz, ν_0(^{19}F) = 376.51, and ν_0(^{133}Cs) = 52.49 MHz) on Bruker Avance III HD spectrometer using a 5 mm single-axis diffusion probe with exchangeable ceramic

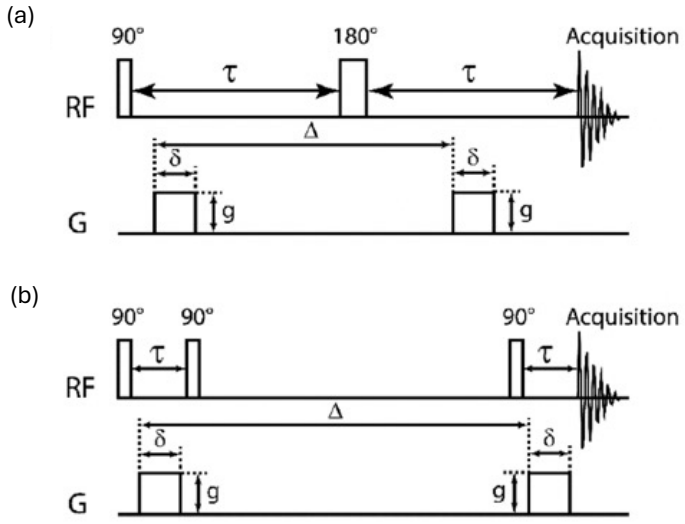


Figure 2.5: The two main PFG NMR sequences (A) spin-echo. (B) stimulated-echo. Adapted from [129].

heads. A stimulated echo pulse sequence was utilized for all PFG experiments with effective gradient pulse durations (δ) ranging between 1 to 1.5 ms, and a diffusion time (Δ) of 10-30 ms, with the gradient amplitude varying between 0.1 and 24 T/m in 36 steps. ^{17}O NMR spectra was obtained using direct observation of natural abundance ^{17}O at 11.75 T ($\nu_0(^{17}\text{O})$ = 67.77 MHz) on Bruker Avance III spectrometer equipped with a 5 mm smart probe. All spectra were referenced to $H_2{}^{17}O$ (δ_{iso} = 0 ppm), with a relaxation time of 200 ms, and 1024 transients collected per experiment. All samples were sealed in a J-Young air-tight NMR tube, temperature stabilized to 303.1 K, and a 1-second recycle delay was used throughout. All data was fitted to the Stejskal-Tanner equation with an R^2 value of 0.999, errors of < 1% and normal distribution of the residuals (>0.5 Shapiro Wilko score) were observed for all experiments.

2.3.3 ICP-MS

Inductively Coupled Plasma Mass Spectrometry (ICP-MS) detects traces elements in a sample. First, the sample is nebulized into aerosols using high-speed argon stream, where the ICP torch then hits the sample with high-temperature

argon plasma that atomizes the sample into single charged species (M^+) that travel to a quadrupole consisting of four electrodes with oscillating electric field to filter species based on their charge-to-mass (m/z) ratio, where the ion counts measured by the detector is directly proportional to the concentration of the element, which is often calibrated using a standard of known concentration to reach detection limits down to ppt level. In this work, to calculate the concentration of a fluoride salt in a solvent, an oversaturated CsF solution in the corresponding solvent was stirred at ambient temperature (recorded 23 °C) overnight and then filtered using a syringe filter. The filtrate was diluted and digested in diluted (2%) nitric acid solution, and the Cs content was measured using ICP-MS and the absolute concentration determined using a Cs standard calibration curve.

2.3.4 Differential Scanning Calorimetry (DSC)

Differential Scanning Calorimetry (DSC) measures the heat flow to and from a sample as it undergoes a phase change or chemical reaction, thus providing a profile of thermal stability at various temperatures. A few milligrams of the sample in a sealed aluminum pan is subjected to a controlled heating/cooling rate (typically 5 - 30 °C/min) and the DSC sensor contrasts the heat flow against a reference empty pan, where endothermic transitions (e.g., melting, glass transition) and exothermic transitions (e.g., freezing, crystallization) are characterized by absorbing and releasing heat, respectively. In this work, DSC was used to study the liquidus range of ionic liquid and solvent-in-salt electrolytes, characterized by the temperature range between the solidification and melting phase transitions.

2.4 Solid-state Structure Characterization

2.4.1 (In-situ) Transmission Electron Microscopy (TEM)

Transmission electron microscopy (TEM) is a widely used and powerful imaging technique used to investigate structure and composition of materials. Since electrons have smaller wavelength (down to a few picometers) compared to both visible light and X-rays, nanometer and atomic resolution can be achieved:

$$\delta = \frac{0.61\lambda}{\mu sin(\beta)}$$

Where δ is the resolution, λ is the wavelength, μ is the refractive index, and β is the semi-angle of collection. In TEM, an electron gun sends a beam of electrons through an accelerating voltage of 80 - 300 keV, before reaching an ultrathinned sample. Along the beam path, an electron beam control system consisting of two condenser lenses sandwiching the condenser aperture are used to focus the beam, enabling resolutions down to 1 nm. The transmitted electrons are then magnified and projected by the objective and projector lenses onto the CCD camera to form the image.

The wealth of information obtained from TEM comes from the wide range of signals generated from the sample upon the passage of the electron beam. Transmitted electrons, consisting of elastically and inelastically scattered electrons, are used to construct bright-field (BF) images where higher atomic number regions show darker contrast due to the transmission of few electrons. Scattered electrons (e.g., backscattered, Auger, and secondary electrons) collected by the objective aperture are used to construct dark-field (DF) images.

In this work, a hexane suspension of the investigated sample (e.g. copper nanocubes) was drop-casted on carbon-coated TEM grid and dried for 4-6 h under vacuum. TEM images were taken using JEOL 2100 and 3000F emission

gun and a Gatan Ultrascan CCD Camera. In-situ TEM was performed by connecting a Nanofactory Instruments Dual-Probe STM-TEM In-situ holder with a controllable tip and a portable Biologic VMP3 potentiostat.

2.4.2 X-ray Photoelectron Spectroscopy (XPS)

In XPS, the sample is struck by X-rays of increasing energy, and the kinetic energy of the ejected electrons is measured, allowing the determination of the binding energy of the electrons using the photoelectric effect. The plot is often given as counts (i.e. of electrons) at a given binding energy (in eV), and each peak can be assigned to a specific orbital (e.g. 2s, 3s..) for a given element. The number of counts for each peak is proportional to how much of that element is present. Reproducible shifts in the binding energy can be used to determine the bonding environment of the atom. These are called chemical shifts (similar to NMR) and they are due to changes in the oxidation states.

In this work, the sample was grounded to the XPS stage using carbon tape and transferred from Ar glovebox to the PHI VersaProbe III XPS using a MOD 07-111K, ULVAC-PHI, Inc. vacuum transfer. An Al Kα (hv = 1486.8 eV) X-ray source was used, while maintaining a vacuum below 10^{-6} Pa throughout this experiment.

3

Solvent-in-salt Protic Electrolytes[1]

Contents

3.1 The Case for Concentrated Electrolytes 60

3.2 Fluoride Solubilities in Protic Solvents 61

3.3 Electrochemical Stability Window and Thermal Stability . . 64

3.4 Diffusivity and Ionic Conductivity 67

3.5 Chemical Stability Towards HF Formation 70

3.6 Galvanostatic and Potentiometric Cycling 74

3.7 Dilution and Potential Co-solvents 76

[1]Parts of this chapter have been published in *ACS Energy Letters* 8.6 (2023): 2668–2673.[130]

3.1 The Case for Concentrated Electrolytes

Concentrations of ca. 1 M are typically used in liquid battery electrolytes. In the Li-ion context, this typically consisted of a lithium salt (e.g., $LiPF_6$) dissolved in a mixture of ethylene carbonate (EC) and a linear carbonate. Despite their optimized ionic conductivity, these conventional electrolytes suffered from sub-optimal ESW, high volatility and low thermal stability.[131] A few solutions emerged to tackle these challenges, including polymer electrolytes, ionic liquids, solid electrolytes, and salt-concentrated electrolytes, the latter of which has attracted an increased interest.

Increasing the charge carrier concentration can introduce unusual changes both to the solvation structure and the physicochemical properties compared to the conventional diluted electrolyte, all driven by the disappearance of free solvent molecules at sufficiently high concentrations.[132] For instance, high-capacity lithium-sulfur batteries with improved cycling stability could be achieved in concentrated electrolytes due to the suppression of polysulfides dissolution at the sulfur cathode.[133, 134] Additionally, solvent molecules that are bound to a charge carrier, C^+, (e.g. Li^+) will have a lower highest occupied molecular orbital (HOMO) and a higher lowest unoccupied molecular orbital (LUMO) compared to the free solvent, due to the bonding interaction with the charge carrier(Figure 3.1).

Given the electrochemical stability window is proportional to the LUMO-HOMO energy difference, this can result in enhancing the ESW in the concentrated electrolytes. For instance, this enabled the cycling of ether solvents in 4-V class Li-ion batteries, which was previously unattainable due to the low oxidation stability for ethers.[135] At sufficiently high concentration, the solvent ceases to be the dominant component in the electrolyte, giving rise to solvent-in-salt (SIS) electrolytes, where the amount of salt exceeds that of the solvent both in weight and volume fractions.[136]

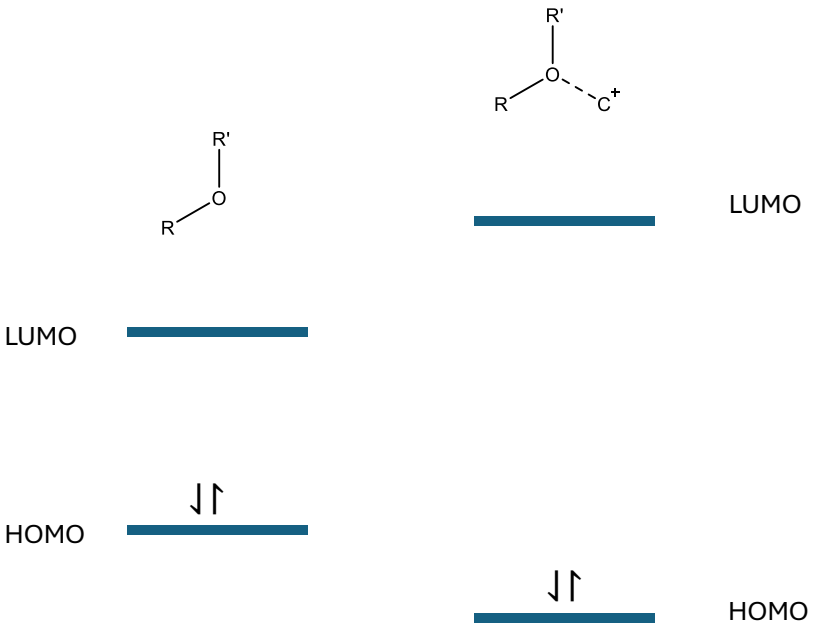


Figure 3.1: Schematic of the change in energy levels of the HOMO and LUMO molecular orbitals at increased concentration and stronger ion-solvent bonding.

While there have been tens of reports for concentrated Li-ion electrolytes, concentrated fluoride-ion electrolytes were hardly explored, partly because the fluoride has low solubility in aprotic solvents which has been the focus of most previous work on FIB electrolytes. Still, the fluoride-ion is soluble in protic solvents due to its ability to form strong hydrogen bonds. Thus, exploring concentrated fluoride electrolytes in protic solvents was an untapped field that needed investigation. Similar to lithium, the fluoride solution is expected to go from solvent-separated ion pairs (SSIPs) and an electrolyte-electrode interface dominated by the free solvent molecules, to contact-ion pairs (CIPs) and ion aggregates (AGGs) as the fluoride concentration is increased up to the SIS threshold, resulting in an ion-dominated electrode-electrolyte interface (Figure 3.2).

3.2 Fluoride Solubilities in Protic Solvents

Among the fluoride salts, cesium fluoride is the only salt that can strike a balance between low cost, availability, and high solubility in protic solvents, compared to

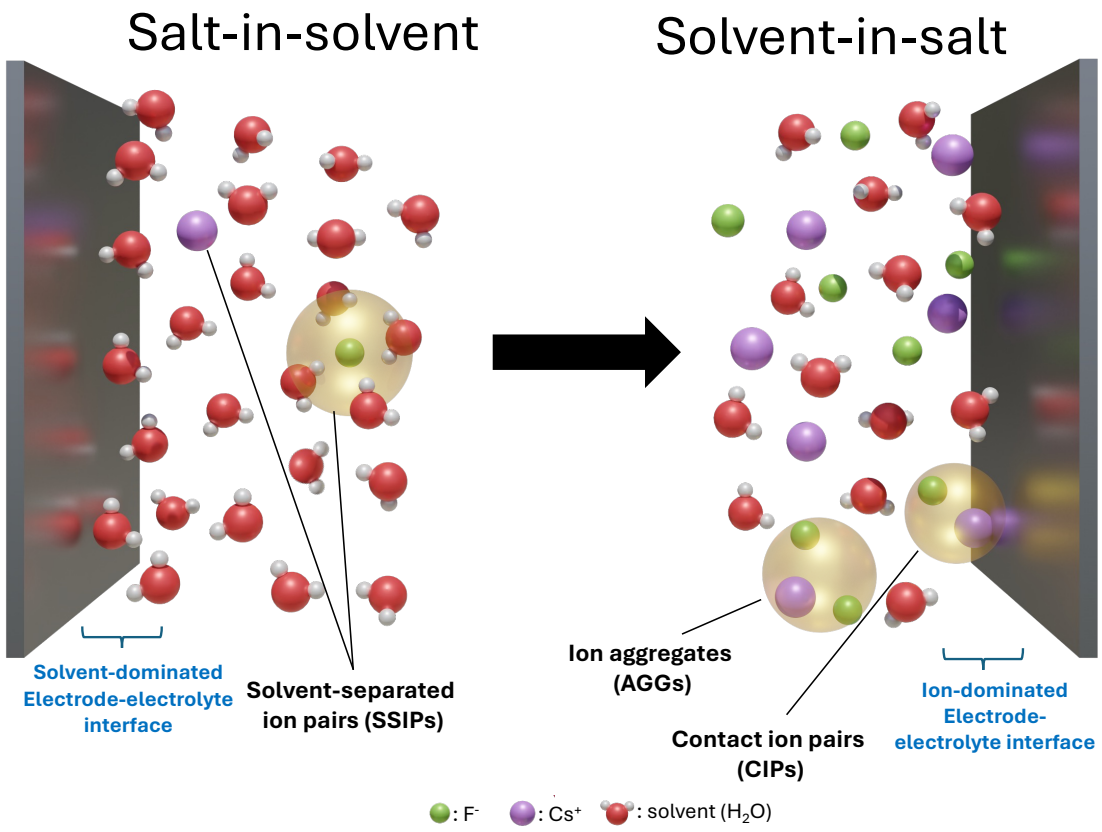


Figure 3.2: Representation of the evolution of the ionic species in the bulk and the electrode-electrolyte interface as the concentration is increased from salt-in-solvent to solvent-in-salt electrolytes.

other inorganic salts (e.g., LiF, NaF, KF) which have insufficient solubilities, and organic fluorides (e.g., TMAF) which are costly to obtain in the large quantities needed for highly concentrated electrolytes.

The solubility of CsF in a range of protic solvents, including alcohols, amides, and water, was measured at room temperature using inductively coupled plasma-mass spectrometry (ICP-MS) to gauge the concentration of the counter cation and thus the fluoride. CsF was found to have the highest solubility in water, at a concentration limit of 37 m, compared to a solubility of less than 10 m in methanol and formamide, and less than 5 m in ethanol and isopropanol (Figure 3.3). This is reasonably expected due to the higher dielectric constant for water compared to methanol, and the presence of two O-H bonds in water capable of accepting a hydrogen bond from the fluoride ion, compared to only one in methanol.

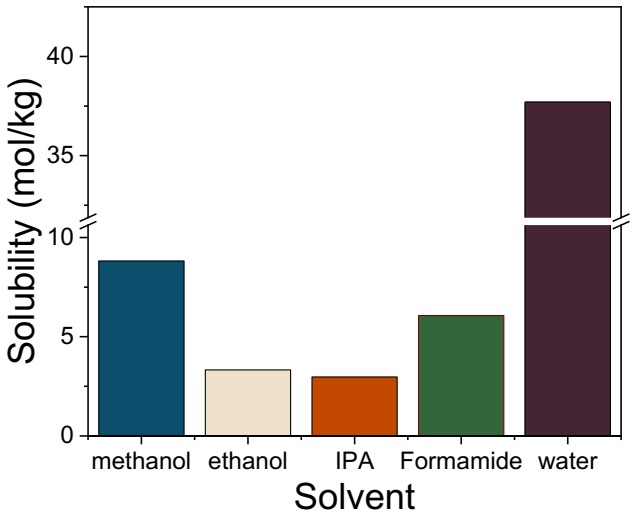


Figure 3.3: Solubility of CsF determined using ICP-MS in common protic solvents (methanol, ethanol, isopropanol, formamide, and water).

The volume, weight, and molar ratios were then calculated up to the measured solubility limit for each solvent (Figure 3.4). These ratios can shed light on whether the given solvent satisfies the solvent-in-salt condition, that is a salt-to-solvent weight and volume ratio equal to or exceeding unity.[136] The weight ratio varied for each solvent based on the different densities, but the volume ratio was the same since it only depended on the amount of salt used at a given molal concentration, and it reached a value of one at a concentration of around 25 m. Water was the only solvent that could satisfy this condition, compared to other solvents that would only exceed a weight or volume ratio of unity beyond their solubility limit, meaning that for these solvents it was not possible to prepare a solvent-in-salt electrolyte at room temperature. Furthermore, other salts such as KF could not have a volume ratio larger than one because of its lower solubility, despite some reports still referring to them as solvent-in-salt electrolytes.[137]

Looking at the solvent-to-salt molar ratios at each concentration (Figure 3.5) shows that there were less than two water molecules solvating each CsF unit in the solvent-in-salt concentration region of 25 m and beyond. This means that the obtained mixture is a ”hydrate-melt” that is still a clear, flowing liquid

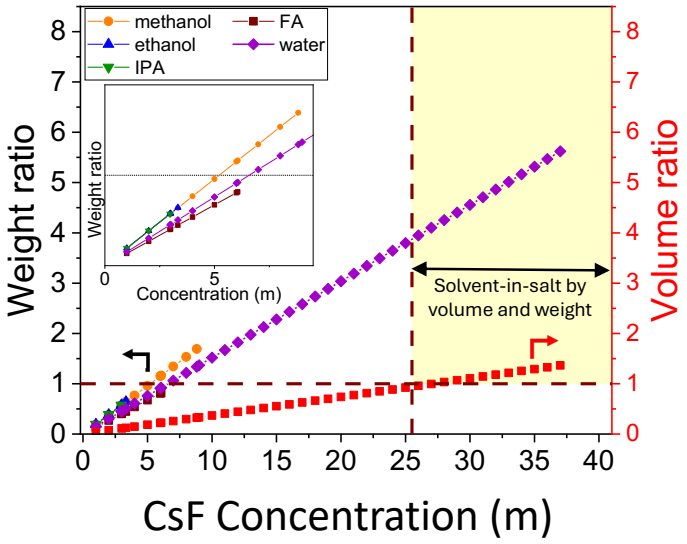


Figure 3.4: Salt-to-solvent weight and volume ratios showing the concentration range of 'solvent-in-salt' region.

at room-temperature despite its high concentration. The choice of water over other alcohol or amide protic solvents was further encouraged by water exhibiting a higher boiling point, lower flammability, and non-toxicity compared to other organic protic solvents, and its ability to overcome the need for ultra-dry battery manufacturing conditions. Thus, water-in-salt electrolytes (WISE) were the most promising out of the explored protic electrolytes.

3.3 Electrochemical Stability Window and Thermal Stability

However, water and protic solvents in general are known to have narrow electrochemical stability windows, limiting the use of high-voltage cathodes and thus the energy density. To explore whether the water-in-salt electrolytes described previously could achieve the main advantage of concentrated electrolytes, that is the expanded electrochemical stability window, LSV was performed. For concentrations greater than 25 m, the ESW for WISE was found to be 3.1 V (Fig-

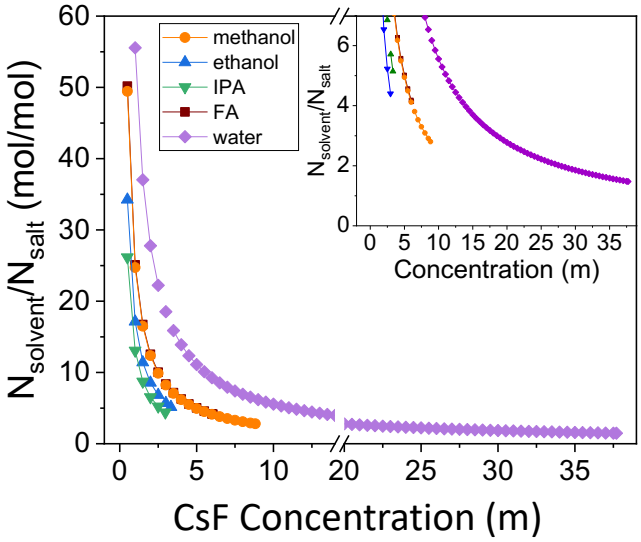


Figure 3.5: Solvent-to-salt molar ratio showing <2 coordination number for CsF in water.

ure 3.6), compared to <2 V for conventional salt-in-solvent aqueous electrolytes and 1.23 V for pure water. This enhancement in the ESW is a result of the increased activity and molar fraction of the salt in the electrolyte both in the bulk and at the electrode, resulting in an ion-dominated electrode-electrolyte interface compared to the less electrochemically stable free water molecules which tends to give rise to solvent-dominated interface in the conventional salt-in-solvent electrolytes. Furthermore, electrolytes that contain significant amounts of free water molecules would have a limited ESW even if deemed concentrated compared to conventional electrolytes, such as the recently reported aqueous KF electrolyte showing an ESW of 2.1 V.[137]

Besides the expanded ESW, water-in-salt electrolytes also show improved thermal stability. Diffraction scanning calorimetry (DSC) curves show a freezing point of around -2.5 °C for the 1 m, which is suppressed to below -20 °C for the highly concentrated electrolyte (Figure 3.7). This colligative decrease in freezing point is due to the increased entropy as more ions are introduced to the solution, breaking the solvent-solvent intermolecular forces. At elevated temperatures, thermal gravimetric analysis (TGA) shows a delayed thermal decomposition, due

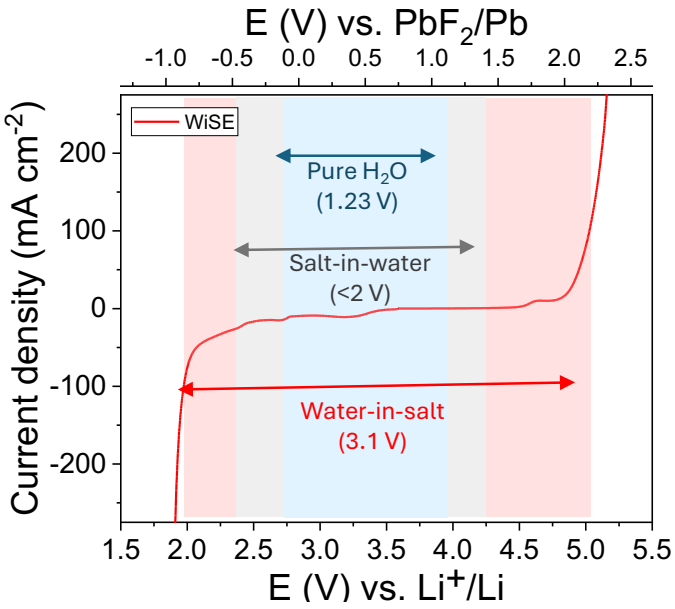


Figure 3.6: Electrochemical stability window (ESW) expansion in the water-in-salt electrolyte (this work) compared to pure water and other aqueous electrolytes.

to both the smaller water fraction and the strong binding with the ions. This indicates that water-in-salt electrolytes have a wider liquid range and are therefore more suitable for both low and high temperature applications compared to conventional aqueous electrolytes.

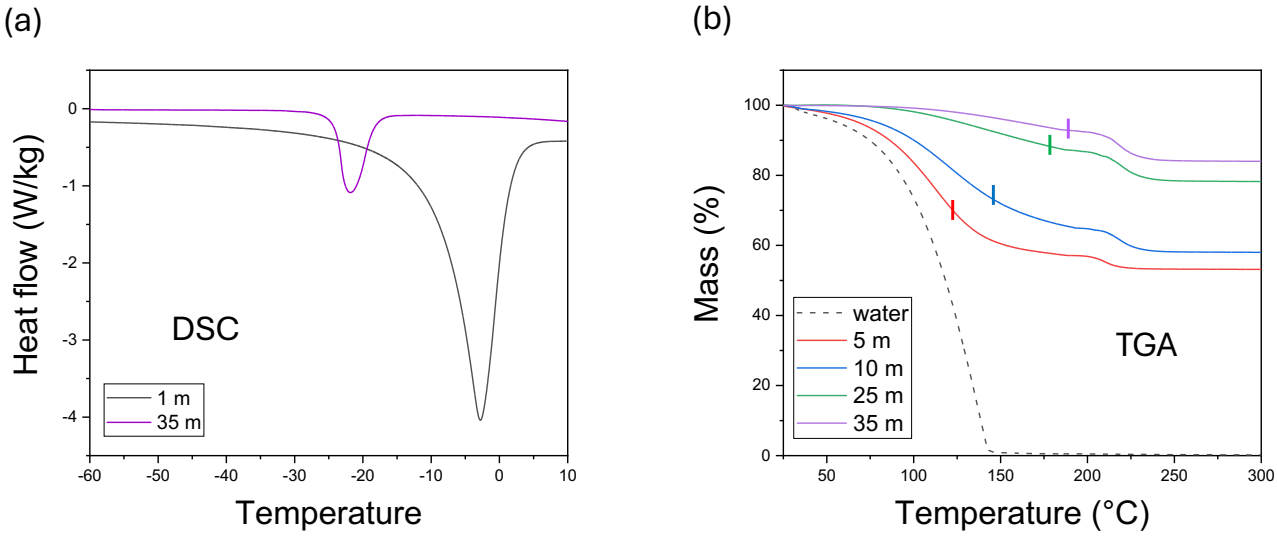


Figure 3.7: DSC scans at sub-zero temperatures (a), and TGA measurement at elevated temperature (b), both showing an extended liquid range due to the suppressed freezing point and increased decomposition temperature.

3.4 Diffusivity and Ionic Conductivity

Despite their expanded electrochemical stability, water-in-salt electrolytes are encumbered by high viscosities, which is undesired for high-performance electrolytes due to potentially limiting transport and kinetic capabilities. The molar conductivity, Λ, which is the ionic conductivity σ normalized by the concentration, is directly proportional to the diffusion coefficient, D. e_0 and N_A are the elementary charge and Avogadro's constant, respectively:

$$\Lambda = \frac{z^2 N_A e_0^2 D}{k_B T} \tag{3.1}$$

Which in turn is inversely proportional to the viscosity, η, through the Einstein-Nernst equation:

$$D = \frac{k_B T}{6\pi r \eta} \tag{3.2}$$

Where r is the effective radius (of the ideal spherical object diffusing). Combining the two equations, and using $N = nN_A$ where n is the moles of the charge carrier for a volume of V gives:

$$\sigma = \frac{z^2 e_0^2}{6V\pi r} \frac{N}{\eta} \tag{3.3}$$

To ensure that this high viscosity, which is inevitable due to the higher concentration, does not prevent the fluoride transport, the ionic conductivity and the self-diffusion coefficient were measured, respectively, using electrochemical impedance spectroscopy (EIS) and pulsed-field gradient (PFG) NMR at various concentrations. The ionic conductivity increased with the concentration due to the increased number of charge carriers, up to a maximum at a concentration of around 10 m then decreasing due to the increased viscosity as the concentration was further increased. The 25 m electrolyte exhibited an ionic conductivity of

around 152 mS cm^{-1}, about two orders of magnitude larger than previously reported for organic-based fluoride electrolytes.[138]

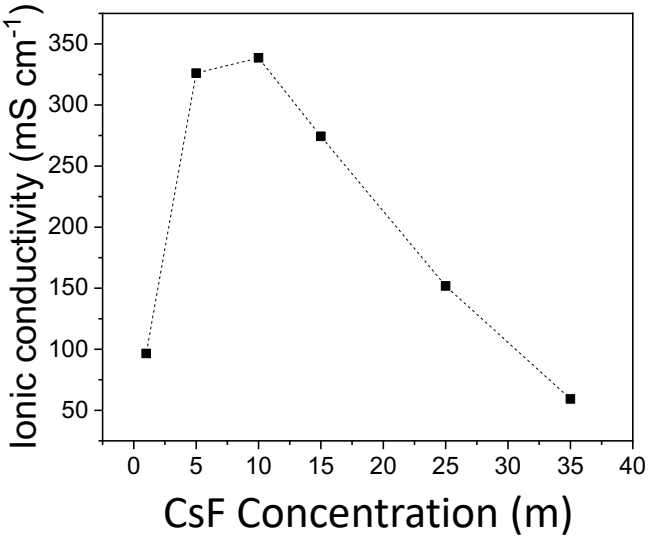


Figure 3.8: The ionic conductivity as a function of concentration for the CsF water-in-salt electrolyte.

Looking at the ^{19}F and ^{133}Cs ions under PFG NMR, the self-diffusion coefficient dropped from $2.45 \cdot 10^{-9}$ and $2.70 \cdot 10^{-9} m^2 s^{-1}$, for F^- and Cs^+ respectively, in the 1 m electrolyte to $2.51 \cdot 10^{-10}$ and $1.24 \cdot 10^{-10} m^2 s^{-1}$ for the 25 m electrolyte (Figure 3.9). Interestingly, as the diffusivity of both ions dropped due to the increased viscosity, the relative fluoride ion diffusivity increased significantly at higher concentrations, as seen in the increased fluoride transport number (Figure 3.9). This is likely due to the stronger Cs-O complexation at higher concentrations since more oxygen lone pairs become available for the cesium as the O$\cdots$H intermolecular interaction weakens due to the small water molar fraction. The ^{17}O NMR spectra (Figure 3.10a) corroborates this by showing the water oxygen peak shifting downfield as the oxygen electrons become increasingly deshielded by the Cs^+ interaction. This was also accompanied by significant peak broadening of the water ^{17}O peak, indicating less mobile water molecules that resembled ”solid-like” behavior. On the other hand, the ^{1}H peak (Figure 3.10b) is more shielded at higher concentrations, indicating weaker interaction

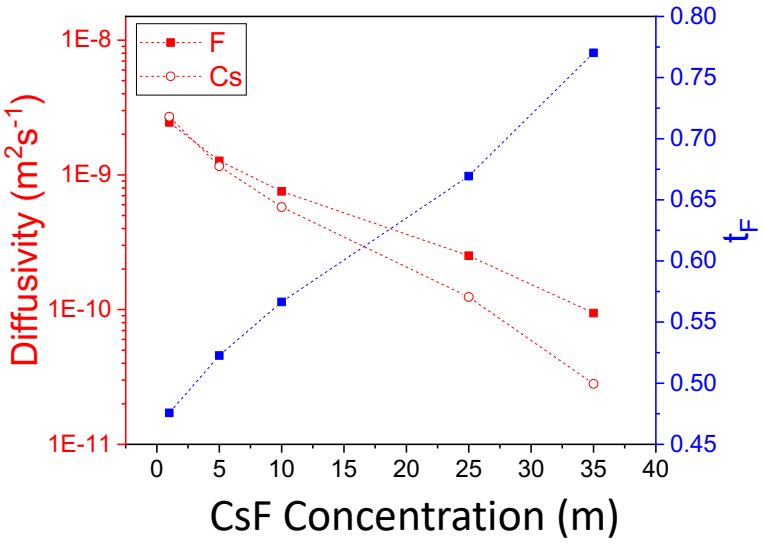


Figure 3.9: The self-diffusion coefficient and transport number as a function of concentration for the Cs and F ions in the water-in-salt electrolyte.

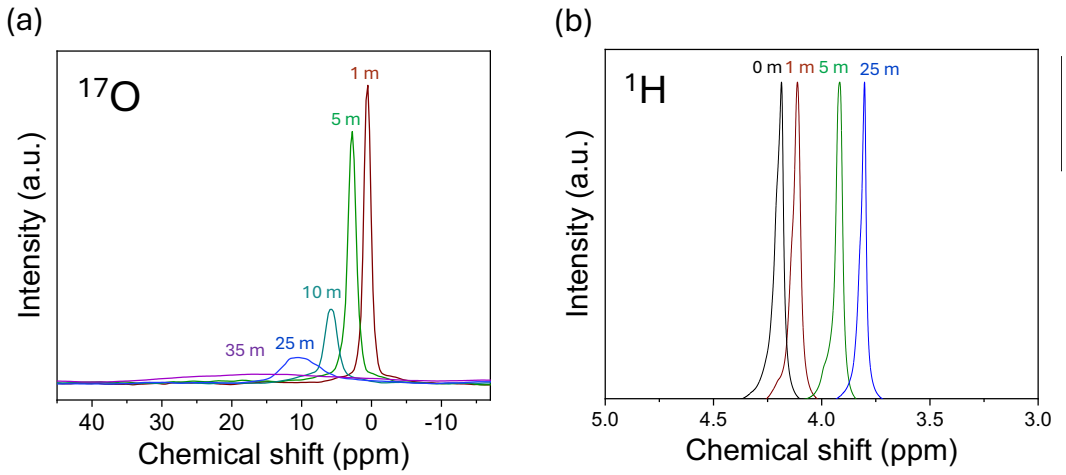


Figure 3.10: ^{17}O NMR spectroscopy showing the peak broadening and peak shift as the water molecules become less mobile (a), and ^{1}H NMR spectra shifting to higher frequency, opposing the trend observed in the ^{17}O and ^{19}F spectra (b).

with the electronegative fluoride ion. These results suggest a nearly immobile Cs-O network, leaving the fluoride ion to move more freely compared to the Cs^+ ion. Improved anion migration was also observed for other systems, where the cation was found to bind more strongly to the solvating molecule at higher concentrations.[139]

The solvation structure was further investigated as the electrolyte evolved from solvent-solvent and solvent-ion to ion-ion dominated interactions. Comparing the 25 m and the 1 m electrolytes, molecular dynamics simulations showed an increased presence of ion aggregates and contact ion pairs in the 25 m electrolyte compared to the 1 m electrolyte (Figure 3.11b), along with a rapid decrease in the fraction of free water molecules calculated based on a radial cutoff of 3.6 Å for Cs^+ and 2.8 Å for F^- (Figure 3.11a). This further confirms the previous ^{17}O NMR spectra showing increased Cs-O interactions compared to intermolecular hydrogen bonding and the improved ESW due to absence of free water molecules.

3.5 Chemical Stability Towards HF Formation

Using protic solvents in the presence of fluoride ion raises the concern of forming the corrosive hydrofluoric acid (HF) due to the deprotonation of the slightly acidic proton in the solvent molecule by the fluoride ion. In the case of water, diluted aqueous fluoride solutions are expected to have some amount of HF, although it would be small given the acid constant (pK_a) value of 3.8 for HF. Aqueous fluoride electrolytes have been previously cycled for up to 1000 cycles with sufficient stability.[23] Measuring the fraction of HF in solution, however, is still important to monitor the chemical stability and safety of the electrolyte and the effect of increasing the fluoride concentration. Ideally, ^{19}F NMR would show two separate ^{19}F signals, one corresponding to F^- and another to HF or any other protonated fluoride species (e.g., HF_2^-), each peak can then be integrated to quantify the fraction of the given species and obtain the $[HF_2^-]/[F^-]$ ratio. In protic media, however, the hydrogen exchange between F^-/HF is fast and known to result in a single ^{19}F NMR peak that is the average of all the fluoride species.[140] ^{19}F NMR is therefore incapable of determining the fraction of HF in the electrolyte. Alternatively, the HF concentration can be calculated by measuring the pH of the solution. pH meters measure the voltage and by comparing it to an internal

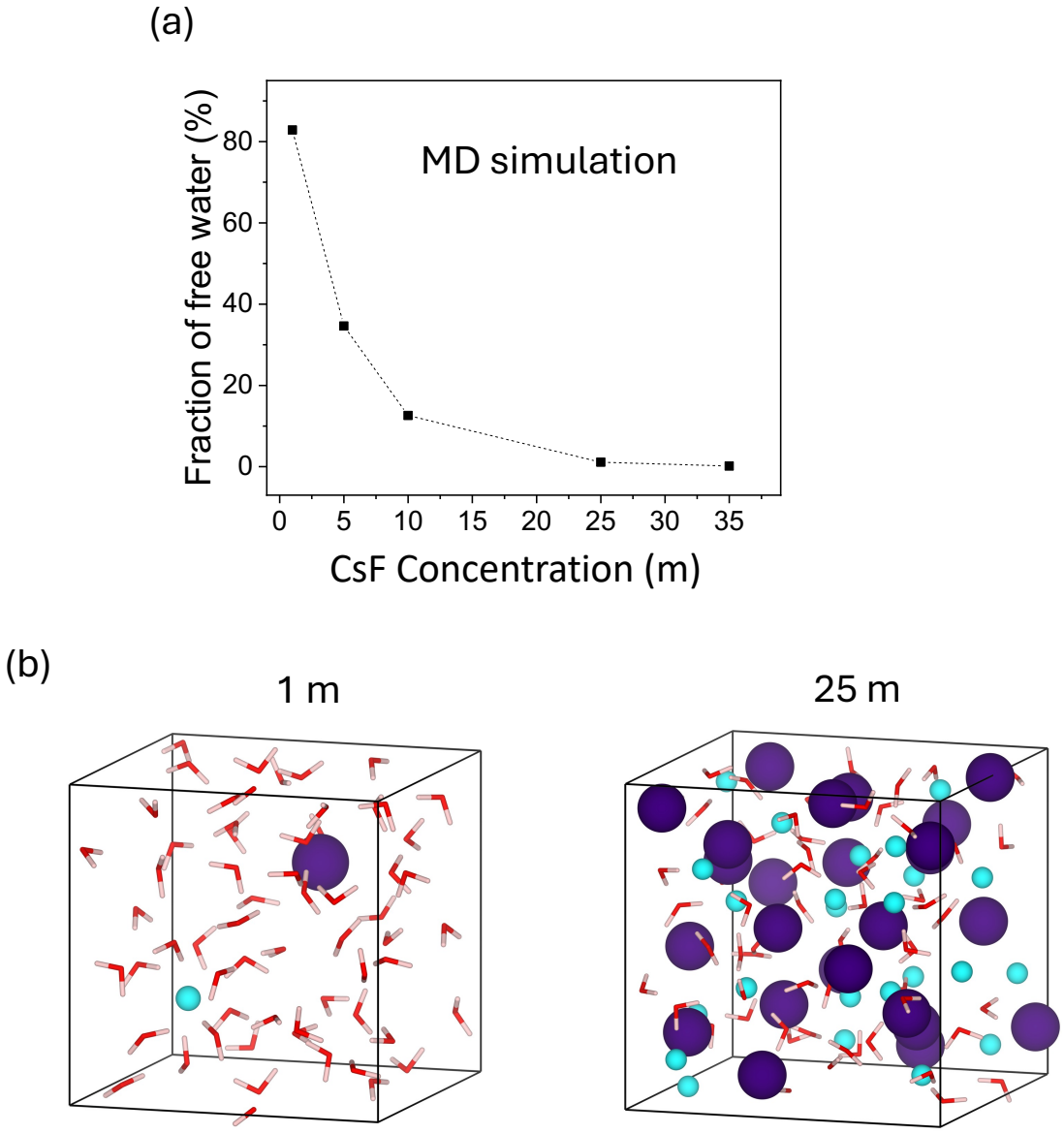


Figure 3.11: Fraction of free water molecules calculated from the MD simulation (a). Molecular dynamics relaxed structure at 1 and 25 m showing the formation of contact ion pairs and aggregates and elimination of free water molecules (b).

standard provide the activity of the H^+ from the Nernst equation, which then can be used to calculate the HF activity from the acid constant. For HF, the acid constant expression is as follows, where a is activity and K_a is the acid constant:

$$K_a = \frac{a_{F^-} a_{H^+}}{a_{HF} a_{H_2O}} \tag{3.4}$$

with rearranging:

$$\frac{a_{HF}}{a_{F^-}} = \frac{a_{H^+}}{K_a a_{H_2O}} \tag{3.5}$$

$$f_{HF} = \frac{a_{HF}}{a_{F^-} + a_{HF}} = \frac{1}{\frac{K_a a_{H_2O}}{a_{H^+}} + 1} = \frac{a_{H^+}}{K_a a_{H_2O} + a_{H^+}} \tag{3.6}$$

Where f_{HF} is the fraction of fluoride present as HF, a_{H^+} is the H^+ activity obtained from the pH measurement, and the water activity, a_{H2O}, would have to be calculated from the water concentration at different CsF concentrations.

Table 1. Calculated water concentration at various CsF concentrations.

CsF concentration (mol/kg)	[H_2O] (mol/L)
1	53.58
5	46.91
10	40.59
15	35.77
25	28.91

This method, however, has two main limitations, first is the highly concentrated solutions potentially affecting the voltage measurements, and second is the inherent discrepancy between the activity and concentration. Still, some reports suggest that pH measurements are still valid for concentrations >17 m.[141] Furthermore, the fast decay of %HF would still hold despite the deviation between the water activity and concentration, given the exponential decay of the

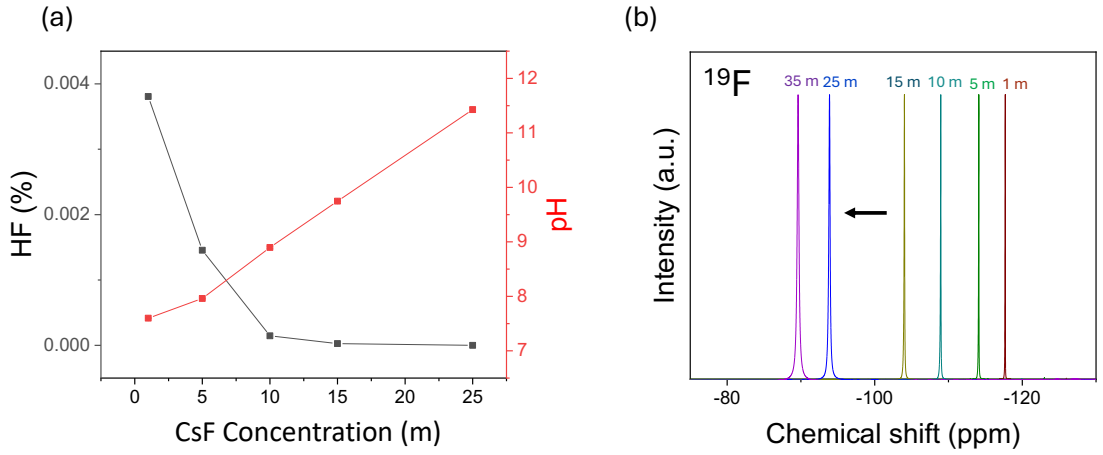


Figure 3.12: The fluoride ion chemical species and electronic environment. pH as a function of concentration indicating the decay of the HF content (a) and ^{19}F NMR spectroscopy (b).

measured a_{H^+}(Figure 3.12a) compared to the linear decay of the water concentration.

The HF content was found to decrease to near zero in the water-in-salt electrolytes as the water molecules donating the protons become more scarce and the solution more basic (Figure 3.12a). This observation is further confirmed by the increasingly deshielded fluoride in the ^{19}F NMR (Figure 3.12b). Despite the difficulty of comparing the ”nakedness” of the fluoride ion in multiple solvents due to other factors affecting the chemical shift (solvent electric dipole, magnetic anisotropy...etc.), comparing chemical shifts across the same solvent is a valid proxy for the fluoride solvation environment.[142] In this case, as the concentration is increased, the fluoride shifts away from the HF region (-160 to -170 ppm) [140], increasingly resembling the naked, less coordinated fluoride in organic solvents. This is also in agreement with the previously obtained ^{1}H NMR spectra, showing more and more deshielded protons at higher CsF concentrations, suggesting weaker interaction with the fluoride.

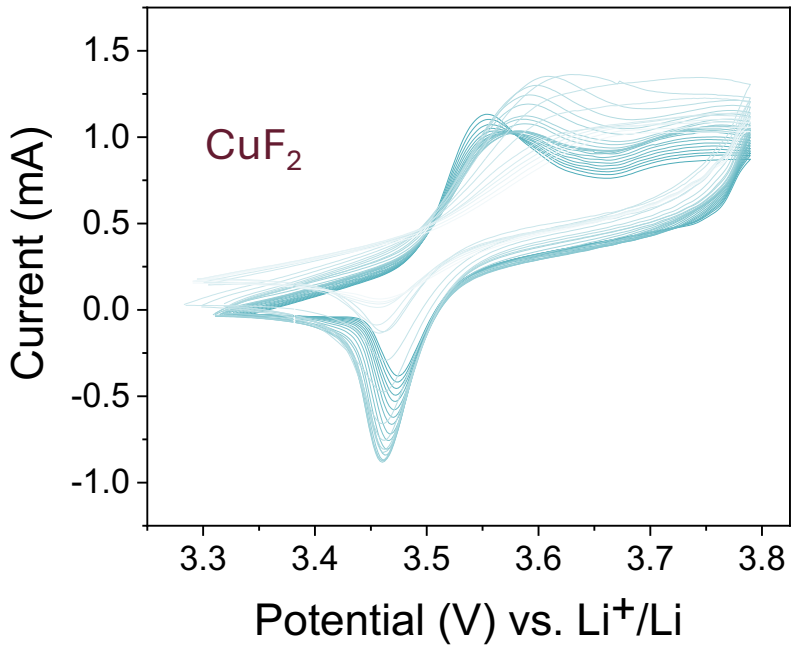


Figure 3.13: Cyclic voltammetry of CuF_2 in the 25 m electrolyte showing 30 cycles.

3.6 Galvanostatic and Potentiometric Cycling

The room-temperature cycling performance was explored using both galvanostatic and cyclic voltammetry for the 25 m water-in-salt electrolyte. First, CV was performed on CuF_2, a high-voltage (3.54 V vs. Li^+/Li) and high-capacity (528 mAh g^{-1}) cathode material that has been very difficult to cycle reversibly due to the formation of soluble intermediates, namely Cu(I).[143] For instance, a previous report by Davis et. al. reports less than 10 cyclic voltammograms before the entire capacity is lost. WiSE, however, shows 30 cycles without fully losing the output current.[41]

This is likely because WiSE can overcome the metal dissolution issue due to the high fluoride concentration, limiting any further active material dissolution. Given the solubility constant, K_{sp} of a metal fluoride (e.g., CuF_2 is constant, the equilibrium concentration of dissolved metal will significantly be suppressed due the increase in fluoride concentration, often to a power of 2-3 due to the multivalency of the corresponding cation:

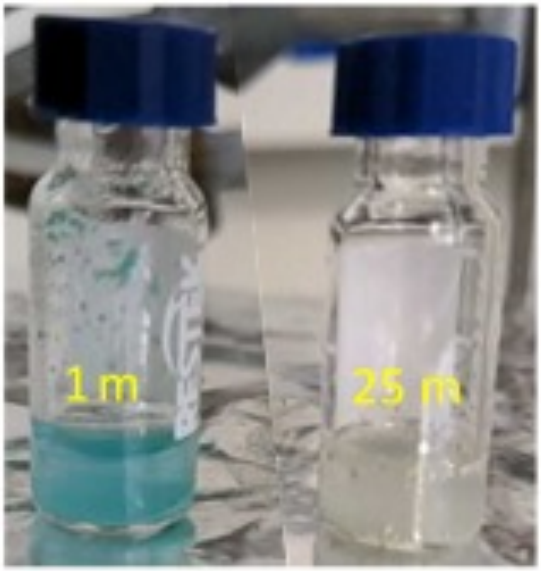


Figure 3.14: CuF_2 suspension in the 1 and 25 m electrolytes showing the elimination of the blue color (due to the dissolved $[Cu(H_2O)_6]^{2+}$) in the 25 m due to suppressed dissolution in the water-in-salt electrolyte.

$$K_{sp} = [Cu^{2+}][F^{-}]^2 \tag{3.7}$$

This can also be visually observed, as the blue color attributed to the water-complexed copper, $[Cu(H_2O)_6]^{2+}$], was observed in the 1 m electrolyte but not in the 25 m (Figure 3.14).

Cycling was also performed on more metal fluorides with high and low reduction potential, respectively, as potential cathode and anode materials. AgF_2 is amongst the highest-voltage binary metal fluoride, whereas ZnF_2 sits just above the oxidative limit of the WiSE electrochemical window (Figure 3.15).

To test a more realistic cell configuration and cycling conditions, coin-cells with PbF_2 electrodes were assembled and cycled at a C/10 rate. While both electrolytes started from similar initial capacity of around 135 mAh g^{-1}, the 25 m showed improved capacity retention compared to the 1 m (Figure 3.16b). A

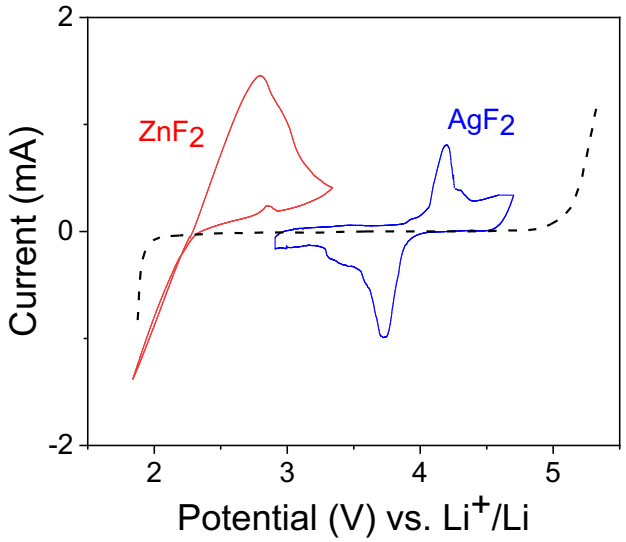


Figure 3.15: Cyclic voltammetry of AgF_2 and ZnF_2 near the oxidative and reductive limits of the WiSE electrochemical stability window.

subtle second plateau was observed in the galvanostatic voltage curve, most likely due to the formation of some $PbO/Pb(OH)_2$ in the aqueous electrolyte (Figure 3.16a). The PbF_2 symmetric cell indicates that the fluoride can be cycled using the WiSE in a conversion electrode, but it only serves as an initial platform for further cathode testing given that PbF_2 is not a practical cathode material and was chosen mainly due to its excellent fluoride conductivity and moderate redox potential.[63] Furthermore, the Ag-Zn redox pair, if assembled, would have an OCV of <2 V, still not fully utilizing the ESW of water-in-salt electrolytes, evoking the fundamental problem in FIBs lacking both high-potential (>4 V) cathodes and electrolytes with low (<1 V vs. Li^+/Li) oxidative limit.

3.7 Dilution and Potential Co-solvents

One way to further expand the limits of water-in-salt electrolytes is to explore potential co-solvents, or diluents, with wider electrochemical stability than water. An ideal diluent would consist of a low-viscosity solvent that can dilute the solvent-in-salt electrolyte without interfering with the local solvation environment, while

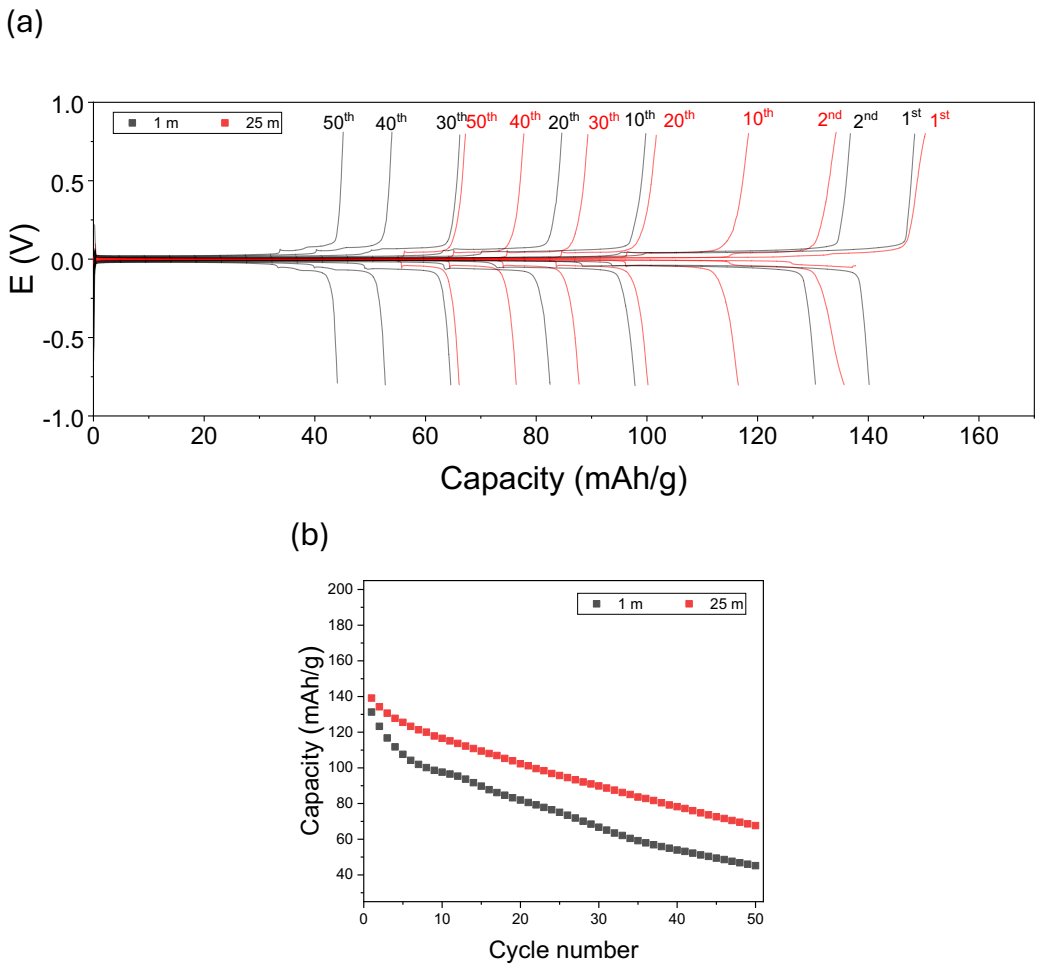


Figure 3.16: Galvanostatic cycling of symmetric Pb|PbF2 at 1 and 25 m showing improved capacity retention in WiSE.

also exhibiting inherent electrochemical stability. This can result in maintaining the advantages of a SIS electrolyte while reducing viscosity and cost, as seen for instance in the use of a fluoroether diluents into a concentrated LiTFSA/glyme resulting in a decrease in viscosity from 110 to 3 mPa s and an increase in ionic conductivity from 1.6 to 5.2 mS cm^{-1}.[134]

In the case of the CsF water-in-salt electrolyte, there are typically organic molecules that are miscible with water despite not necessarily interacting with the fluoride ion. Ethers have a low oxidative stability limit that allows their cycling with metallic lithium and potassium[144, 145] and are miscible with water in any ratio. Furthermore, their low donor number compared to water means

that it is expected that they don't interrupt the inner solvation shell to break the solvent-in-salt structure. Therefore, to test this, a 1:1 (v/v) ratio of the 25 m water-in-salt electrolyte and dimethoxyethane (DME) were vigorously mixed and allowed to settle (Figure 3.17). However, the aqueous and the DME phases separated, even though pure water and DME are miscible. The 1:1 (v/v) mixing was then carried out with more diluted aqueous CsF solutions, but they all phase separated except for the 1 m electrolyte. This mixing was also attempted using other solvents, such as sulfolane and tetraglyme, both showing similar results to DME. Furthermore, to formulate more systematic compositions, a ternary phase diagram was constructed using the solubility limit of CsF in water and given that CsF is completely insoluble in the co-solvent, and water and the co-solvent are fully miscible (Figure 3.18). Samples of four compositions (A, B, C, and D) presumably falling in the soluble region were prepared using, separately, G4 and acetonitrile. However, all prepared samples still phase separated, indicating that the solvation environment is possibly more complex than the constructed phase diagram, despite still holding for analogous ternary mixtures.[146] This is likely due to the small fraction of water which is unable to coordinate to both CsF and DME, leaving the organic phase out of solution. This indicates that if a co-solvent is to be used with WiSE, it would have to exhibit some interaction with the fluoride salt, just like ethers used to dilute the LiTFSI water-in-salt electrolyte can already solubilize lithium salts to form "ether-in-water" electrolytes[147], which brings back the need to develop aprotic organic solvents for the fluoride ion.

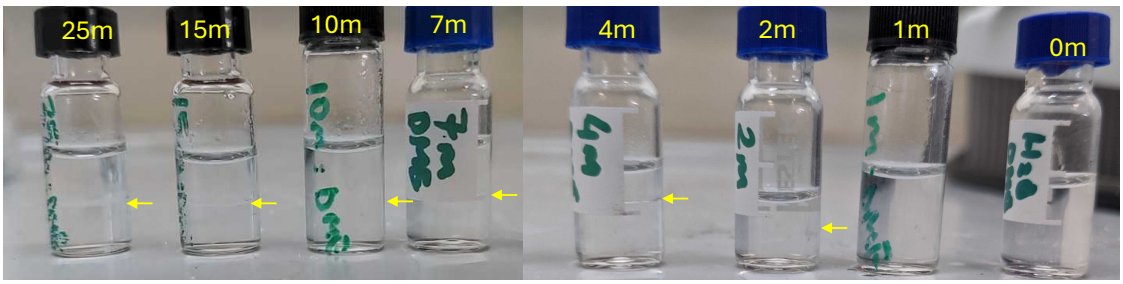


Figure 3.17: Samples of 1:1 v/v mixing of DME and WiSE at various concentrations showing phase separation between the aqueous and organic phases.

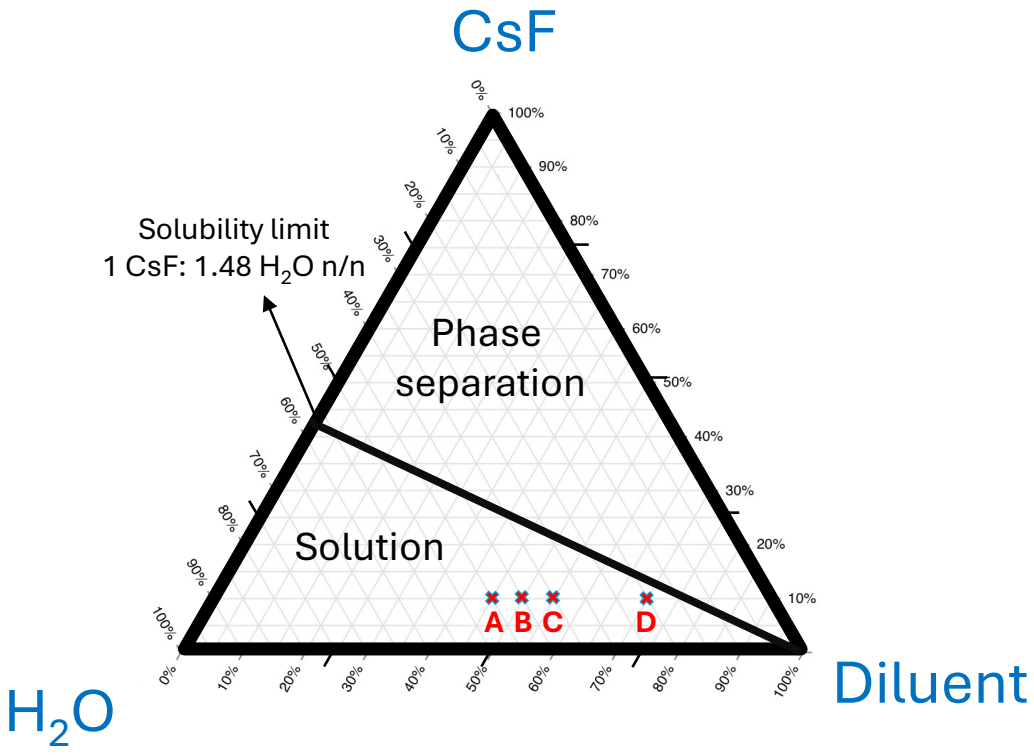


Figure 3.18: Ternary phase diagram of water, CsF, and a diluent that is miscible with water but incapable of dissolving CsF.

4

Aprotic Electrolytes[1]

Contents

4.1 Exploring the Aprotic Fluoride Solvents 82

4.2 Imidazolium-based Ionic Liquids as Fluoride Solvents . . . 84

4.2.1 Synthesis of TMAF and [MMIm][TFSI] 85

4.2.2 Chemical Stability of the Imidazolium Towards the Fluoride Ion 87

4.2.3 Fluoride-Imidazolium Solvation Structure 92

4.2.4 Thermal Properties 95

4.2.5 ESW, Ionic Conductivity, and Diffusivity 96

4.3 Molecular Solvents 97

[1] Parts of this chapter were published in *ACS Energy Letters* 9.12 (2024): 6104–6108.[148]

4.1 Exploring the Aprotic Fluoride Solvents

Despite the high solubility of fluoride salts in protic solvents, which enabled highly concentrated solvent-in-salt electrolytes with improved (electro)chemical stabilities, the fluoride solubility in aprotic solvents (e.g., carbonates, ethers, sulfolane) has been tenaciously low, preventing their practical use in battery electrolytes. For instance, potassium fluoride (KF) has a solubility of around 0.02 M in both DMSO and DMF[149], and an even lower solubility in ethers and carbonates due to their smaller dielectric constants. In solvents where it was slightly soluble, such as acetonitrile, fluoride ion was found to continuously deprotonate the acidic β hydrogens, degrading the electrolyte and forming hydrogen bifluorides and the corresponding olefin[150]:

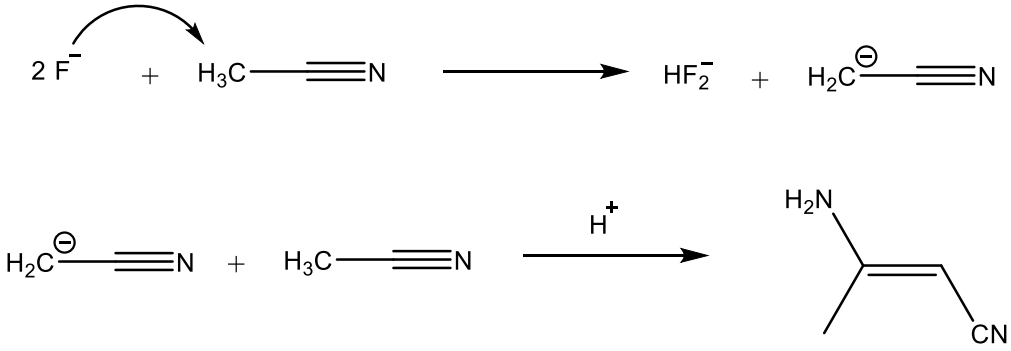


Figure 4.1: Deprotonation of acetonitrile by the fluoride ion to form HF_2^- and the corresponding alkene.

The reactivity of the acidic β hydrogens can also be problematic in other solvents, and even salt cations, where the presence of a good leaving group, X, such as an amine, can elicit E2 elimination reactions[4]:

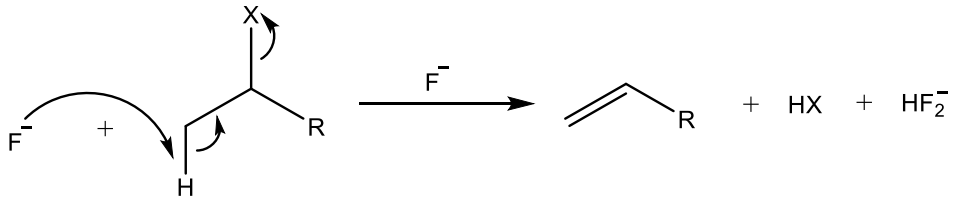


Figure 4.2: Reaction scheme of E2 elimination reaction catalyzed by the fluoride ion.

Besides the fluoride reactivity towards acidic β hydrogen, the selected aprotic solvent must lack any other halide atoms, as it can exchange with the fluoride ion. For instance, despite the reasonable fluoride solubility in chlorinated solvents (chloroform, ethylene chloride, and methylene chloride), the system was found to release Cl^- and increase in acidity upon dissolving the fluoride salt.[151] These restrictions made finding solvents for fluoride salts a problem even in synthetic chemistry, where the low fluoride solubility obliges higher temperatures and longer reaction times, which results in unwanted side reactions.[152] Therefore, expanding the array of aprotic solvents that can be used in fluoride-ion electrolytes is a tremendous but necessary challenge, as aprotic solvents are the only way to achieve electrochemical stability windows of >4 V while still enabling cycling at room temperature.

Keeping the fluoride reactivity in mind, one has to also consider the molecular motifs that will enable the fluoride solvation, as preventing chemical reactions should not come at the expense of solubility. Despite the reactivity of the fluoride towards the acidic β hydrogen, some acidity in the solvent hydrogen atoms is likely needed so that it can act as a hydrogen bond acceptor towards the fluoride, thus enabling the solubilization of the salt. With this rationale, aprotic solvents with mildly acidic protons were sought, so that the fluoride ion can be solvated by hydrogen bonding without full hydrogen abstraction. This was the fundamental structural design behind the Bis(2,2,2-trifluoroethyl) ether reported by Davis et. al.[41], which could achieve a solubility of 2.1 M, although still with some hydrogen bifluoride formation.

4.2 Imidazolium-based Ionic Liquids as Fluoride Solvents

Attractive possible solvents for the fluoride ion include ionic liquids, which are salts of typically large, asymmetrical ions with melting points below room-temperature. In an ionic liquid, the anion can influence the physical properties, such as melting point, the electrochemical stability, and hygroscopicity. Typical anions include PF_6^-, BF_4^-, TFSI, FSI, and AlX_4^- (X=Cl^-, Br^-). Aluminum halides, AlX_4^-, tend to be water sensitive, releasing HX upon the interaction with traces of moisture,[39] whereas hexafluorophosphate PF_6^- and tetrafluoroborates BF_4^- are both water and air resistant.[153] However, smaller anions lack the plasticizing effect needed to reduce the melting point below room temperature, which is the underlying reason ionic liquids based on PF_6^- and BF_4^- always have the highest melting points.[40] The choice of the cation, on the other hand, is even more influential in the context of a fluoride-ion electrolyte, as it can set the boundaries of the chemical stability and thus the potential formation of HF_2^-. Cations that comprise ionic liquids are typically quaternary ammoniums, imidazoliums, pyrrolidinium, piperidinium, or pyridiniums, in addition to sulfoniums [R_3S^+] and phosphoniums [R_4P^+] (Figure 4.3). Both pyrolidinium and piperidinium have β hydrogens that are prone to E2 elimination, whereas Pyridinium can undergo S_NAr substitution with the fluoride ion due to the presence of electron-poor aromatic ring. Imidazolium does not contain any β hydrogens or leaving groups like Pyrrolidinium and Piperidinium, and although it is aromatic like Pyridinium, it is considerably more electron-rich due to the presence of a second nitrogen atom. Besides chemical instability towards the fluoride, ionic liquids based on tetraalkylammoniums, pyrrolidiniums, piperidiniums, pyridiniums have considerably lower ionic conductivities in the range of 0.1-5 mS cm^{-1}, compared to around 10 mS cm^{-1} for imidazolium-based ionic liquids.[153]

Furthermore, imidazolium ionic liquids have polarities similar to small organic molecular solvents such as acetonitrile, DMF, and short chain alcohols[154],

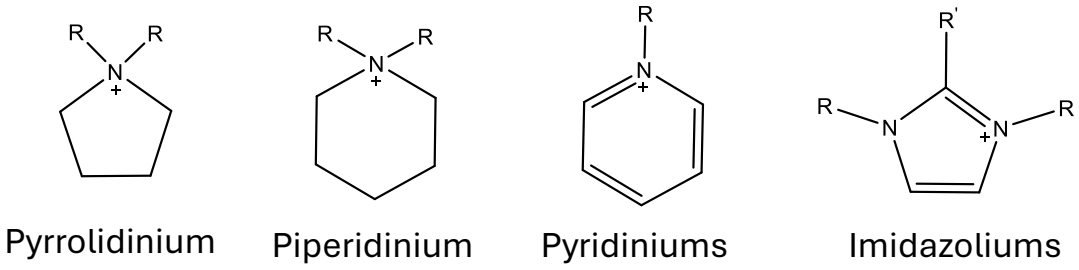


Figure 4.3: Structure of potential ionic liquid cations.

suggesting that it could have similar solubilizing abilities towards the fluoride ion due to its polarity, while still exhibiting the qualities of ionic liquids such as improved (electro)chemical stability and low vapor pressure. For the ionic liquid anion, TFSI exhibits the best trade-off between the plasticizing ability needed for low melting point compared to smaller anions (e.g., BF_4^-) and the enhanced chemical stability relative to other anions such as PF_6^- and FSI^-.

For these reasons, an ionic liquid based on 1,3-dimethylimidazolium TFSI, [MMIm][TFSI], was chosen as a reasonable starting point to study ionic liquid solvents for fluoride-ion batteries electrolytes. Methyl was chosen as the N-alkyl group to avoid longer chains with β hydrogens.

4.2.1 Synthesis of TMAF and [MMIm][TFSI]

The synthesis of [MMIm][TFSI] was carried out starting from 1-methylimidazole and through a chloride-free, one-step alkylation using methyl bis(trifluoromethanesulfonyl)imide as both the methylating agent and the anion-containing species. This synthetic design overcomes the traditional method which uses dimethyl sulfate and results in some residue of methyl bisulfate[155], an acidic side product that can directly form hydrogen fluoride.[156] Therefore, using the synthetic route proposed herein overcomes any side products, eliminating the need for an involved subsequent purification treatment. Furthermore, flushing the starting materials with argon and the performance of the reaction under argon aims to reduce any amounts of moisture dissolving into the obtained [MMIm][TFSI],

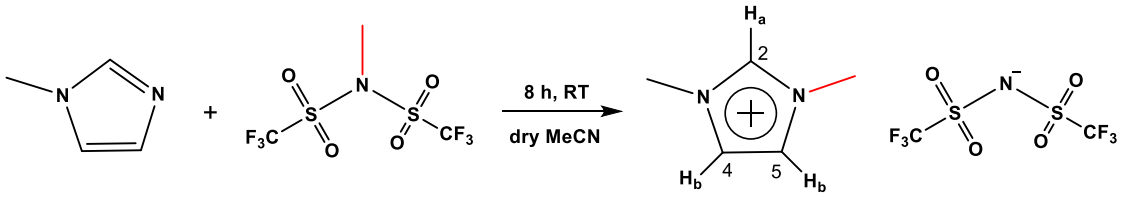


Figure 4.4: The [MMIm][TFSI] ionic liquid synthetic route.

resulting in a pure product with NMR spectra: 8.4 ppm (s, 1 H), 7.3 ppm (s, 2 H), 3.8 ppm (s, 6 H) for ^{1}H (400 MHz, DMSO-d_6), 135.8 ppm, 122.3 ppm, 118.8 ppm (q, CF_3), 34.5 ppm, for ^{13}C NMR (101 MHz, DMSO-d_6), and -80.93 ppm for ^{19}F NMR (376 MHz, DMSO-d_6)).

As for the choice of the fluoride salt, tetramethylammonium fluoride (TMAF) was selected due to its higher solubility compared to CsF, which was used in the water-in-salt electrolyte also for its lower price and availability, both needed for the highly concentrated electrolytes. Compared to other longer chain tetraalkylammonium fluorides, which can have higher solubility due to the anion-cation size mismatch resulting in a smaller lattice energy, TMA^+ has the highest electrochemical stability among the tetraalkylammonium cations due to the distribution of the positive charge over 12 hydrogen atoms.[71] In general, tetraalkylammonium cations have a limiting reduction potential ranging between 0.37 and 0.57 V (V vs. Li^+/Li).[80], which as described later will not be the limiting factor in the electrochemical stability window of TMAF in [MMIm][TFSI].

TMAF was synthesized starting from KF and $TMABF_4$, both dried under vacuum at temperatures of 250°C, and dissolved in dry methanol to form the KBF_4 precipitate. The filtrate was then collected and methanol removed under vacuum and a solvent trap, followed by elongated drying of the obtained TMAF at 150 °C for 3 days under high-vacuum (<10^{-3} mbar). The aim of this synthesis was to control the water-level in the synthesized TMAF, as both KF and $TMABF_4$ are less hygroscopic than TMAF.

Testing the solubility of TMAF in [MMIm][TFSI] at room temperature by comparing the integrations of the F^- and the solvent $TFSI^-$ peaks in ^{19}F NMR showed

a high solubility of 0.67 m (Figure 4.5). For comparison, the highest solubility aprotic fluoride solvent, BTFE, has a solubility of <0.1 m for TMAF.

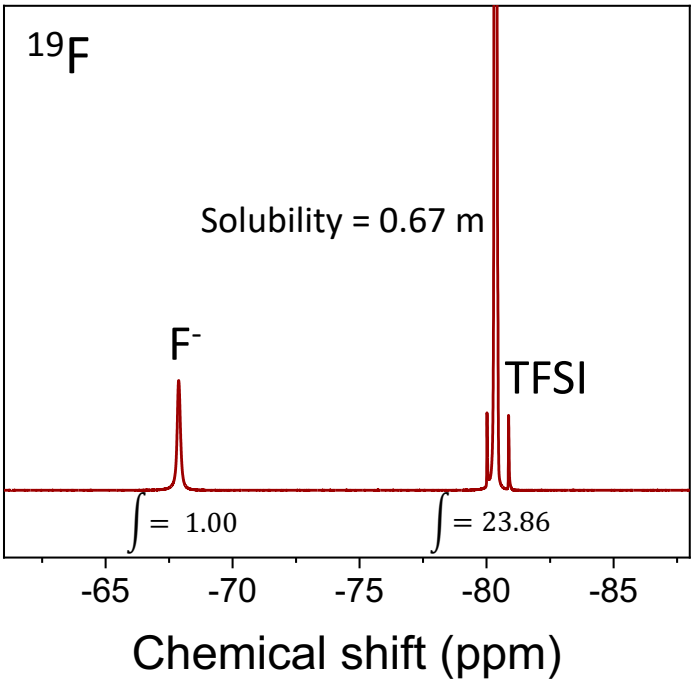


Figure 4.5: ^{19}F NMR for saturated TMAF in [MMIm][TFSI] showing a solubility of 0.67 m.

4.2.2 Chemical Stability of the Imidazolium Towards the Fluoride Ion

[MMIm][TFSI] exhibits the ability to solubilize TMAF at relativity high solubility. However, the chemical stability of the imidazolium cation towards the fluoride has to be confirmed, particularly whether 1,3-dimethylimidazolium forms the corresponding N-heterocyclic carbene (NHC) upon interacting with a base, B, such as the F^- ion:

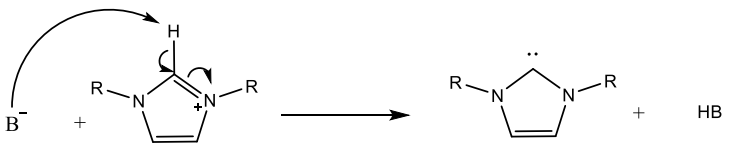
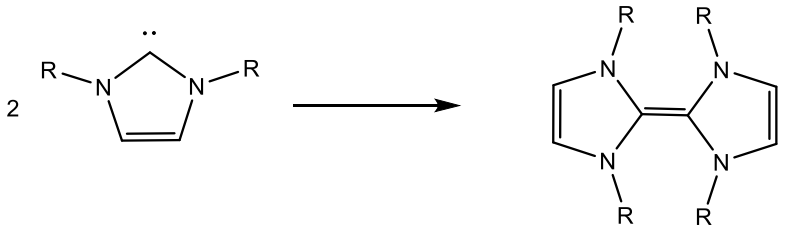


Figure 4.6: Reaction scheme of the potential deprotonation of imidazolium to form the N-heterocyclic carbene (NHC).

This potential deprotonation would be problematic due to the formation of HF_2^- but also due to the continuous degradation of the electrolyte solvent, potentially forming olefinic dimers also known as Wanzlick-carbenes[157]:



Whether the C2 carbene in imidazolium is prone to deprotonation and forming the NHC has been historically ambiguous. Though imidazoliums have widely been used in various chemical conditions with assumed chemical stability; it is also known that the C2 hydrogen can be exchanged with deuterium[158], and can be deprotonated by relatively mild bases such as 3-hydroxyquinuclidine (3-HQD) and 1,4-Diazabicyclo[2.2.2]octane (DABCO), both of which have pK_a values of 8-9.[159] This, however, is especially surprising given that the pK_a for imidazolium salts is around 24[160], suggesting that an equilibrium between DABCO and imidazolium would be strongly shifted towards the protonated imidazolium species. Furthermore, the fluoride ion has a pKa 3.2, meaning that it is a much weaker base than both 3-HQD and DABCO.

For these reasons, an extensive study on the chemical stability of imidazolium and the possible formation of NHC needs to be performed to confirm their chemical stability towards the fluoride ion and to eliminate the chance of continuously forming HF_2^-. First, ^{13}C NMR was used to probe the potential formation of new carbene species. Even though carbenes are known to be unstable, transient and hard to isolate, NHCs specifically are a lot more stable than other carbenes generated from azomethane or chloroform due to the presence of the two electron donating nitrogen atoms, which in previous reports enabled the monitoring of NHCs using ^{13}C NMR.[161]. Upon the addition of TMAF to [MMIm][TFSI], only one new signal was observed, with a chemical shift of 54.7 ppm attributed to the TMA^+ methyl group carbon, whereas the other signals, at 35.2 and 123.1 ppm

were due the imidazolium N-CH_3 and the two equivalent C4 and C5 carbons, respectively, and the 119.68 ppm quartet due to the CF_3 in $[TFSI]^-$ (Figure 4.7). Furthermore, carbenes tend to have ^{13}C NMR chemical shifts of around 206 - 220 ppm.[162] Looking more closely at this region in the TMAF in [MMIm][TFSI] ^{13}C NMR spectra (Figure 4.7 inset) shows no such signal exists, further confirming the absence of any NHCs in the electrolyte.

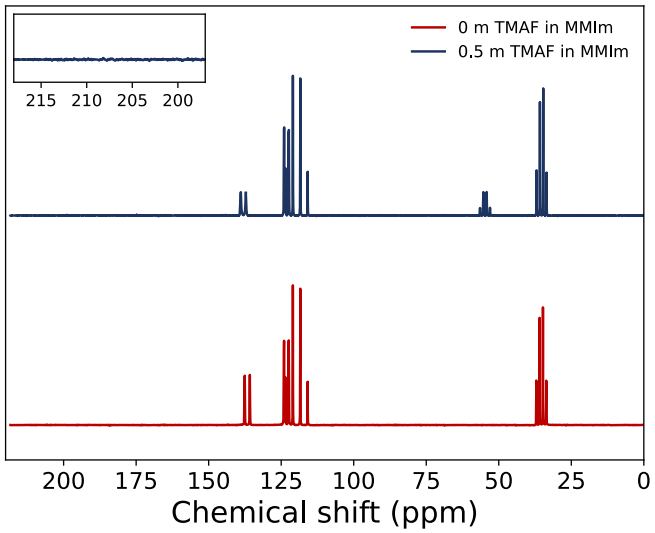


Figure 4.7: ^{13}C NMR for [MMIm][TFSI] and 0.5 m TMAF in [MMIm][TFSI] showing the absence of NHC species and the chemical stability of [MMIm][TFSI] towards fluoride deprotonation.

Performing electron paramagnetic resonance (EPR) can also shed light on whether carbene species are formed, specifically triplet carbenes since they are di-radicals with unpaired electrons that are visible under EPR. Fundamentally, the NHC carbene can exist as one of two electronic states, triplet, with the two nonbonding electrons occupying different electronic orbitals with parallel spin, or singlet, where both of the nonbonding electrons are paired (Figure 4.8).

EPR performed at -170 °C on the neat [MMIm][TFSI] shows only a broad background signal, which persisted after the addition of the TMAF salt. The temperature was therefore increased to RT to excite any singlet carbenes to a possible triplet state, but an identical EPR spectrum was obtained, further suggesting the absence of carbene species (Figure 4.9).



Figure 4.8: Electronic geometry for singlet and triplet carbenes showing the latter having two unpaired electrons.

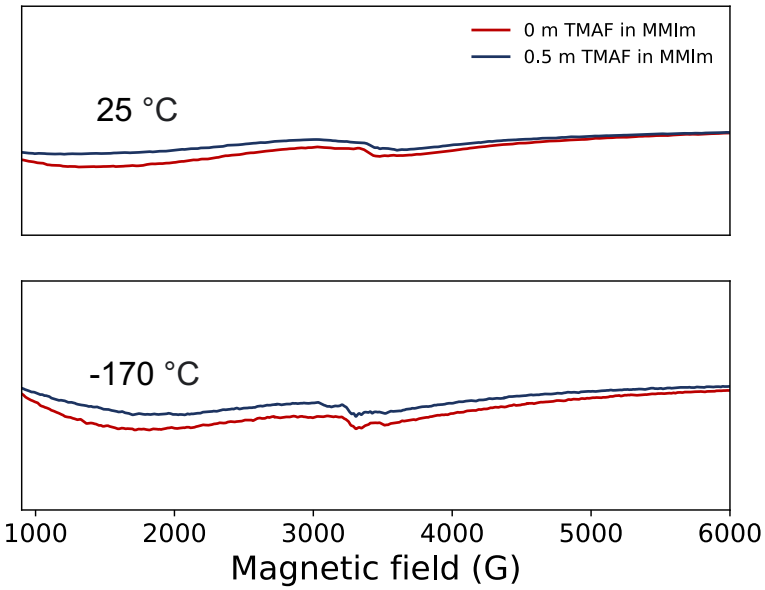


Figure 4.9: EPR for [MMIm][TFSI] and 0.5 m TMAF in [MMIm][TFSI] showing the absence of NHC species and the chemical stability of [MMIm][TFSI] towards fluoride deprotonation.

Finally, to probe the ground energy of the deprotonated species compared to [MMIm][TFSI], a DFT calculation was performed, showing that the protonated imidazolium is more thermodynamically stable, and further supporting the previous ^{13}C NMR and EPR evidence.

Despite the absence of any carbenes in the electrolyte, traces of HF_2^- were still observed in the ^{19}F NMR. This HF_2^- formation is likely due to the abstraction of a proton source other than the 1,3-dimethylimidazolium, which could only be traces of water in the system. Despite the meticulous drying, water still persisted in the synthesized TMAF at levels of 100-200 ppm due to its inevitable

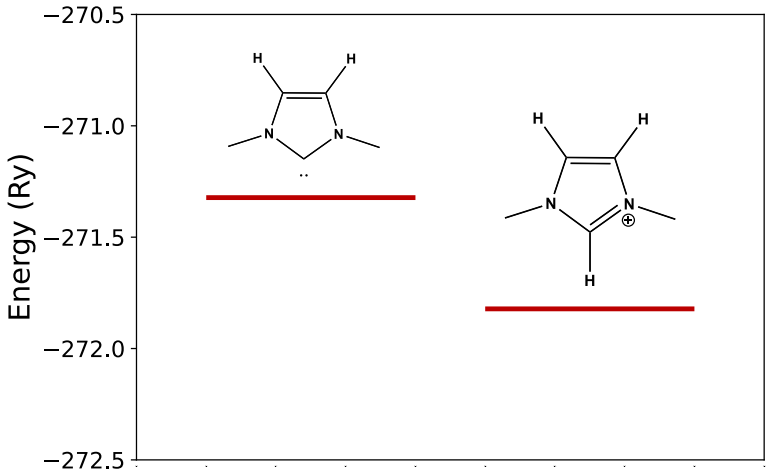


Figure 4.10: The ground-state energy for deprotonated imidazolium exhibiting higher energy compared to the imidazolium cation.

hygroscopicity. This formation of trace HF_2^- is similar to that observed in the BTFE solvent[41], which leaves open the question of whether F^- can ever exist in an aprotic solvent without trace amounts of the HF_2^-.

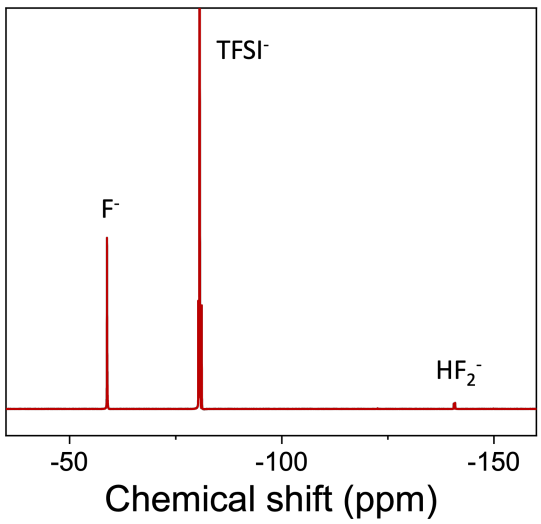


Figure 4.11: 0.5 m TMAF in [MMIm][TFSI] ^{19}F NMR spectrum showing a small peak attributed to HF_2^- at -141.85 ppm.

Still, [MMIm][TFSI] represents an improvement over the current fluoride solvents in terms of solubility, and as discussed later electrochemical performance, and is therefore worth exploring the solvation structure to gain insights into developing future solvents for FIBs.

4.2.3 Fluoride-Imidazolium Solvation Structure

The solvation structure of the fluoride in imidazolium was further explored to investigate the origin of the high solubility, and to gain more insight into the long-range ordering of both the F^- and TMA^+ in [MMIm][TFSI].

First, looking at the ^{1}H NMR spectroscopy for the imidazolium hydrogens at various fluoride concentrations can reveal which of these hydrogen atoms interacts more strongly with the fluoride ion, as the electronic environment of these protons would show larger correlation with the fluoride concentration. As the TMAF concentration was increased from 0.1 to 0.5 m, a more pronounced change in the ^{1}H NMR chemical shift was observed for the C2 proton (H_a), compared to the C4/5 protons (H_b) (Figure 4.12). This indicates that H_a exhibits some preferential solvation towards the fluoride ion compared to the other imidazolium hydrogen atoms.

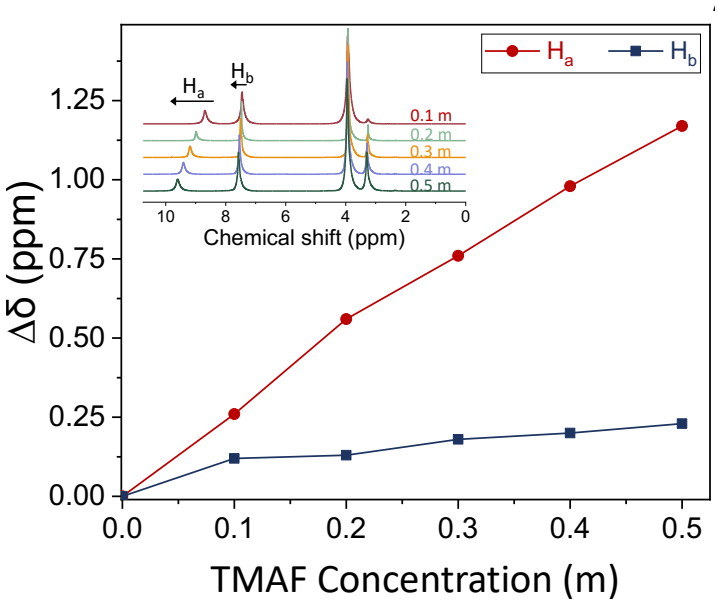


Figure 4.12: Preferential solvation revealed by ^{1}H NMR change in proton chemical shift at variable TMAF concentrations.

NMR spectroscopy, however, is not sufficient in determining the specific positions and distances of the solvating motifs. For this reason, neutron total scat-

tering was deployed to achieve real and spatial resolution and fully understand the structure of the liquid electrolyte. This neutron scattering pattern obtained experimentally can then be used to refine an MD simulation through empirical potential structure refinement (EPSR) to finally obtain partial radial distribution functions (RDFs) that describes the bonding environment of the various species in the electrolyte.

The CH···F partial radial distribution function, *g(r)*, in particular can uncover the nature of the fluoride solvation bonding, as the CH···F bond length is a direct measure of the bond strength and of whether this interaction is covalent (i.e., forming an HF bond), or simply based on weak hydrogen bonding. This crossover to the covalent character is known to occur at a bond length of around $\sim$ 1 Å.[163] The constructed CH···F RDF, however, for fluoride in [MMIm][TFSI] shows a first intense peak at 2.3 Å and another peak for the second solvation shell at 5.9 Å (Figure 4.13a). This indicates that the CH···F is a weak hydrogen bond with little to no short-distance HF covalent character. The distance-angle map for the CH···F shows two intense peaks, the first centered at 130° and the second closest at 40° (Figure 4.13b). This shows that the fluoride ion does not approach the solvating hydrogen head-on, resulting in a weaker C-H···F hydrogen bonding as characteristic from non-directional interactions.[164] This is somewhat expected given that C-H is not a particularly strong donor, as the carbon electronegativity is similar to that of hydrogen and the imidazolium ring provides two opposite effects of electron-donating due to the conjugation and electron-withdrawing nature of the highly electronegative nitrogen atoms. The spatial density function (SDF) from the imidazolium center-of-mass (CoM) encapsulates these findings obtained from the EPSR refinement (Figure 4.14); In this case, the multiple spheres do not represent multiple fluoride ions, as there is less than 0.2 fluoride atoms per imidazolium in accordance with the concentration, but is the probability distribution of the fluoride ion in the Imidazolium proximity. The SDF shows that the average position of the fluoride ion lies between the imidazolium C–H and the methyl hydrogens, with stronger interaction with the

C2 imidazolium C–H as evidenced by the shorter solvation bond length, thus confirming the preferential solvation observed previously in the ^{1}H NMR.

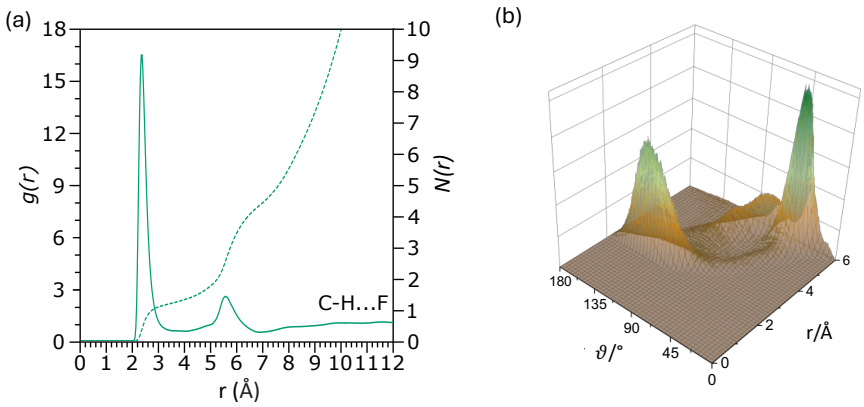


Figure 4.13: The partial radial distribution function, g(r) and coordination number N(r) for CH-F (a) and the distance-angle map for CH-F (b).

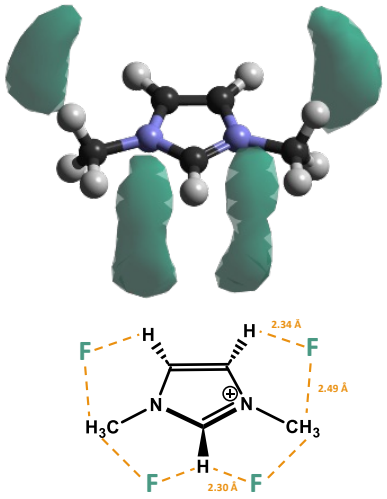


Figure 4.14: The spatial density function (SDF) for the fluoride ion around $[MMIm]^{+}$.

Looking at the partial radial distribution functions for the two counter cations, $[MMIm]^{+}$ and $[TMA]^{+}$, with respect to the fluoride ion shows high intensity peaks for both cations indicating highly localized interactions. For the $[MMIm]^{+}$ CoM this occurred at a 4.65 Å distance, while for the $[TMA]^{+}$ CoM it was 3.65 Å. Integrating the RDF curves up to the first *g(r)* minima (6.75 and 5.45 Å, for $[MMIm]^{+}$ and $[TMA]^{+}$, respectively) to obtain the coordination numbers shows that the fluoride

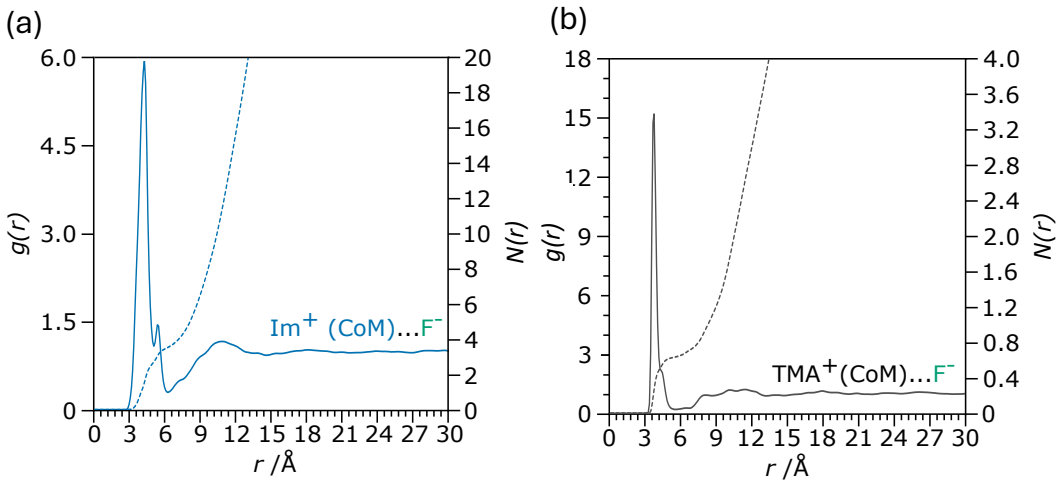


Figure 4.15: The MMIm-F (a) and TMA-F (b) radial distribution function, g(r), and coordination number, N(r).

ion first solvation shell contains *ca.* 5 $[MMIm]^+$ and 0.6 $[TMA]^+$ cations. This low coordination number for the $[TMA]^+$, in addition to the lack of *low-Q* signals in the neutron scattering, indicates the absence of $[TMA]^+$ and F^- ion clustering. In other words, this electrolyte is a mixture of four statistically distributed ions: $[MMIm]^+$, $[TMA]^+$, F^- and $[TFSI]^+$.

4.2.4 Thermal Properties

One of the main advantages of using ionic liquids as electrolytes is their low vapor pressure and extended thermal stability. Performing TGA on the 0.1 m TMAF in [MMIm][TFSI] electrolyte shows no thermal degradation up to 400 °C (Figure 4.16a). This is especially surprising given that the decomposition of solid TMAF happens around 170 °C,[150] suggesting that the strong solvation and the random distribution of the TMAF ions breaks any of its ionic character.

Furthermore, DSC curves for the same electrolyte show no thermal processes occurring at high temperatures. Temperatures of -14.43 °C and 19.2 °C for the liquid-to-solid and solid-to-liquid transitions, respectively, were observed (Figure 4.16b). This disparity between freezing and melting temperatures is due to supercooling, where lowering temperature increases viscosity and prevents the

diffusion necessary to form the first seed crystals. This is especially common in ionic liquids due to their higher viscosity, and it can be overcome by using a slower heating rate in DSC. This is why some prefer reporting this liquid-like to solid-like transition in terms of T_g, or simply as 'solidification temperature' instead of freezing point, since it is more of a kinetic transition as opposed to freezing, which has a determined value where the crystal is energetically more stable than the liquid. The discrepancy between the melting and solidification points in ionic liquids can be as high as 200 °C[39], whereas the temperature difference observed here is 33.6 °C.

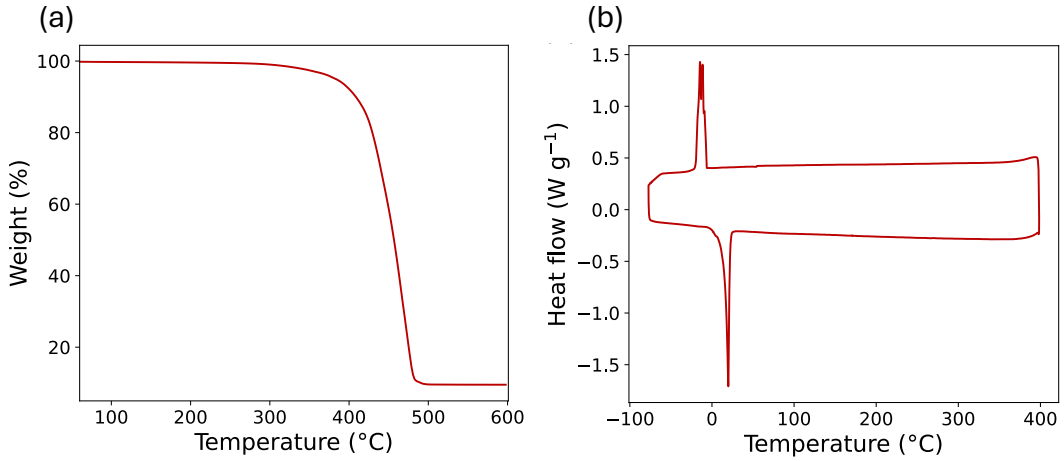


Figure 4.16: Thermogravimetric analysis (TGA) (a) and Differential scanning calorimetry (DSC) (b) for 0.1 m TMAF in [MMIm][TFSI] showing thermal stability up to 400°C.

4.2.5 ESW, Ionic Conductivity, and Diffusivity

Given the high fluoride solubility and chemical stability of [MMIm][TFSI], the electrolyte transport and electrochemical properties were subsequently examined. The ionic conductivity was measured using electrochemical impedance spectroscopy (EIS) to be 9.53 mS cm^{-1} for the 0.1 m electrolyte, decreasing to 6.16 mS cm^{-1} for the 0.5 m (Figure 4.17a). This trend is in agreement with previously reported ionic conductivities of ionic liquids, decreasing monotonically with increasing salt concentration due to the increased viscosity.[165, 166] The fluoride

diffusivity, determined by pulse-field gradient (PFG) NMR spectroscopy, also matched this trend, with self-diffusion coefficients ranging between 2.32·10^{-11}m^2 s^{-1} and 1.36·10^{-11} m^2 s^{-1} for the 0.1 and 0.5 m, respectively (Figure 4.17b).

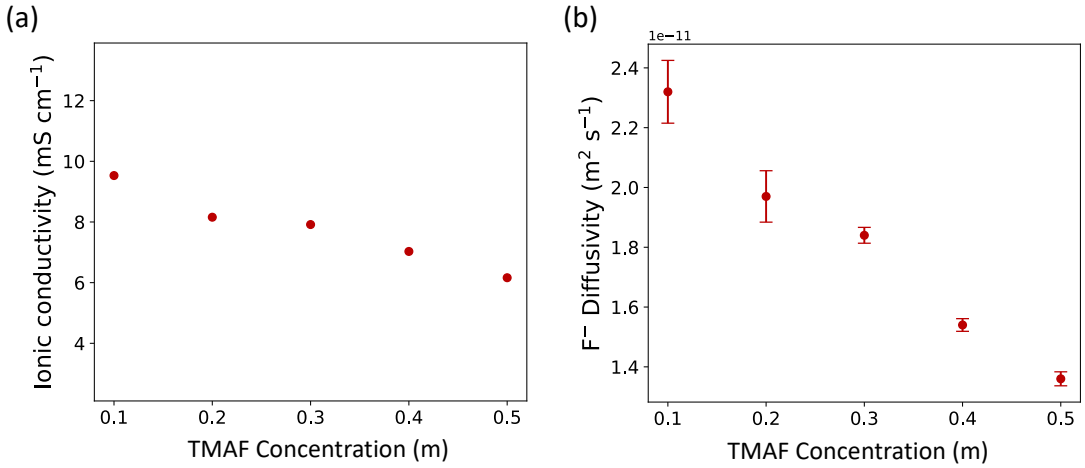


Figure 4.17: The fluoride-ion diffusion coefficient (a) and ionic conductivity (b) at variable TMAF concentrations in [MMIm][TFSI].

The ESW was measured using linear sweep voltammetry (LSV) to be 4.65 V (Figure 4.18a) using a 100 μA cm^{-2} current density cutoff. This, to the best of our knowledge, is the highest ESW reported thus far for a FIB electrolyte. Finally, cyclic voltammetry showed that the achieved diffusivity and ionic conductivity were sufficient to cycle both high and low voltage metal fluorides such as AgF_2 and MnF_2 (Figure 4.18b).

4.3 Molecular Solvents

Besides ionic liquids, molecular solvents can also be an attractive option for fluoride-ion electrolyte solvents, despite previously suffering from low fluoride solubilities and chemical degradation. Building on Bis(2,2,2-trifluoroethyl) ether (BTFE), the state of the art aprotic solvent for FIB electrolyte which despite exhibiting relatively high solubility suffers from a low boiling point of 63 °C.[41, 43] However, the ultimate advantage of the aprotic molecular solvents is that their

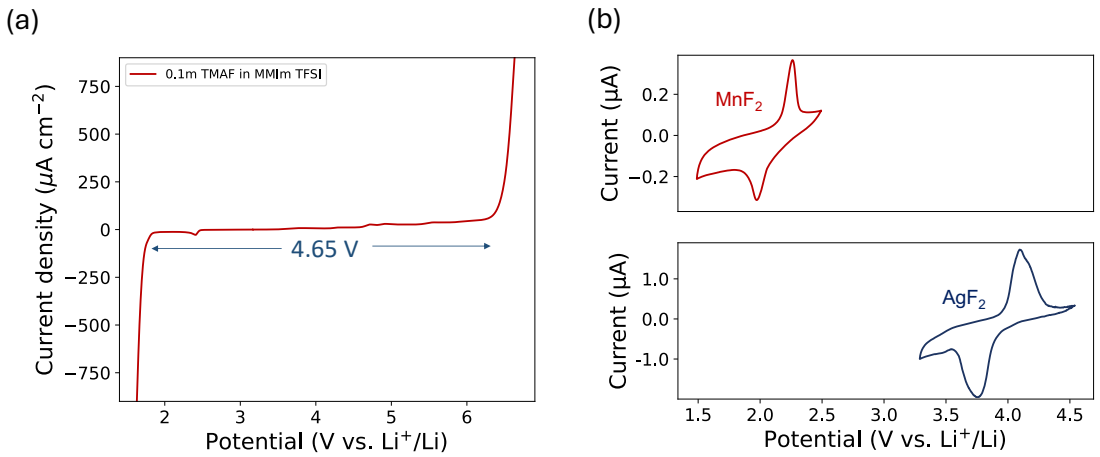
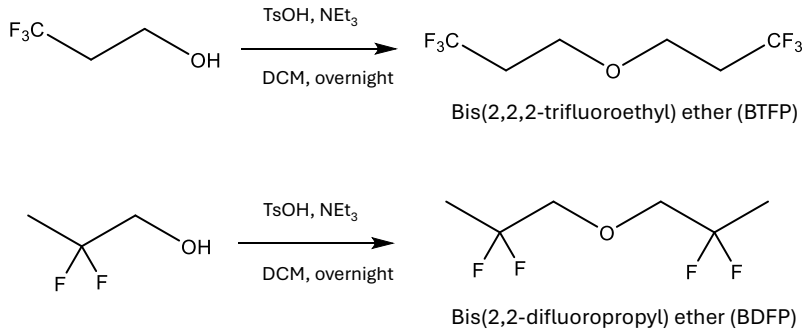


Figure 4.18: The electrochemical stability window (a) and cyclic voltammograms for MnF_2 and AgF_2 (b) in 0.1 m TMAF in [MMIm][TFSI].

ESW extends over low potentials, that is voltages below 1 V (vs. Li^+/Li), which has not been possible using both solvent-in-salt electrolytes and imidazolium-based ionic liquids. This ESW covering lower potentials is essential to enable the cycling of anode materials with low potentials (e.g., La, Ca) as despite the [MMIm][TFSI] exhibiting the widest ESW, no cathode materials with fluorination reduction potentials higher than 4 V (vs. Li^+/Li) is yet known, leaving over 2 V of the potential window unused. Scanning the commercially available aprotic solvents, while keeping in mind the reactivity conditions discussed earlier in the chapter, a group of molecular solvents were investigated for fluoride solubility (using TMAF) and chemical stability, particularly those with the -OCH_2CF_3 moiety, which is expected to be solvating the fluoride ion in BTFE.[41] Bis(2,2,2-trifluoroethyl) carbonate (BTFC) and 3,3,3-Trifluoropropylene carbonate (TFPC) are fluorinated analogs of the commonly used lithium-ion electrolyte solvents ethyl carbonate (EC) and propylene carbonate (PC), both of which exhibit wide ESW but are incapable of dissolving fluoride salts. Introducing the electron withdrawing fluorine atoms increases the hydrogen bond donor ability and can potentially enable solvation. However, ^{19}F NMR for a saturated then filtered TMAF solution in the given solvent showed that BTFC did not show any practical solubility, while TFPC and TFMP reacted to form new side products, the latter

reacting vigorously to form a black color. Hexafluorobenzene, which might have formed a complex with the fluoride ion due to its extremely electron poor aromatic ring, was also found to be unable to dissolve any fluoride salt as evident by the absence of any new F^- peaks (Figure 4.19). These results indicate that the fluoride ion is not stable towards the phosphonate group, possibly due to some nucleophilic reaction at the phosphorus center. Still, it would be worth exploring BTFC with more soluble salts than TMAF, as the solubility of the latter, despite being impractically low, was larger than that measured for BTFE (ca. 1/40 and 1/15 F^-/solvent molar ratio for BTFE and BTFC, respectively), although both with traces of HF_2^-, unlike HFB which showed no F^- peaks.

Furthermore, to build on the ether solvents with the -OCH_2CF_3 moiety capable of solvating the fluoride ion, the synthesis of longer chain fluorinated ethers to achieve boiling points higher than BTFE was investigated. Two solvents were first explored, with synthetic routes starting from the corresponding alcohols:



Where BTFP and BDFP have expected boiling points of 112 and 135 °C, respectively. The synthesis was first designed to involve two steps, first the tosylation of the alcohol using TsOH and triethylamine, followed by separation then the substitution reaction to form the ether. However, after running the reaction overnight the ether was observed by NMR, with trace amounts of the fluorinated tosyl ester. This preliminary synthesis serves as a stepping stone to further investigate BTFP and BDFP and many other ethers, as fluorinated alcohols are

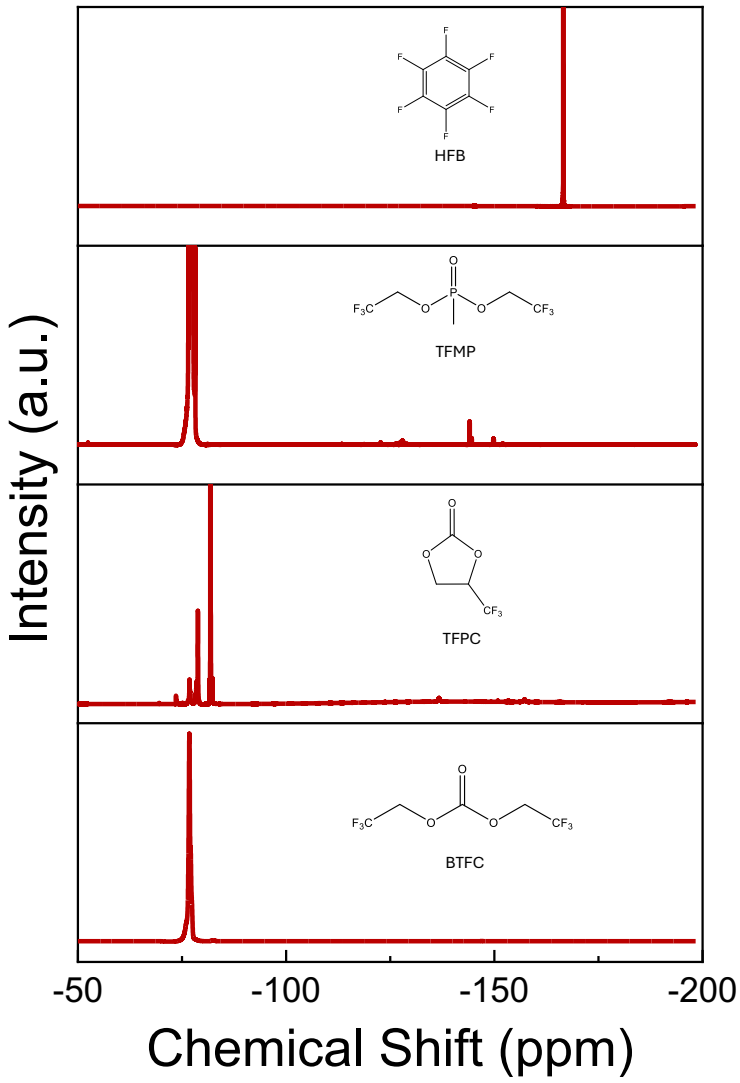


Figure 4.19: ^{19}F NMR for some investigated aprotic molecular solvents: hexafluorobenzene (HFB), Bis(2,2,2-trifluoroethyl) methyl phosphonate (TFMP), 3,3,3-Trifluoropropylene carbonate (TFPC), and Bis(2,2,2-trifluoroethyl) carbonate (BTFC).

widely available, and then to explore their fluoride solubility, chemical stability, and electrochemical performance.

5

Electrodes for Fluoride-Ion Batteries

Contents

5.1 Hunting Down the Perfect FIB Cathode 104

5.2 Positive Electrodes Based on Cu/CuF_2 106

5.2.1 Synthesis of Monodisperse Cu Nanocubes 108

5.2.2 In-situ Fluorination of the Cu Nanocubes 114

5.3 Reference Electrodes for FIBs 115

5.4 The Future of FIB electrodes 118

5.1 Hunting Down the Perfect FIB Cathode

While the electrolyte design is crucial for the battery performance, as it determines the F-ion conductivity, rate capability, and the electrochemical stability, the electrodes are ultimately what determine the discharge capacity and reversibility of the cell. As the FIB is discharged, the metal fluoride cathode releases the fluoride ions to the metal anode, changing the oxidation state of both metals and enabling the electrochemical reaction. The rate and reversibility of this conversion reaction at high operating voltages is what will determine whether FIBs can achieve their desired high energy densities.

At first glance, it can be thought that metal fluorides with small molecular weights could be the ideal cathode materials for high energy density FIBs. However, many other parameters need to be considered to achieve the reversible (de)fluorination necessary for practical FIBs. First, small volume change between the metal and metal fluoride is needed to avoid excessive local strains during the conversion reaction, which could result in contact loss and quick capacity fading. Second, metal fluorides with minimal solubility in the electrolyte are preferred to avoid active material dissolution. Furthermore, high electronic and ionic conductivity would be ideal to facilitate the fluoride diffusion conversion reaction with minimal additives of conductive carbon and to alleviate the need for small particle size. Moreover, the metal fluoride has to be low-cost with a resilient supply chain. Finally, and more importantly, the cathode has to have high gravimetric capacity (in mAh/g) and high reduction potential to enable high energy density FIB. These various variables need to be considered concurrently while selecting FIB cathode materials.

The ionic conductivity of the metal fluoride is largely determined by its crystal structure.[15] Fluorite-type ($Fm\bar{3}m$) and Tysonite-type ($P\bar{3}c1$) metal fluorides are considered 'superionic' fluoride conductors, although only at elevated temperatures.[167, 168] Furthermore, these materials have low reduction potentials due

to the electropositivity of their constituting metals (Ca, Ba, and Sr for Fluorite-types, La, Ce for Tysonite-types) which prevents their use as high-voltage cathode materials. Other metal fluorides include the divalent metal fluorides with tetragonal crystal structures, such as PbF_2 and MnF_2 ($P4_2/mnm$). PbF_2 in particular has a reasonably good fluoride ionic conductivity of 10^{-7} S cm^{-1},[169] which is one reason why PbF_2 has been widely used to study fluorination reactions in FIBs. However, its low reduction potential of 2.89 V (vs. Li^+/Li) and the low gravimetric capacity due to the high molecular weight of lead renders it an impractical cathode material.

Unlike ionic conductivity, electronic conductivity is determined by electron energy levels, or the difference between the conduction and valence bands. Unfortunately, all metal fluorides have large band gaps due to their ionicity which render them electronically insulating, meaning that the electronic conductivity can only be enhanced using smaller particle size and by infusing conductive carbon.

Perhaps most importantly of all the parameters is the reduction potential and specific capacity of the metal fluoride cathode, as these determine the energy density of the FIB. AgF_2 has the highest potential at 4.48 V (vs. Li^+/Li) (Table 1.1), but the low specific capacity dictated by the large molecular weight, along with the high cost of silver, are prohibitive. HgF_2 has also a high reduction potential of 4.15 V vs. Li^+/Li but with a low and unappealing specific capacity of 224.6 mAh/g. Iron fluorides are low-cost, low-molecular weight, which results in a reasonable capacity of 712.5 and 571.12 mAh/g for FeF_3 and FeF_2, respectively, but they suffer from low potentials of 2.62 - 2.74 V vs. Li^+/Li. Co and Ni fluorides are also potential candidates, with a 693.60 mAh/g capacity and 3.61 V potential for CoF_3 and a slightly lower capacity and potential for CoF_2, whereas NiF_2 has 554.4 mAh/g capacity and 2.97 V. SnF_2, although not a transition metal, is also an interesting choice of cathode, as it has similar fluoride conductivity to PbF_2 but with higher reduction voltage of 2.97 V vs. Li^+/Li, but it suffers from a severely low capacity of 342.1 mAh/g. BiF_3 has also been extensively demonstrated and widely reported as a FIB cathode. Despite its appealing low

cost, bismuth has a high molecular weight that results in a low specific capacity of 384.7 mAh/g. Based on this, CuF_2 seems to have the highest reduction potential and capacity compared to the other metal fluorides and is the most appealing of the metal fluorides.

Besides binary metal fluorides, ternary fluorides can also potentially be FIB cathode materials. However, these materials tend to have lower gravimetric capacity due to the presence of atoms that do not undergo an electrochemical redox reaction while still contributing to the mass of the cathode. A study by McTaggart et al., which screened all multi-atom fluoride/non-fluoride pairs posited that the highest capacity of the ternary fluorides was $NClOF_4$/NClO at 758 mAh/g.[170] However, a practical synthesis of $NClOF_4$ has not been known to the best of our knowledge.

Table 5.1: Metal fluoride cathodes electrochemical parameters derived from Gibbs free energy of formation and density of metal/fluoride pairs.[4]

Active Material	**Redox Potential (V. vs. Li+/Li)**	**Specific Capacity (mAh/g)**	**Volume Change**	**Metal Price (US$/kg)**
AgF_2	4.48	367.48	5.89%	$500-600
CuF_2	3.54	528	237%	$7–$9
CoF_3	3.61	693.6	21.01%	$20-$30
BiF_3	3.18	384.7	50%	$5–$6
FeF_3	2.74	712.53	311%	$\sim$ $1
NiF_2	2.96	913.32	211%	$18–$20
SnF_2	2.97	342.1	5.04%	$17

5.2 Positive Electrodes Based on Cu/CuF_2

Due to its high capacity and high reduction potential, CuF_2 seems to be the most promising cathode material, despite suffering from low electronic and ionic conductivity and large volume change during (de)fluorination (Table 1.1). These hurdles, however, can be overcome by tuning the particle size, using conductive additives, and utilizing flexible binders and coatings to overcome the large

change in volume. Unlike other metal fluorides whose intrinsically lower capacity and reduction potential prevent high-energy density cathodes, CuF_2 can enable higher energy densities with proper material design. This is one reason why CuF_2 has been investigated as conversion cathode material for Li-ion batteries, following the reaction:

$$CuF_2 + 2Li^+ + 2e^- \rightarrow Cu + 2LiF$$

The CuF_2 conversion has been utilized in LIB cathodes with some, although still unsatisfactory, levels of success. Typically, CuF_2 cathodes lose capacity after 5-10 cycles due to mainly four reasons. First, the low electronic conductivity of CuF_2, which itself is a result of the highly ionic Cu-F bond, reduces the reaction reversibility and kinetics and giving rise to low coulombic efficiencies and poor rate capability. Second is the high voltage hysteresis (up to 1 V), which stems from the large activation energy barrier required to break the Cu-F and Li-F bonds during conversion. Third, the coarsening of the Cu particles and the phase separation due to the higher mobility of Cu which disturbs the conductive network and forms non-conductive islands within the cathode composite. Fourth, and perhaps most importantly, is the active material dissolution which results in irreversible capacity loss.[143, 171, 172]

However, a few reports have partially overcome this adverse CuF_2 capacity fading in LIBs. For instance, sodium alginate was used as a binder to form a network structure that insulates cation migration and suppresses the dissolution of CuF_2, achieving 420.4 mAh/g reversible capacity after 50 cycles.[173] In another report, a polymer based on PIL-PVDF-HFP (PPH) was used to achieve a capacity of nearly 500 mAh/g while lowering the voltage hysteresis (overpotential) from 700 to 50 mV.[174] In both of these reports, superior copper conversion was achieved, it was claimed, by stabilizing the metastable Cu(I) phase which is more soluble and typically is assumed to cause capacity fading due to active material dissolution. By introducing a polymer that can coordinate to Cu(I), an alginate or a PIL-PVDF-HFP, better capacity retention is achieved. While the existence of

Cu(I) fluoride has been controversial, it was recently shown using XPS and EPR, as Cu(II) is paramagnetic ($4s^0\ 3d^9$) while Cu(I) is diamagnetic ($4s^0\ 3d^{10}$), along with a Raman peak at 216 cm^{-1} corresponding to the $2\Gamma_{12}^-$ Cu(I)F signal.[174]

However, in a LIB CuF_2 cathode, Li^+ ions in the electrolyte diffuse and interact with the CuF_2, unlike the reaction in a fluoride-ion battery where the diffusing species are purely copper and fluoride and as CuF_2 recieves electrons externally through the current collectors:

$$CuF_2 + 2e^- \rightarrow Cu + 2F^-$$

The conversion of CuF_2 in a FIB is therefore mechanistically different from that in LIB, as there is no breakage of Li-F bonds and no phase separation between Cu and LiF phases during cycling. Therefore, the fluorination mechanism of CuF_2 requires new understanding in the FIB context.

5.2.1 Synthesis of Monodisperse Cu Nanocubes

Understanding the copper fluorination mechanism is a compelling undertaking, as it can shed light on the possible failure pathways and propose ways to alleviate them to utilize the full reversible capacity. High-resolution transmission electron microscopy (HR)TEM and other complementary techniques provide a plethora of highly resolved chemical, morphological, and structural information for a crystalline particle during its conversion reaction.[175] However, in a real battery, the utility of these tools is restricted by the need to isolate particles that are single crystalline and in the same state-of-charge and on a high-symmetry axis. Even still, such a particle would need be representative of the entire cathode material due to the variety of morphologies, crystallinities and orientations. In a typical cathode, the active material (e.g. CuF_2) is ball milled, resulting in irregular size and morphology distribution, in addition to the presence of conductive carbon and binders, all preventing the isolation of individual copper particles that are representative of the entire cathode.

Monodispersed, nanocrystalline materials can overcome these hurdles and unlock the use of (HR)TEM techniques for mechanistic study in conversion reactions. If a careful and deliberate synthesis of the active material was performed, instead of directly ball milling the powder, particles with uniform size, morphology, and lattice orientation can be obtained, so that the conversion of one particle can be safely extrapolated to represent the entire system. Such monodisperse nanoparticles can traditionally be synthesized using colloidal synthesis, where a high-temperature (100-300 °C) solution-phase synthesis results in uniform particle size with narrow size distribution (standard deviation <5%) as a result of a single, brief nucleation event followed by crystal growth and the use of long-chain ligands that coordinate to and stabilize the isolated particle.[176, 177] This rapid nucleation and growth can be achieved either by injecting the reagent into a hot solvent where the formation of supersaturated solution is alleviated by nucleation, and where further nucleation is prevented as the concentration now is below the critical concentration, or by mixing the precursors in a high-boiling point solvent at low temperature not to elicit a chemical reaction, followed by controllably ramping the temperature to achieve supersaturation that result in a burst of nucleation, where time, concentration, temperature and the choice of surfactant (i.e., stabilizer) all affect the size and morphology of the obtained nanoparticle.[176] The surfactant plays an important role in colloidal synthesis, reducing the interfacial free energy, γ, of the particle and preventing agglomeration to compensate for the reduction in bulk free energy in bigger particles:

$$\Delta G = -\frac{4}{3}\pi r^3 \Delta G_v + 4\pi r^2 \gamma$$

Where ΔG is the change in free energy for the nucleation reaction, r is the particle radius, and ΔG_v is the volume free energy of the bulk particle. The critical radius, r^*, at which these two effects are balanced occurs at $\frac{dG}{dr} = 0$, at which:

$$r^* = \frac{2\gamma}{\Delta G_v}$$

Thus, the use of surfactants reduces γ and facilitates smaller particle size. In colloidal syntheses, surfactants such as oleic acid, oleylamine, trioctylphosphine are often used, where the steric hindrance provided by the long alkyl chain reduces γ and suppresses the particle diffusion.[178]

Metal fluorides (FeF_2, CoF_2) are known to form upon the single-precursor decomposition of the corresponding metal trifluoroacetate at high temperatures (250 - 350 °C), with byproducts CO_2 + CO + CHF_3 + H_2O + HF in addition to the metal fluoride.[179] Recently, this synthesis was developed into a colloidal synthesis to obtain monodisperse FeF_2 by the use of the surfactants oleyl amine (OLAM), oleic acid (OLAC) and a 1-octadecene (1-ODE) solvent, with the aim of mechanistically understanding the conversion reaction in a lithium-ion battery.[177]

However, extending this synthesis to monodisperse CuF_2 has been notoriously arduous due to the high reduction potential of Cu^{2+}, which results inadvertently in the formation of metallic copper. For this reason, single source precursors such as metal trifluoroacetates cannot be used with the conventional solvents and surfactants combinations to form CuF_2. Thus, starting from the discharged state (i.e., copper metal) and then performing the fluorination is more attainable than starting from the CuF_2. Namely, using CuBr as a precursor, trioctylphosphine oxide (TOPO) and oleylamine (OLAM) as surfactants gives monodisperse metallic copper particles,[180] which can then be used to investigate the fluorination mechanism starting from the discharged state:

$$CuBr \rightarrow Cu$$

The first few attempts at synthesizing monodisperse Cu nanocubes were hindered by either not obtaining the desired morphology, or by getting too thick an organic layer. For the morphology, the drying of the synthesized copper nanocubes had to be performed in a high-vacuum oven that was free of any contamination, particularly sulfur contamination. We presume that traces of sulfur from other experiments in the oven resulted in the rapid formation of CuS,

resulting in the undesired irregular dendritic morphology (Figure 5.1). For the organic layer (Figure 5.2), the washing of the resulting copper suspension had to be improved to include both polar and nonpolar solvents, to remove both the aliphatic and polar ends of the surfactants coordinating the copper particles. It was found that five washes of 1:1 ethanol:hexane were sufficient to remove the organic gunk surrounding the particles.

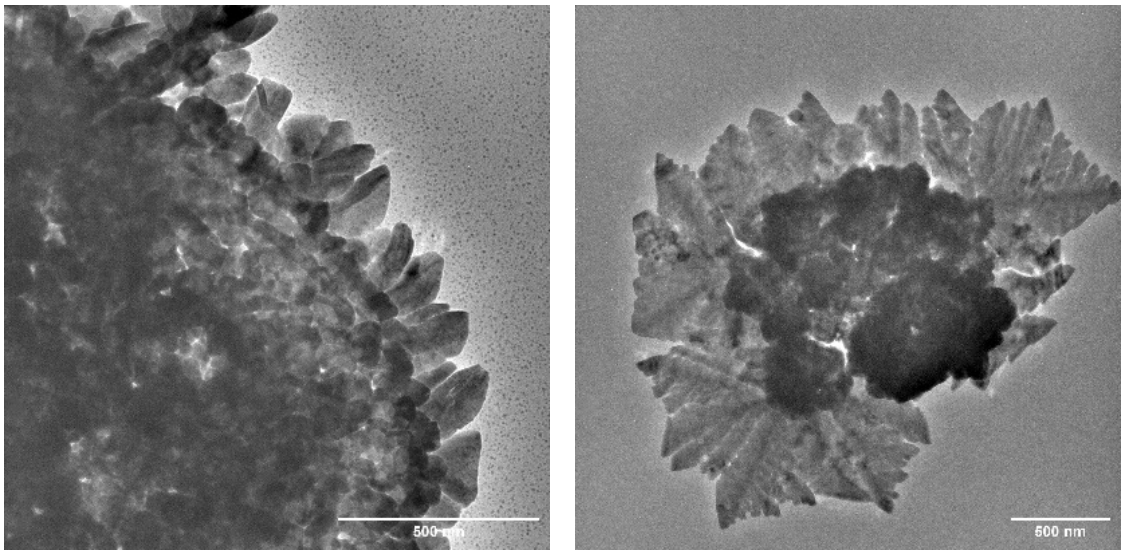


Figure 5.1: Irregular, dendritic morphology upon the attempted synthesis of copper nanocubes.

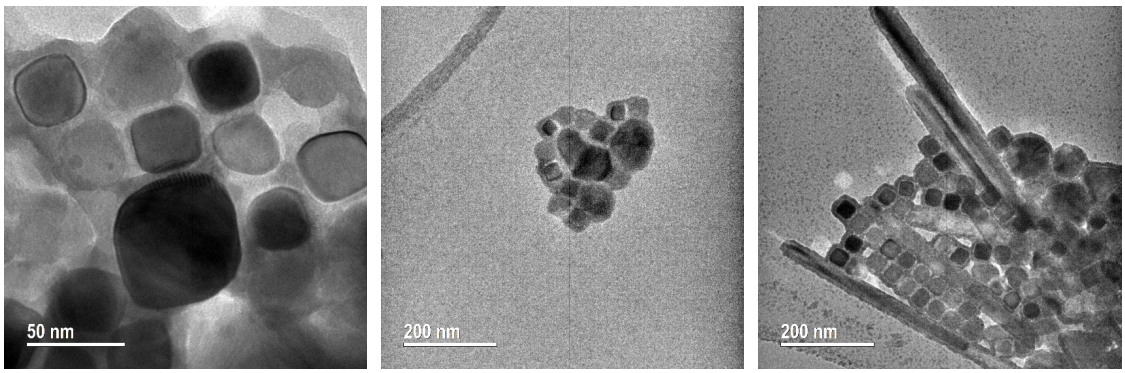


Figure 5.2: Thick organic layers covering copper nanoparticles due to residual surfactants from the colloidal synthesis.

After multiple iterative trials, monodisperse copper nanocubes were reproducibly obtained with the desired monodispersity, with a particle size of 44.2 nm and a size distribution of 3.8 %, confirming the monodisperse morphology

criteria (Figure 5.3a), which extends over much of the particle distribution (Figure 5.3b). Furthermore, selected area electron diffraction (SAED) shows a poly-crystalline Cu nanocubes, as evident by the multiple lattice orientations in the electron diffraction pattern (Figure 5.3c). The lattice planes (111) (222), (220), and (200) were observed corresponding to face-centered cubic phase. Furthermore, (HR)TEM analysis of a single nanocube more closely shows a thin layer encapsulating the copper nanocubes (Figure5.4a). Further elemental analysis using x-ray photoelectron spectroscopy (XPS) shows that the surface contains a thin layer of copper oxide (CuO), most likely forming during the short exposure of the sample to air during the operation of the TEM experiments. Overall, these results confirm that monodisperse copper nanocubes were obtained, enabling the study of the copper fluorination mechanism.

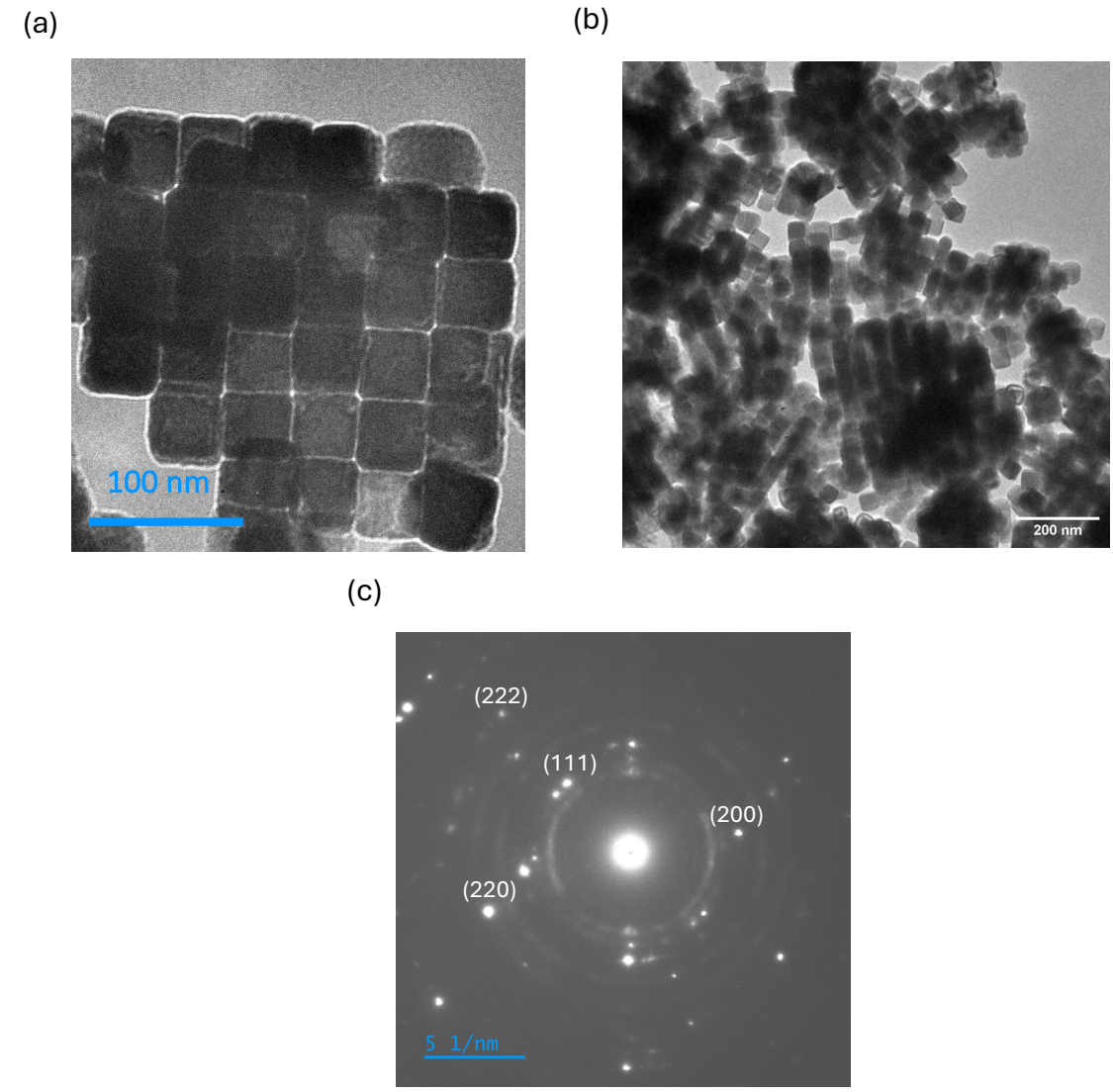


Figure 5.3: TEM micrograph and SAED pattern of the successful synthesis of monodisperse copper nanocubes with particle size of 44.2 nm.

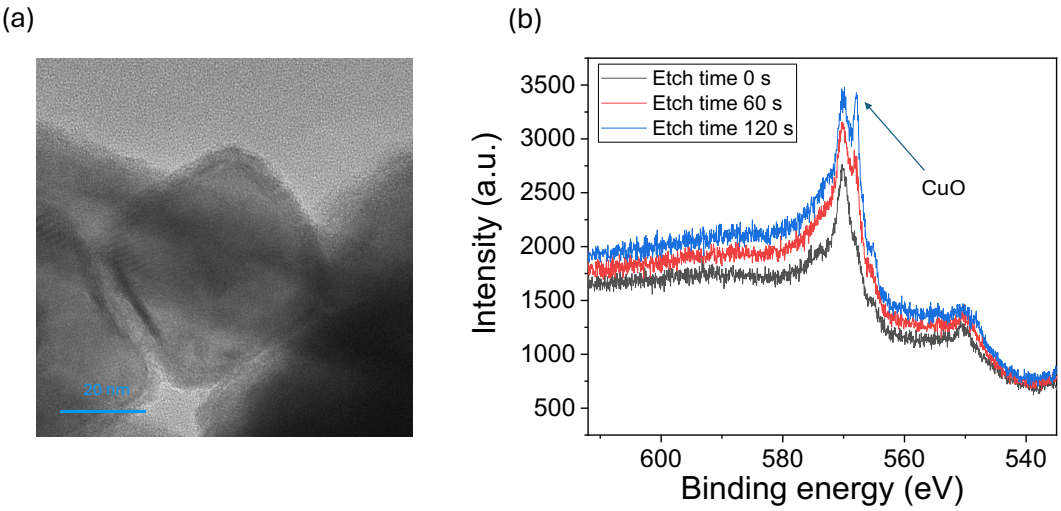


Figure 5.4: XPS of the pristine Cu particle showing the formation of a copper oxide layer.

5.2.2 In-situ Fluorination of the Cu Nanocubes

In-situ fluorination of the copper nanocubes was performed by inserting a fluorinating tip to touch the copper nanocubes under TEM while applying a potential bias. The fluorinating tip was prepared by scratching soft lead with a tungsten tip, then fluorinating the metallic lead using a solution of CsF in methanol followed by the washing of the electrolyte and drying of the tip (Figure 5.5)a), which in turn was connected to a potentiostat voltage bias to observe the conversion of the copper nanocubes to CuF_2 in-situ under TEM (Figure 5.5)a).

The conversion reaction observed under TEM shows the propagation of the copper conversion reaction front across particle boundaries even in the absence of electrolyte (Figure 5.6). Despite some particle fusion, the monodispersity and morphology was maintained during the charge reaction, in addition to a maintained crystallinity as evident by the SAED pattern matching the lattice of CuF_2. Spatial inhomogeneity during the conversion reaction is an underlying reason of the high polarization in CuF_2, and therefore the voltage hysteresis and capacity loss, which is a result of the conversion reaction occurring at the surface before proceeding to the core of the particle. In a LIB CuF_2, the outer layer is a Cu(o)/LiF and the inner core is unreacted, with the polarization stemming

from the Cu(0)/LiF interphase.[174] This is particularly challenging in lithium CuF_2 given that both Cu and LiF are cubic and could form low energy, homogeneous interfaces, in contrast with the monoclinic CuF_2. While following a similar morphological evolution and reaction front propagation, this LiF interphase is absent in the fluoride-ion conversion CuF_2 cathode, resulting in what seems like a fully reacted core. Still, an outer layer of a different phase persists after the conversion reaction, which is likely the CuO already present in the nanocubes.

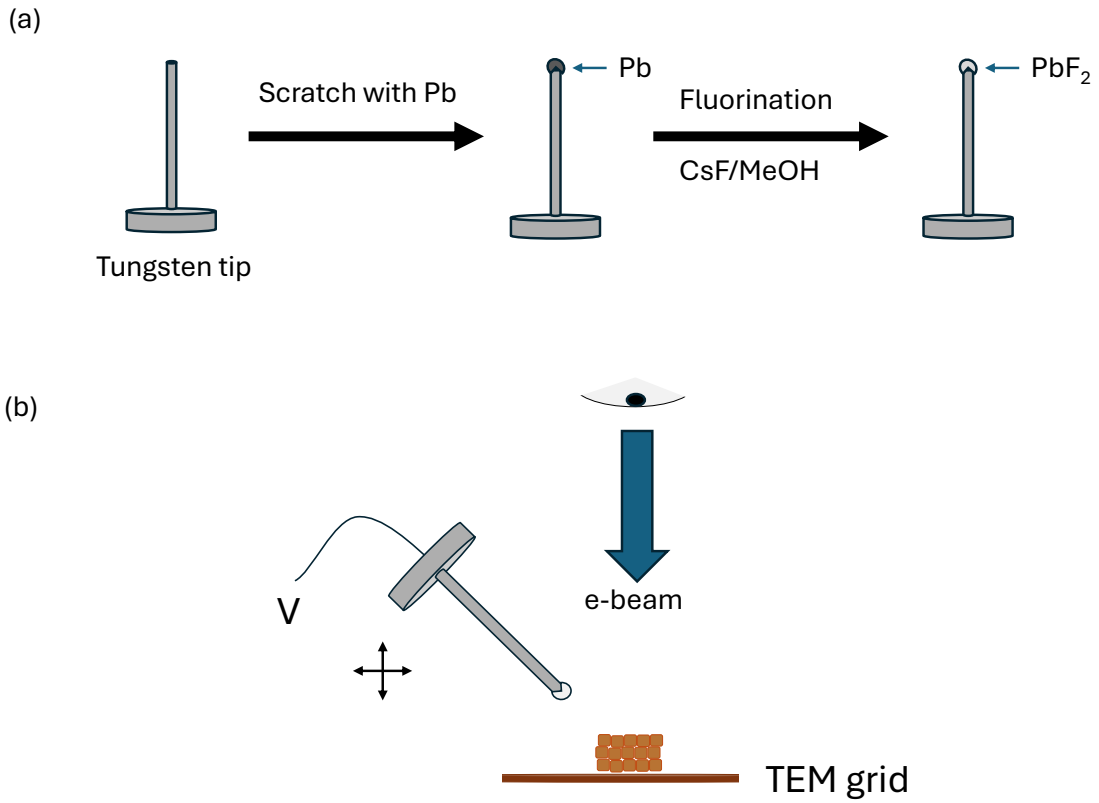


Figure 5.5: Schematic of the experimental setup for the in-situ TEM fluorination of the copper nanocubes.

5.3 Reference Electrodes for FIBs

A reference electrode provides a known potential against which the working potential can be measured, which is crucial in electrolyte characterization and

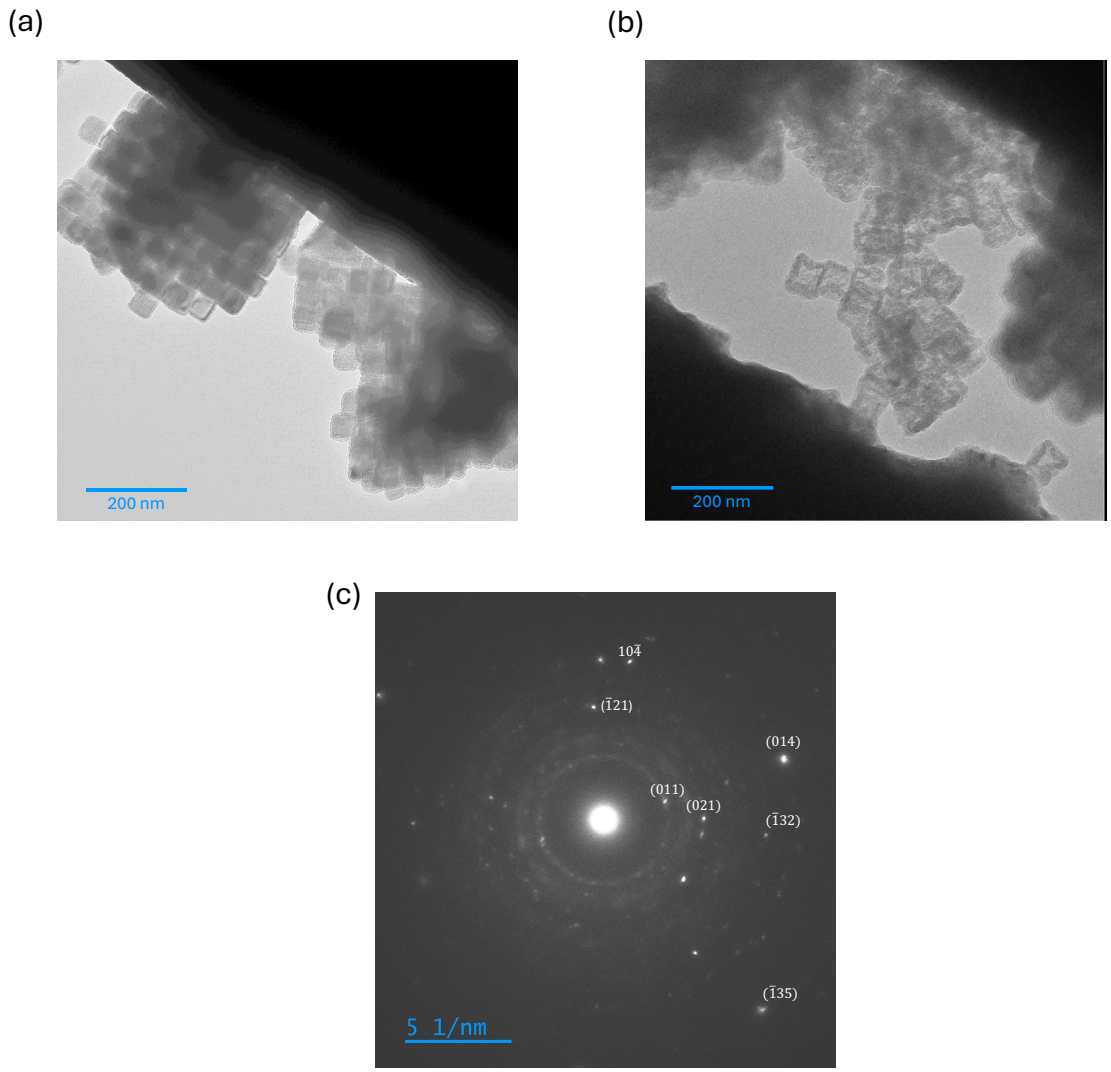


Figure 5.6: The copper nanocubes at the pristine state (a), the TEM micrograph after the in-situ fluorination reaction (b), and electron diffraction of the converted copper nanocubes (c).

electrochemical testing for FIBs. Ideally, a reference electrode will have a potential that is independent from that of the analyzed electrolyte, meaning that it is independent of the fluoride activity, and is constant regardless of the variable potential in the working electrode.

The commonly used and commercially available reference electrodes, such as the saturated calomel electrode (SCE), standard hydrogen electrode (SHE), or the AgCl/Ag, are not suitable for the fluoride-ion battery due to their chemical incompatibility, which is the reason most FIB studies have been using non-ideal

pseudo reference electrodes. There have not been any reports, to the best of our knowledge, on a stable reference electrode for the fluoride-ion battery.

In our setting for testing electrolytes using 3-electrode cells, we often use a pseudo Pb/PbF_2 reference electrode followed by calibration with ferrocene. However, this was problematic for multiple reasons. First, ferrocene did not always show redox peaks in the CV. This irreversibility is likely due to some degradation of the ferrocene where the fluoride can attack the ferrocene aromatic ring. Second, the Pb/PbF_2 pair, although often stable towards most electrolytes, has a reduction potential of 2.89 V vs. Li^+/Li which sits at the center of most electrolytes electrochemical windows, so traces of dissolved lead would sometimes show small redox peaks in the LSV curve, in addition to the variable open circuit potential due to the dependence of the Pb/PbF_2 on the fluoride concentration.

A few attempts were made to fabricate an alternative reference electrode. First, a small copper block was machined to fit a banana plug at the top (Figure 5.7). A small side bolt was also added so that a silver wire can be inserted at the bottom and screwed from the side. This assembly comprised the essential silver wire that is to be connected to the potentiostat. The electrode frit was first made of a PTFE and the sides of the pipette were melted for sealing (Figure 5.7a). However, this assembly was leaking within minutes, so another pipette was made to fit two longer PTFE frits at the bottom of the electrode (Figure 5.7b). However, this PTFE frit, despite being sealed at one end, had an opening at the other end as it was designed for liquid chromatography filtration, resulting also in leakage of the reference electrode solution within 1 hour. This prompted the redesign of all the electrode components so that a sturdy and leakless electrode can be obtained.

A rod made from Polyether ether ketone (PEEK), known for its chemical stability and durability, was machined to leave a 3 mm opening, which allows the plug connected to the silver wire to sit flush at the top. To have more control over the shape, thickness, and porosity of the frit, PTFE was replaced with a compact powder of LaF_3, as PTFE tends to degrade without undergoing a glass transition

which prevents shaping it to fill and seal the electrode tip. Furthermore, LaF_3 is chemically stable towards the fluoride and organic solvent. A LaF_3 frit made in house starting from powdered LaF_3 was pressed using a 3 mm mold under 200 MPa, giving a 2 mm thick pellet that was secured and sealed at the electrode tip using an epoxy resin (Figure 5.8).

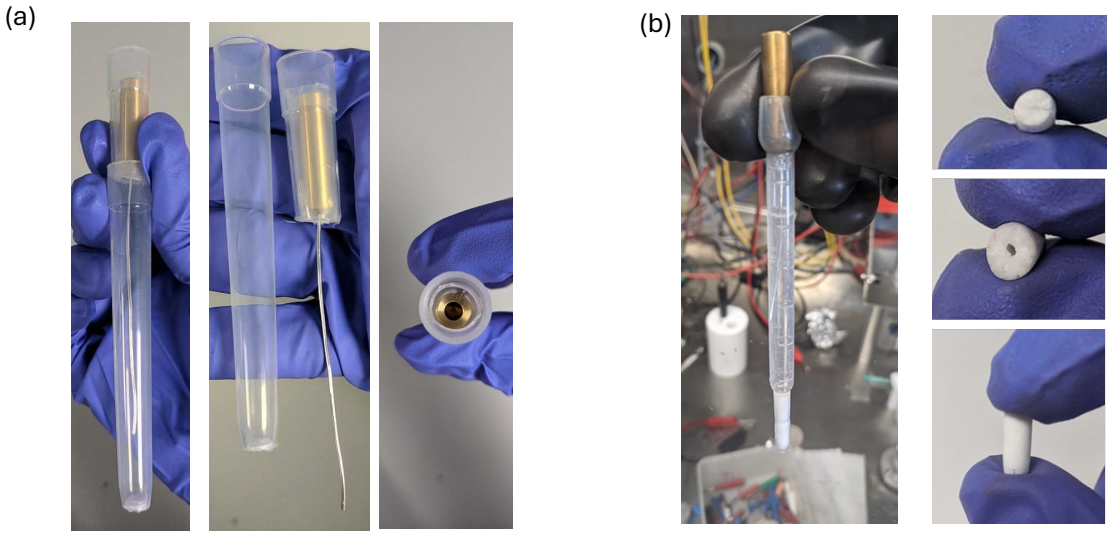


Figure 5.7: Early reference electrode assemblies using a pipette and a PTFE frit.

Performing OCV using a 3-electrode cell, with platinum as the counter/reference and the designed Ag^+/Ag electrode as the working electrode, shows an initial jump in potential for 10 h due to the soaking needed to overcome the impedance at the electrode junction. This, however, was followed by a stable OCV for over 30 hours, indicating the stability of the reference electrode and the feasibility for studying fluoride-ion electrolytes. At the end of the test, however, the tip of the electrode was examined and found to have accumulated some black material. This is likely due to the formation of some AgF_2 as some Ag^+ escapes the reference electrode solution.

5.4 The Future of FIB electrodes

No work in the FIB literature, to the best of our knowledge, has focused on understanding the fluorination mechanism or SEI formation in low-potential fluoride

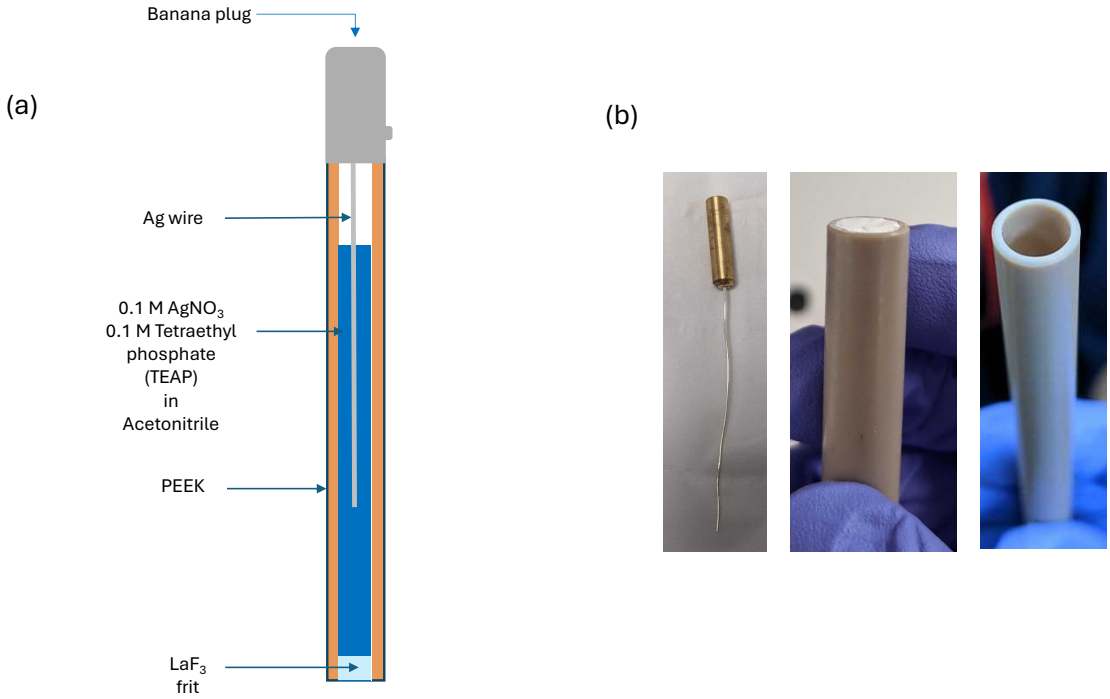


Figure 5.8: Final reference electrode design, using Ag^+/Ag, PEEK case, and LaF_3 pellet as a frit.

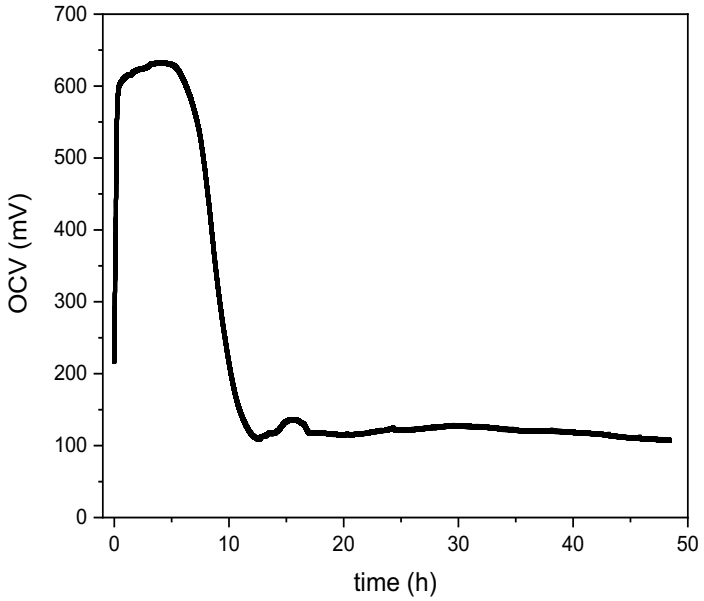


Figure 5.9: OCV for the reference electrode as working electrode versus a platinum counter for 50 hours.



Figure 5.10: The reference electrode tip forming a black residual at the end of the OCV experiment

anodes. This could be because cathodes are typically the limiting factor to the cell capacity, but also partially because no electrolytes have been formulated with ESW covering <0.5 V vs. Li^+/Li. CaF_2 is the most promising, yet so far untapped, anode material due to its high fluoride conductivity, low cost, almost no volume change during (de)fluorination, and a high capacity of 686.5 mAh/g.

Furthermore, while not that attractive as FIB cathodes due to their limited capacity, intercalation materials can be used as anode materials due to their superior cycling stability. Unlike oxides of electropositive metals, like $Sr_2TiO_3F_2$ which cannot achieve low redox potentials and which have only been defluorinated chemically, electrides based on Ca, Sr, Y, Ce, or La (e.g. $Ca_2N^+e^-$) can be a compelling anode material due to its near-zero (vs. Li^+/Li) redox potential.

References

[1] Lina Zhao et al. “Engineering of sodium-ion batteries: Opportunities and challenges”. In: *Engineering* 24 (2023), pp. 172–183.

[2] U.S. Geological Survey. *Mineral Commodity Summaries 2021*. Tech. Rep. Reston, Virginia, U.S.A.: U.S. Geological Survey, 2021.

[3] M. G. García and L. Borgnino. “CHAPTER 1: Fluoride in the Context of the Environment”. In: *Food and Nutritional Components in Focus*. Vol. 2015-Janua. Royal Society of Chemistry, 2015, pp. 3–21.

[4] Albert W Xiao, Giulia Galatolo, and Mauro Pasta. “The case for fluoride-ion batteries”. In: *Joule* 5.11 (2021), pp. 2823–2844.

[5] M. Anji Reddy and M. Fichtner. “Batteries based on fluoride shuttle”. In: *Journal of Materials Chemistry* 21 (2011), pp. 17059–17062.

[6] W. Baukal. “Über Reaktionsmöglichkeiten in Elektroden von Festkörperbatterien”. In: *Electrochimica Acta* X.Y (Z), pp. 687–694.

[7] J. H. Kennedy and J. C. Hunter. “Thin□Film Galvanic Cell Pb / PbF2 / PbF2 , CuF2 / Cu”. In: *Journal of the Electrochemical Society* 123 (1976), pp. 10–14.

[8] J. Schoonman. “A Solid□State Galvanic Cell with Fluoride□Conducting Electrolytes”. In: (1976). Add more details if necessary.

[9] J Schoonman and A Wolfert. “Alloy-anodes in fluoride solid-state batteries”. In: *J. Electrochem. Soc* 128.7 (1981), pp. 1522–1523.

[10] K. Mori et al. “Experimental Visualization of Interstitialcy Diffusion Pathways in Fast-Fluoride-Ion-Conducting Solid Electrolyte $Ba_{0.6}La_{0.4}F_{2.4}$”. In: *ACS Applied Energy Materials* 3 (2020), pp. 2873–2880.

[11] A. Roos et al. “Ionic conductivity in tysonite-type solid solutions $La_{1-x}Ba_xF_{3-x}$”. In: *Solid State Ionics* 13 (1984), pp. 191–203.

[12] C. Rongeat et al. “Solid electrolytes for fluoride ion batteries: Ionic conductivity in polycrystalline tysonite-type fluorides”. In: *ACS Applied Materials Interfaces* 6 (2014), pp. 2103–2110.

[13] J. Chable et al. “Fluoride solid electrolytes: From microcrystalline to nanostructured tysonite-type $La_{0.95}Ba_{0.05}F_{2.95}$”. In: *Journal of Alloys and Compounds* 692 (2017), pp. 980–988.

[14] L. Zhang et al. “Development of dense solid state thin-film electrolyte for fluoride ion batteries”. In: *Journal of Alloys and Compounds* 684 (2016), pp. 733–738.

[15] Mohammad Ali Nowroozi et al. “Fluoride ion batteries–past, present, and future”. In: *Journal of Materials Chemistry A* 9.10 (2021), pp. 5980–6012.

[16] L. Zhang, M. A. Reddy, and M. Fichtner. “Electrochemical performance of all solid-state fluoride-ion batteries based on thin-film electrolyte using alternative conductive additives and anodes”. In: *Journal of Solid State Electrochemistry* 22 (2018), pp. 997–1006.

[17] C. Rongeat et al. “Development of new anode composite materials for fluoride ion batteries”. In: *Journal of Materials Chemistry A* 2 (2014), pp. 20861–20872.

[18] P. Molaiyan and R. Witter. “Crystal phase and surface defect driven synthesis of $Pb_{1x}Sn_xF_2$ solid solution electrolyte for fluoride ion batteries”. In: *Journal of Electroanalytical Chemistry* 845 (2019), pp. 154–159.

[19] Miwa Murakami et al. “High Anionic Conductive Form of Pb x Sn2–x F4”. In: *Chemistry of Materials* 31.18 (2019), pp. 7704–7710.

[20] I. Mohammad et al. “Room-Temperature, Rechargeable Solid-State Fluoride-Ion Batteries”. In: *ACS Applied Energy Materials* 1 (2018), pp. 4766–4775.

[21] M. A. Nowroozi and O. Clemens. “Insights on the Behavior of Conversion-Based Anode Materials for Fluoride Ion Batteries by Testing against an Intercalation-Based Reference Cathode”. In: *ACS Applied Energy Materials* 1 (2018), pp. 6626–6637.

[22] T. Yamamoto et al. “Room-Temperature Fluoride Shuttle Batteries Based on a Fluorohydrogenate Ionic Liquid Electrolyte”. In: *ACS Applied Energy Materials* 2 (2019), pp. 6153–6157.

[23] Xuejin Li et al. “Initiating a Room-Temperature Rechargeable Aqueous Fluoride-Ion Battery with Long Lifespan through a Rational Buffering Phase Design”. In: *Advanced Energy Materials* 11.14 (2021).

[24] O. Clemens et al. “Electrochemical fluorination of perovskite type $BaFeO_{2.5}$”. In: *Dalton Transactions* 43 (2014), pp. 15771–15778.

[25] Mohammad Ali Nowroozi. “On the Development of Intercalation-Based Cathode Materials for All-Solid-State Fluoride Ion Batteries”. In: (2020).

[26] M. A. Nowroozi et al. “$LaSrMnO_4$: Reversible Electrochemical Intercalation of Fluoride Ions in the Context of Fluoride Ion Batteries”. In: *Chemistry of Materials* 29 (2017), pp. 3441–3453.

[27] Mohammad Ali Nowroozi et al. “High cycle life all-solid-state fluoride ion battery with La2NiO4+ d high voltage cathode”. In: *Communications materials* 1.1 (2020), p. 27.

[28] Mohammad Ali Nowroozi et al. “La 2 CoO 4: a new intercalation based cathode material for fluoride ion batteries with improved cycling stability”. In: *Journal of Materials Chemistry A* 6.11 (2018), pp. 4658–4669.

[29] Kerstin Wissel et al. “Topochemical fluorination of La2NiO4+ d: Unprecedented ordering of oxide and fluoride ions in La2NiO3F2”. In: *Inorganic Chemistry* 57.11 (2018), pp. 6549–6560.

[30] Benjamin P de Laune and Colin Greaves. “Structural and magnetic characterisation of CoSb2O4, and the substitution of Pb2+ for Sb3+”. In: *Journal of Solid State Chemistry* 187 (2012), pp. 225–230.

[31] Akshaya K Padhi, Kirakodu S Nanjundaswamy, and John B Goodenough. “Phospho-olivines as positive-electrode materials for rechargeable lithium batteries”. In: *Journal of the electrochemical society* 144.4 (1997), p. 1188.

[32] Wasif Zaheer et al. “Reversible room-temperature fluoride-ion insertion in a tunnel-structured transition metal oxide host”. In: *ACS Energy Letters* 5.8 (2020), pp. 2520–2526.

[33] Mohammad Ali Nowroozi, Benjamin de Laune, and Oliver Clemens. “Reversible electrochemical intercalation and deintercalation of fluoride ions into host lattices with Schafarzikite-type structure”. In: *ChemistryOpen* 7.8 (2018), pp. 617–623.

[34] Steven T Hartman and Rohan Mishra. “Layered electrides as fluoride intercalation anodes”. In: *Journal of Materials Chemistry A* 8.46 (2020), pp. 24469–24476.

[35] Scott C Warren et al. *Metal carbides and metal nitrides for a fluoride ion battery*. US Patent 11,710,825. July 2023.

[36] Fabienne Gschwind, Zhirong Zao-Karger, and Maximilian Fichtner. “A fluoride-doped PEG matrix as an electrolyte for anion transportation in a room-temperature fluoride ion battery”. In: *Journal of Materials Chemistry A* 2.5 (2014), pp. 1214–1218.

[37] Fabienne Gschwind and Joshua Bastien. “Parametric investigation of room-temperature fluoride-ion batteries: assessment of electrolytes, Mg-based anodes, and BiF 3-cathodes”. In: *Journal of Materials Chemistry A* 3.10 (2015), pp. 5628–5634.

[38] Keitaro Takahashi et al. “Fluoride Ion Conductive Polymer Electrolytes for All-solid-state Fluoride Shuttle Batteries”. In: *Electrochemistry* 88.4 (2020), pp. 310–313.

[39] Maciej Galiński, Andrzej Lewandowski, and Izabela Stępniak. “Ionic liquids as electrolytes”. In: *Electrochimica acta* 51.26 (2006), pp. 5567–5580.

[40] Kang Xu. “Electrolytes and interphases in Li-ion batteries and beyond”. In: *Chemical reviews* 114.23 (2014), pp. 11503–11618.

[41] Victoria K Davis et al. “Room-temperature cycling of metal fluoride electrodes: Liquid electrolytes for high-energy fluoride ion cells”. In: *Science* 362.6419 (2018), pp. 1144–1148.

[42] Victoria K Davis et al. “Fluoride-ion solvation in non-aqueous electrolyte solutions”. In: *Materials Chemistry Frontiers* 3.12 (2019), pp. 2721–2727.

[43] Tiancheng Tan et al. “Anhydrous N, N-Dimethyl-N, N-Dineopentylammonium Fluoride Electrolyte for Fluoride Ion Batteries”. In: *Chemistry of Materials* 36.9 (2024), pp. 4553–4560.

[44] Hiroaki Konishi et al. “Electrochemical performance of a bismuth fluoride electrode in a reserve-type fluoride shuttle battery”. In: *Journal of The Electrochemical Society* 164.14 (2017), A3702.

[45] Hiroaki Konishi et al. “Triphenylboroxine and triphenylborane as anion acceptors for electrolyte in fluoride shuttle batteries”. In: *Chemistry Letters* 47.11 (2018), pp. 1346–1349.

[46] Hiroaki Konishi et al. “Charge and Discharge Reactions of a Lead Fluoride Electrode in a Liquid-Based Electrolyte for Fluoride Shuttle Batteries:-The Role of Triphenylborane as an Anion Acceptor-”. In: *ChemistrySelect* 4.19 (2019), pp. 5984–5987.

[47] Hiroaki Konishi et al. “Electrochemical properties of lead fluoride electrode in fluoride shuttle battery”. In: *Journal of Electroanalytical Chemistry* 826 (2018), pp. 60–64.

[48] Hiroaki Konishi et al. “Improvement of cycling performance in bismuth fluoride electrodes by controlling electrolyte composition in fluoride shuttle batteries”. In: *Journal of Applied Electrochemistry* 48 (2018), pp. 1205–1211.

[49] H. Konishi et al. “Improved electrochemical performances in a bismuth fluoride electrode prepared using a high energy ball mill with carbon for fluoride shuttle batteries”. In: *Journal of Electroanalytical Chemistry* 839 (2019), pp. 173–176. URL: https://doi.org/10.1016/j.jelechem.2019.03.063.

[50] H. Konishi et al. “Reversible Electrochemical Reaction of a Fluoride Shuttle Battery with a Bismuth(III) Fluoride Electrode and Electrolyte Containing Triphenylboroxine as an Anion Acceptor”. In: *ChemistrySelect* 5 (2020), pp. 6237–6241. URL: https://doi.org/10.1002/slct.202000943.

[51] H. Konishi et al. “Electrochemical performance of a lead fluoride electrode mixed with carbon in an electrolyte containing triphenylboroxine as an anion acceptor for fluoride shuttle batteries”. In: *Materials Chemistry and Physics* 226 (2019), pp. 1–5. URL: https://doi.org/10.1016/j.matchemphys.2018.12.018.

[52] Kang Xu et al. “LiBOB as salt for lithium-ion batteries: a possible solution for high temperature operation”. In: *Electrochemical and Solid-State Letters* 5.1 (2001), A26.

[53] Roman Holomb et al. “Vibrational spectroscopy and ab initio studies of lithium bis (oxalato) borate (LiBOB) in different solvents”. In: *The Journal of Physical Chemistry A* 110.40 (2006), pp. 11467–11472.

[54] Asuman Celik Kucuk et al. “Effects of LiBOB on salt solubility and BiF 3 electrode electrochemical properties in fluoride shuttle batteries”. In: *Journal of Materials Chemistry A* 7.14 (2019), pp. 8559–8567.

[55] Asuman Celik Kucuk and Takeshi Abe. “Borolan-2-yl involving anion acceptors for organic liquid electrolyte-based fluoride shuttle batteries”. In: *Journal of Fluorine Chemistry* 240 (2020), p. 109672.

[56] Toshiro Yamanaka et al. “In situ observation of fluoride shuttle battery reactions with dissolution-deposition mechanisms by Raman microscopy”. In: *Journal of The Electrochemical Society* 166.4 (2019), A635.

[57] Asuman Celik Kucuk et al. “Low-cost fluoride source for organic liquid electrolyte-based fluoride shuttle battery”. In: *Journal of The Electrochemical Society* 168.1 (2021), p. 010501.

[58] Hiroaki Konishi et al. “Reactivity of the anion acceptor in electrolyte: An important factor in achieving high electrochemical performance of a lead (II) fluoride electrode in a fluoride shuttle battery”. In: *Journal of Electroanalytical Chemistry* 871 (2020), p. 114103.

[59] Casey R Wade et al. “Fluoride ion complexation and sensing using organoboron compounds”. In: *Chemical reviews* 110.7 (2010), pp. 3958–3984.

[60] Zishuai Zhang et al. “Aqueous rechargeable dual-ion battery based on fluoride ion and sodium ion electrochemistry”. In: *Journal of Materials Chemistry A* 6.18 (2018), pp. 8244–8250.

[61] Xiaoqiao Hu et al. “The electrochemical behaviors of NaF dual battery based on the hybrid electrodes of nano-bismuth@ CNTs”. In: *Materials Letters* 233 (2018), pp. 332–335.

[62] Xiaoqiao Hu et al. “The electrochemical behaviors of NaF dual battery based on the hybrid electrodes of nano-bismuth@ CNTs”. In: *Materials Letters* 233 (2018), pp. 332–335.

[63] Giulia Galatolo et al. “Advancing fluoride-ion batteries with a Pb-PbF2 counter electrode and a diluted liquid electrolyte”. In: *ACS Energy Letters* 9.1 (2023), pp. 85–92.

[64] Guyue Li et al. “Electrolyte Design by Synergistic High-Donor Solvent and Alcohol Anion Acceptor for Reversible Fluoride Ion Batteries”. In: *Advanced Functional Materials* 34.41 (2024), p. 2406421.

[65] Yifan Yu et al. “High-capacity and long-cycling F-ion pouch cells enabled by green electrolytes”. In: *ACS Energy Letters* 9.3 (2024), pp. 1008–1016.

[66] Desiree Mae Prado and Clemens Burda. “Untapped Potential of Fluoride Ions in Maximizing the Electrochemical Stability of Deep Eutectic Solvents”. In: *The Journal of Physical Chemistry Letters* 15.24 (2024), pp. 6343–6346.

[67] Hiroki Yamamoto et al. “Fluoride-Based Deep Eutectic Solvents with Amide Dual-Hydrogen-Bond Donors”. In: *The Journal of Physical Chemistry Letters* 15.24 (2024), pp. 6249–6255.

[68] James H Clark. “Fluoride ion as a base in organic synthesis”. In: *Chemical Reviews* 80.5 (1980), pp. 429–452.

[69] M. Mautner. “The Ionic Hydrogen Bond and Ion Solvation: Correlations with Proton Affinity and Deviations Due to Structural Effects”. In: *Journal of the American Chemical Society* 106.5 (1984), pp. 1257–1264.

[70] J Emsley. “Very strong hydrogen bonding”. In: *Chemical Society Reviews* 9.1 (1980), pp. 91–124.

[71] Konrad Seppelt. “Does the naked fluoride ion exist?” In: *Angewandte Chemie International Edition in English* 31.3 (1992), pp. 292–293.

[72] Jack M Miller and James H Clark. “‘Naked fluoride’masked: nmr evidence for tight ion pairs in Kf–crown ether”. In: *Journal of the Chemical Society, Chemical Communications* 22 (1982), pp. 1318–1319.

[73] Shlomi Elias et al. “Synthesis, characterization, and reactivity of thermally stable anhydrous quaternary ammonium fluorides”. In: *Organic letters* 19.12 (2017), pp. 3039–3042.

[74] T. Yonezawa, Y. Sakamoto, and K. Nogawa. “Preparation of Tetrabutylammonium Fluoride–Alcohol Adducts as Fluorination Agents”. JP 06316551 A. 1994.

[75] Dong Wook Kim et al. “Facile nucleophilic fluorination reactions using tert-alcohols as a reaction medium: significantly enhanced reactivity of alkali metal fluorides and improved selectivity”. In: *The Journal of organic chemistry* 73.3 (2008), pp. 957–962.

[76] Keary M Engle et al. “Coordination diversity in hydrogen-bonded homoleptic fluoride–alcohol complexes modulates reactivity”. In: *Chemical Science* 6.9 (2015), pp. 5293–5302.

[77] GT Hefter. “Solvation of fluoride ions. 3. A review of fluoride solvation thermodynamics in nonaqueous and mixed solvents”. In: *Reviews in Inorganic Chemistry* 10.1-3 (1989), pp. 185–224.

[78] David A Wynn, Marie M Roth, and Bruce D Pollard. “The solubility of alkali-metal fluorides in non-aqueous solvents with and without crown ethers, as determined by flame emission spectrometry”. In: *Talanta* 31.11 (1984), pp. 1036–1040.

[79] GT Hefter and PJ McLay. “The solvation of fluoride ions. I. Free energies for transfer from water to aqueous alcohol and acetonitrile mixtures”. In: *Journal of solution chemistry* 17 (1988), pp. 535–546.

[80] Herbert O House, Edith Feng, and Norton P Peet. “Comparison of various tetraalkylammonium salts as supporting electrolytes in organic electrochemical reactions”. In: *The Journal of Organic Chemistry* 36.16 (1971), pp. 2371–2375.

[81] Scott D. Schimler et al. “Anhydrous Tetramethylammonium Fluoride for Room-Temperature SNAr Fluorination”. In: *The Journal of Organic Chemistry* 80.24 (2015), pp. 12137–12145.

[82] Richard A. Bartsch. “Eliminations from 2-Butyl Halides Induced by Halide Ions in Dimethylformamide and Dimethyl Sulfoxide”. In: *The Journal of Organic Chemistry* 35 (1970), pp. 1023–1025.

[83] Victor V. Grushin and William J. Marshall. “Fluorination of Nonactivated Haloarenes via Arynes under Mild Conditions, Resulting from Further Studies

toward Ar-F Reductive Elimination from Palladium(II)". In: *Organometallics* 27 (2008), pp. 4825–4828.

[84] R. K. Sharma and J. L. Fry. "Instability of Anhydrous Tetra-*n*-alkylammonium Fluorides". In: *The Journal of Organic Chemistry* 48 (1983), pp. 2112–2114.

[85] Haoran Sun and Stephen G. DiMagno. "Anhydrous Tetrabutylammonium Fluoride". In: *Journal of the American Chemical Society* 127 (2005), pp. 2050–2051.

[86] D. Phillip Cox, John Terpinski, and Wojciech Lawrynowicz. ""Anhydrous" Tetrabutylammonium Fluoride: A Mild but Highly Efficient Source of Nucleophilic Fluoride Ion". In: *The Journal of Organic Chemistry* 49 (1984), pp. 3216–3219.

[87] J. H. Clark and D. J. Nightingale. "Methylhexamethylenetetramine Fluoride Dihydrate: A New Fluorodenitration Reagent". In: *Journal of Fluorine Chemistry* 81 (1996), pp. 91–93.

[88] R. Z. Gnann et al. "Naked Fluoride Ion Sources: Synthesis, Characterization, and Coupling Reaction of 1-Methylhexamethylenetetramine Fluoride". In: *Journal of the American Chemical Society* 119.1 (1997), pp. 112–115.

[89] K. M. Harmon et al. "N,N,N-Trimethyl-1-adamantylammonium Fluoride, a Completely Anhydrous Quaternary Ammonium Fluoride Salt". In: *The Journal of Organic Chemistry* (1993), pp. 7294–7295.

[90] K. M. Harmon and B. A. Southworth. "Hydrogen Bonding Part 48. IR and Thermodynamic Study of the Lower Hydrates of N-Methylquinuclidinium Iodide, Bromide, Chloride, Fluoride, and Hydroxide; Evidence for a Temperature-Dependent Rearrangement of Hydrogen Bonds in the Chloride Monohydrate". In: *Journal of Molecular Structure* 298 (1993), pp. 23–36.

[91] S. Sef- et al. "Reactions of the 'Naked' Fluoride Ion: Syntheses and Structures of SeF_2^- and BrF". In: *Chemical Science* 4 (1995), pp. 261–265.

[92] S. Elias et al. "Synthesis, Characterization, and Reactivity of Thermally Stable Anhydrous Quaternary Ammonium Fluorides". In: *Organic Letters* (2017).

[93] Takashi Ooi and Keiji Maruoka. “Asymmetric Organocatalysis of Structurally Well-Defined Chiral Quaternary Ammonium Fluorides”. In: *Accounts of Chemical Research* 37 (2004), pp. 526–533.

[94] J. H. Clark. “The Anionic Side of Fluorine Chemistry”. In: *Fluorine Chemistry at the Millennium*. 2000, pp. 167–174.

[95] S. J. Brown and J. H. Clark. “Tetraphenylphosphonium Hydrogendifluoride: A New Source of Fluoride Ion”. In: *Journal of the Chemical Society, Chemical Communications* (1985), pp. 672–673.

[96] S. J. Brown, J. H. Clark, and D. J. Macquarrie. “Tetra-Arylfluorophosphoranes”. In: *Journal of Fluorine Chemistry* (1988), pp. 277–280.

[97] Andreas Kornath, Felix Neumann, and Heinz Oberhammer. “Tetramethylphosphonium Fluoride: ‘Naked’ Fluoride and Phosphorane”. In: *Inorganic Chemistry* 42 (2003), pp. 2894–2901.

[98] J. E. Richman and R. B. Flay. “Phosphonium Fluoride Salts”. In: *Journal of the American Chemical Society* 103 (1981), pp. 5265–5267.

[99] Sarah J. Ryan et al. “Acyl Azolium Fluorides for Room Temperature Nucleophilic Aromatic Fluorination of Chloro- and Nitroarenes”. In: *Organic Letters* 17 (2015), pp. 1866–1869.

[100] Zvi Rappoport, Shmuel E. Biali, and Miriam Kaftory. “Fluorinated Macrocyclic Ethers as Fluoride Ion Hosts. Novel Structures and Dynamic Properties”. In: *Journal of the American Chemical Society* 112 (1990), pp. 7707–7718.

[101] William Joseph Middleton and Chadds P. Ford. “Tris(Substituted Amino) Sulfonium Salts”. US3871965. United States Patent, vol. 2. 1976.

[102] J. L. Atwood et al. *Inclusion Compounds: Physical Properties and Applications*. Ed. by Academic Press. Vol. 3. 1984.

[103] F. Viigtle and E. Weber. *Host-Guest Complex Chemistry/Macrocycles*. Springer-Verlag, 1985.

[104] Charles L. Liotta and H. P. Harris. “The Chemistry of “Naked” Anions. I. Reactions of the 18-Crown-6 Complex of Potassium Fluoride with Organic Substrates in Aprotic Organic Solvents”. In: *Journal of the American Chemical Society* 459 (1974), pp. 2250–2252.

[105] J. W. Larson and T. B. McMahon. “Fluoride and Chloride Affinities of Main Group Oxides, Fluorides, Oxofluorides, and Alkyls. Quantitative Scales of Lewis Acidities from Ion Cyclotron Resonance Halide-Exchange Equilibria”. In: *Journal of the American Chemical Society* 107 (1985), pp. 766–773.

[106] J. W. Larson and T. B. McMahon. “Strong Hydrogen Bonding in Gas-Phase Anions. An Ion Cyclotron Resonance Determination of Fluoride Binding Energetics to Brønsted Acids from Gas-Phase Fluoride Exchange Equilibria Measurements”. In: *Journal of the American Chemical Society* 105 (1983), pp. 2944–2950.

[107] J. W. Larson and T. B. McMahon. “Chelation of Gas-Phase Anions. An Ion Cyclotron Resonance Study of Cooperative Binding to Fluoride and Chloride Ions”. In: *Journal of Physical Chemistry* 88 (1984), pp. 1083–1086.

[108] Martin Newcomb and Matthew T. Blanda. “Macrocycles Containing Tin. A Small, Exclusive Host for the Fluoride Ion”. In: *Tetrahedron Letters* 29 (1988), pp. 4261–4264.

[109] Michael E. Jung and Hong Xia. “Synthesis and Transport Properties of 12-Silacrown-3, a New Type of Anion Complexing Agent”. In: *Tetrahedron Letters* 29 (1988), pp. 297–300.

[110] Wei Liu, Allen G. Oliver, and Bradley D. Smith. “Stabilization and Extraction of Fluoride Anion Using a Tetralactam Receptor”. In: *Journal of Organic Chemistry* 84 (2019), pp. 4050–4057.

[111] Agnieszka Szumna and Janusz Jurczak. “A New Macrocyclic Polylactam-Type Neutral Receptor for Anions - Structural Aspects of Anion Recognition”. In: *European Journal of Organic Chemistry* (2001), pp. 4031–4039.

[112] Michał J. Chmielewski and Janusz Jurczak. “Anion Recognition by Neutral Macrocyclic Amides”. In: *Chemistry - A European Journal* 11 (2005), pp. 6080–6094.

[113] Michał J. Chmielewski and Janusz Jurczak. “Anion Binding versus Intramolecular Hydrogen Bonding in Neutral Macrocyclic Amides”. In: *Chemistry - A European Journal* 12 (2006), pp. 7652–7667.

[114] Michał J. Chmielewski, Tomasz Zieliński, and Janusz Jurczak. “Synthesis, Structure, and Complexing Properties of Macrocyclic Receptors for Anions”. In: *Pure and Applied Chemistry* 79 (2007), pp. 1087–1096.

[115] Mohand Melaïmi et al. “Structural and electrochemical investigations of the high fluoride affinity of sterically hindered 1,8-bis(boryl)naphthalenes”. In: *Inorganic Chemistry* 45.20 (2006), pp. 8136–8143. URL: https://doi.org/10.1021/ic060869u.

[116] R. Taube and J. Sieler. “Komplexkatalyse XLV. Die Darstellung von C-Allylnickel(II)-fluorid [Ni(C3H5)F], yl-nickel(II)-tris(pentafluorphenyl)-fluoroborat [Ni(C3H5)]FB(C6F5)3, einen Katalysator für die 1,4-Polymerisation des Buta”. In: *Journal of Organometallic Chemistry* 459 (1993), pp. 335–347. URL: https://doi.org/10.1016/0022-328X(93)83039-M.

[117] Shunsuke Miyasaka, Jun Kobayashi, and Toshihiro Kawashima. “Enhancement of the Lewis acidity by substitution of sulfur-containing hetero aromatics in triarylboranes”. In: *Tetrahedron Letters* 50 (2009), pp. 3467–3469. URL: https://doi.org/10.1016/j.tetlet.2009.04.066.

[118] Chi-Wei Chiu and François P. Gabbaï. “Fluoride ion capture from water with a cationic borane”. In: *Journal of the American Chemical Society* 128 (2006), pp. 14248–14249. URL: https://doi.org/10.1021/ja066508m.

[119] Howard E. Katz. “Hydride Sponge: 1,8-Naphthalenediylbis(dimethylborane)”. In: *Journal of the American Chemical Society* 107 (1985), pp. 1421–1423. URL: https://doi.org/10.1021/ja00291a023.

[120] Gianfranco Cainelli, Francesco Manescalchi, and M. P. Manescalchi. “Polymer-Supported Reagents. The Use of Anion-Exchange Resins in the Synthesis of Primary and Secondary Alkyl Fluorides from Alkyl Halides or Alkyl Methanesulfonates”. In: *Synthesis (Stuttgart)* (1976), pp. 472–473. URL: https://doi.org/10.1055/s-1976-24115.

[121] J. M. Miller, K. H. So, and J. H. Clark. “Hydrogen bond assisted organic reactions: C- and O-alkylations, sulphenylations, and Michael additions aided by polymer immobilized fluoride ion”. In: *Journal of the Chemical Society, Chemical Communications* (1978), pp. 466–467. URL: https://doi.org/10.1039/C39780000466.

[122] T. Ando and J. Yamawaki. “Potassium Fluoride on Celite - Versatile Reagent for C-Alkylation, N-Alkylation, O-Alkylation, and S-Alkylation”. In: *Chemistry Letters* (1979), pp. 45–46. URL: https://doi.org/10.1246/cl.1979.45.

[123] Roger G. Linford, ed. *Electrochemical Science and Technology of Polymers*. Vol. 1. London: Elsevier Applied Science, 1987.

[124] Noémie Elgrishi et al. “A practical beginner’s guide to cyclic voltammetry”. In: *Journal of chemical education* 95.2 (2018), pp. 197–206.

[125] Ryosuke Jinnouchi, Ferenc Karsai, and Georg Kresse. “On-the-fly machine learning force field generation: Application to melting points”. In: *Phys. Rev. B* 100.1 (July 2019). Publisher: American Physical Society, p. 014105. URL: https://link.aps.org/doi/10.1103/PhysRevB.100.014105 (visited on 04/12/2023).

[126] B. Hammer, L. B. Hansen, and J. K. NÃžrskov. “Improved adsorption energetics within density-functional theory using revised Perdew-Burke-Ernzerhof functionals”. In: *Phys. Rev. B* 59.11 (Mar. 1999). Publisher: American Physical

Society, pp. 7413–7421. URL: https://link.aps.org/doi/10.1103/PhysRevB.59.7413 (visited on 04/12/2023).

[127] Stefan Grimme et al. “A consistent and accurate ab initio parametrization of density functional dispersion correction (DFT-D) for the 94 elements H-Pu”. In: *J. Chem. Phys.* 132.15 (Apr. 2010). Publisher: American Institute of Physics, p. 154104. URL: https://aip.scitation.org/doi/10.1063/1.3382344 (visited on 04/12/2023).

[128] L. Martínez et al. “PACKMOL: A package for building initial configurations for molecular dynamics simulations”. In: *Journal of computational chemistry* 30.13 (2009), pp. 2157–2164.

[129] Guilhem Pagès et al. “Pulsed-field gradient nuclear magnetic resonance measurements (PFG NMR) for diffusion ordered spectroscopy (DOSY) mapping”. In: *Analyst* 142.20 (2017), pp. 3771–3796.

[130] Omar Alshangiti et al. “Solvent-in-salt electrolytes for fluoride ion batteries”. In: *ACS Energy Letters* 8.6 (2023), pp. 2668–2673.

[131] Yuki Yamada et al. “Advances and issues in developing salt-concentrated battery electrolytes”. In: *Nature Energy* 4.4 (2019), pp. 269–280.

[132] Yuki Yamada et al. “Unusual stability of acetonitrile-based superconcentrated electrolytes for fast-charging lithium-ion batteries”. In: *Journal of the American Chemical Society* 136.13 (2014), pp. 5039–5046.

[133] Liumin Suo et al. “A new class of solvent-in-salt electrolyte for high-energy rechargeable metallic lithium batteries”. In: *Nature communications* 4.1 (2013), p. 1481.

[134] Kaoru Dokko et al. “Solvate ionic liquid electrolyte for Li–S batteries”. In: *Journal of The Electrochemical Society* 160.8 (2013), A1304.

[135] Kazuki Yoshida et al. “Oxidative-stability enhancement and charge transport mechanism in glyme–lithium salt equimolar complexes”. In: *Journal of the American Chemical Society* 133.33 (2011), pp. 13121–13129.

[136] Liumin Suo et al. “A new class of Solvent-in-Salt electrolyte for high-energy rechargeable metallic lithium batteries”. In: *Nature Communications* 4 (2013), pp. 1–9.

[137] Ziren Fang et al. “A long-life aqueous Fluoride-ion battery based on Water-in-salt electrolyte”. In: *Inorganic Chemistry Communications* 148.December 2022 (2023), p. 110275. URL: https://doi.org/10.1016/j.inoche.2022.110275.

[138] Mohammad Ali Nowroozi et al. “Fluoride ion batteries - past, present, and future”. In: *Journal of Materials Chemistry A* 9.10 (2021), pp. 5980–6012.

[139] Kang Xu. “Electrolytes and interphases in Li-ion batteries and beyond”. In: *Chemical Reviews* 114.23 (2014), pp. 11503–11618.

[140] Karl O. Christe and William W. Wilson. “Nuclear magnetic resonance spectrum of the fluoride anion”. In: *Journal of Fluorine Chemistry* 46.2 (1990), pp. 339–342.

[141] Stuart Licht. “pH Measurement in Concentrated Alkaline Solutions”. In: *Analytical Chemistry* 57.2 (1985), pp. 514–519.

[142] M. Gerken et al. “The 19F NMR shifts are not a measure for the nakedness of the fluoride anion”. In: *Journal of Fluorine Chemistry* 116.1 (2002), pp. 49–58.

[143] Fredrick Omenya et al. “Intrinsic challenges to the electrochemical reversibility of the high energy density copper (II) fluoride cathode material”. In: *ACS Applied Energy Materials* 2.7 (2019), pp. 5243–5253.

[144] Jack Fawdon et al. “Characterising lithium-ion electrolytes via operando Raman microspectroscopy”. In: *Nature Communications* 12.1 (2021), p. 4053.

[145] Jinfan Li et al. “Weak cation–solvent interactions in ether-based electrolytes stabilizing potassium-ion batteries”. In: *Angewandte Chemie International Edition* 61.33 (2022), e202208291.

[146] Corey M Efaw et al. “Localized high-concentration electrolytes get more localized through micelle-like structures”. In: *Nature Materials* 22.12 (2023), pp. 1531–1539.

[147] Yanxin Shang et al. “An “Ether-in-Water” electrolyte boosts stable interfacial chemistry for aqueous lithium-ion batteries”. In: *Advanced Materials* 32.40 (2020), p. 2004017.

[148] Omar Alshangiti et al. “Imidazolium-based ionic liquid electrolytes for fluoride ion batteries”. In: *ACS Energy Letters* 9.12 (2024), pp. 6104–6108.

[149] Abdel Karim S Labban and Yizhak Marcus. “The solubility and solvation of salts in mixed nonaqueous solvents. 1. Potassium halides in mixed aprotic solvents”. In: *Journal of solution chemistry* 20 (1991), pp. 221–232.

[150] Karl O Christe et al. “Syntheses, properties, and structures of anhydrous tetramethylammonium fluoride and its 1: 1 adduct with trans-3-amino-2-butenenitrile”. In: *Journal of the American Chemical Society* 112.21 (1990), pp. 7619–7625.

[151] William T Miller Jr, John H Fried, and Harold Goldwhite. “Substitution and Addition Reactions of the Fluoroölefins. IV. 1 Reactions of Fluoride Ion with Fluoroölefins2, 3”. In: *Journal of the American Chemical Society* 82.12 (1960), pp. 3091–3099.

[152] Michael RC Gerstenberger and Alois Haas. “Methods of fluorination in organic chemistry”. In: *Angewandte Chemie International Edition in English* 20.8 (1981), pp. 647–667.

[153] Uwe Schröder et al. “Water-induced accelerated ion diffusion: voltammetric studies in 1-methyl-3-[2, 6-(S)-dimethylocten-2-yl] imidazolium tetrafluoroborate,

1-butyl-3-methylimidazolium tetrafluoroborate and hexafluorophosphate ionic liquids". In: *New Journal of Chemistry* 24.12 (2000), pp. 1009–1015.

[154] Jairton Dupont and Paulo AZ Suarez. "Physico-chemical processes in imidazolium ionic liquids". In: *Physical Chemistry Chemical Physics* 8.21 (2006), pp. 2441–2452.

[155] John D Holbrey, W Matthew Reichert, and Robin D Rogers. "Crystal structures of imidazolium bis (trifluoromethanesulfonyl) imide 'ionic liquid'salts: the first organic salt with a cis-TFSI anion conformation". In: *Dalton Transactions* 15 (2004), pp. 2267–2271.

[156] Giulia Galatolo. "Fluoride-ion batteries with liquid electrolytes". PhD thesis. University of Oxford, 2023.

[157] Anthony J Arduengo. "Looking for stable carbenes: the difficulty in starting anew". In: *Accounts of Chemical Research* 32.11 (1999), pp. 913–921.

[158] Tina L Amyes et al. "Formation and stability of N-heterocyclic carbenes in water: the carbon acid p K a of imidazolium cations in aqueous solution". In: *J. Am. Chem. Soc.* 126.13 (2004), pp. 4366–4374.

[159] Varinder K Aggarwal, Ingo Emme, and Andrea Mereu. "Unexpected side reactions of imidazolium-based ionic liquids in the base-catalysed Baylis–Hillman reaction". In: *Chemical Communications* 15 (2002), pp. 1612–1613.

[160] Roger W Alder, Paul R Allen, and Stuart J Williams. "Stable carbenes as strong bases". In: *Journal of the Chemical society, Chemical communications* 12 (1995), pp. 1267–1268.

[161] Olaf Kühl. "The chemistry of functionalised N-heterocyclic carbenes". In: *Chemical Society Reviews* 36.4 (2007), pp. 592–607.

[162] Daniela Tapu, David A Dixon, and Christopher Roe. "13C NMR spectroscopy of "Arduengo-type" carbenes and their derivatives". In: *Chem. Rev.* 109.8 (2009), pp. 3385–3407.

[163] Bogdan Dereka et al. “Crossover from hydrogen to chemical bonding”. In: *Science* 371.6525 (2021), pp. 160–164. eprint: https://www.science.org/doi/pdf/10.1126/science.abe1951. URL: https://www.science.org/doi/abs/10.1126/science.abe1951.

[164] Gautam R Desiraju and Thomas Steiner. *The weak hydrogen bond: in structural chemistry and biology*. Vol. 9. IUCr, 2001.

[165] Shiro Seki et al. “Imidazolium-based room-temperature ionic liquid for lithium secondary batteries: Effects of lithium salt concentration”. In: *J. Electrochem. Soc.* 154.3 (2007), A173.

[166] Jakob Asenbauer et al. “Solubilities and ionic conductivities of ionic liquids containing lithium salts”. In: *Electrochim. Acta* 247 (2017), pp. 1038–1043.

[167] Carine Rongeat et al. “Solid electrolytes for fluoride ion batteries: ionic conductivity in polycrystalline tysonite-type fluorides”. In: *ACS Applied Materials & Interfaces* 6.3 (2014), pp. 2103–2110.

[168] Carine Rongeat et al. “Nanostructured fluorite-type fluorides as electrolytes for fluoride ion batteries”. In: *The Journal of Physical Chemistry C* 117.10 (2013), pp. 4943–4950.

[169] LN Patro and K Hariharan. “Fast fluoride ion conducting materials in solid state ionics: An overview”. In: *Solid State Ionics* 239 (2013), pp. 41–49.

[170] Don H McTaggart et al. “Assessing ternary materials for fluoride-ion batteries”. In: *Scientific Data* 10.1 (2023), p. 90.

[171] Xiao Hua et al. “Comprehensive study of the CuF2 conversion reaction mechanism in a lithium ion battery”. In: *The Journal of Physical Chemistry C* 118.28 (2014), pp. 15169–15184.

[172] Feng Wang et al. “Conversion reaction mechanisms in lithium ion batteries: study of the binary metal fluoride electrodes”. In: *Journal of the American Chemical Society* 133.46 (2011), pp. 18828–18836.

[173] Jiale Xia et al. “Super-reversible CuF2 cathodes enabled by Cu2+-coordinated alginate”. In: *Advanced Materials* 34.43 (2022), p. 2205229.

[174] Yinzhu Jiang et al. “Breaking the voltage hysteresis of conversion electrodes for high energy batteries”. In: (2024).

[175] Jiang Cui, Hongkui Zheng, and Kai He. “In situ TEM study on conversion-type electrodes for rechargeable ion batteries”. In: *Advanced Materials* 33.6 (2021), p. 2000699.

[176] Christopher B Murray et al. “Colloidal synthesis of nanocrystals and nanocrystal superlattices”. In: *IBM Journal of Research and Development* 45.1 (2001), pp. 47–56.

[177] Albert W Xiao et al. “Understanding the conversion mechanism and performance of monodisperse FeF2 nanocrystal cathodes”. In: *Nature materials* 19.6 (2020), pp. 644–654.

[178] Christopher B Murray, Cherie R Kagan, and Moungi G Bawendi. “Synthesis and characterization of monodisperse nanocrystals and close-packed nanocrystal assemblies”. In: *Annual review of materials science* 30.1 (2000), pp. 545–610.

[179] Joseph S Francisco. “Decomposition pathways for trifluoroacetic acid, CF3C (O) OH”. In: *Journal of the Chemical Society, Faraday Transactions* 88.24 (1992), pp. 3521–3525.

[180] Yuxuan Wang et al. “Copper Nanocubes for CO2 Reduction in Gas Diffusion Electrodes”. In: *Nano Letters* 19.12 (2019), pp. 8461–8468.